Supporting Information

Towards Accelerating the Discovery of Efficient Iridium(III) Emitters Using Novel Database and Machine Learning Based Only on Structural Formula

Sergei V. Tatarin,[a] Lev V. Krasnov,[a] Ekaterina V. Nykhrikova,[a] Maxim M. Minin,[a,b] Daniil E. Smirnov,[a] Andrei V. Churakov,[a] Stanislav I. Bezzubov*[a]

[a] N.S. Kurnakov Institute of General and Inorganic Chemistry, Russian Academy of Sciences, Leninskii pr. 31, Moscow, 119991, Russia
E-mail: bezzubov@igic.ras.ru
[b] Department of Chemistry, Lomonosov Moscow State University, Lenin's hills 1/3, Moscow 119991, Russia

Table of Content

1. Experimental details

Materials and methods

All commercially available reagents were at least reagent grade and used without further purification. Solvents were distilled and dried according to standard procedures. Synthesis of 1-benzyl-2-phenyl-1H-benzo[d]imidazole (bim), 1-benzyl-2-(4-(tert-butyl)phenyl)-1H-benzo[d]imidazole (tbim), 1-benzyl-2-(4-chlorophenyl)-1H-benzo[d]imidazole (cbim), 1-benzyl-2-(3,4-dimethoxyphenyl)-1H-benzo[d]imidazole (mbim) was reported in[1], other N-benzylbenzimidazole ligands were synthesized in a similar way. Synthesis of $[Ir(phi)_2Cl]$ was reported in[2], phi - 1,2-diphenyl-1H-phenanthro[9,10-d]imidazole. Preparation of iridium(III) complexes was carried out under dry argon. Purification and other manipulations with complexes were performed in air.

^1H and $^{13}C\{^1H\}$ NMR spectra were acquired at 25 °C on a Bruker Avance 400 instrument and chemical shifts were reported in ppm referenced to residual solvent signals. High resolution and accurate mass measurements were carried out using a BrukermicroTOF-Q™ ESI-TOF (Electrospray Ionisation / Time of Flight) spectrometer. Electronic absorption spectra were measured on an OKB Spectr SF-2000 spectrophotometer. Luminescence measurements of the complexes in Ar-saturated dichloromethane solution were performed on a Perkin-Elmer LS-55 spectrometer. An Elins P20 potentiostat-galvanostat was used for electrochemical measurements with a platinum working electrode, platinum counter electrode, and silver quasi-reference electrode. Polarographic curves were recorded in Ar-saturated dichloromethane with 0.25 M (n-$Bu_4N)ClO_4$ at a scan rate of 200 mV/s. Ferrocene was used as an internal standard.

Characterization data for previously unreported cyclometalating benzimidazole ligands:

1-benzyl-5,6-dichloro-2-phenyl-1H-benzo[d]imidazole (dcbim): white crystals, yield 64%.
^1H NMR, δ, ppm. ($CDCl_3$): 5.41 (s, 2H), 7.03 – 7.10 (m, 2H), 7.29 (s, 1H), 7.32 – 7.40 (m, 3H), 7.43 – 7.55 (m, 3H), 7.63 – 7.70 (m, 2H), 7.93 (s, 1H).
$^{13}C\{^1H\}$ NMR, δ, ppm. ($CDCl_3$): 48.21, 111.46, 120.66, 125.40, 126.45, 126.60, 127.76, 128.55, 128.68, 128.77, 128.89, 130.10, 134.82, 134.99, 141.92, 155.62.

1-benzyl-2-(4-(*tert*-butyl)phenyl)-5,6-dichloro-1H-benzo[d]imidazole (tdcbim): white powder, yield 59%.
^1H NMR, δ, ppm. ($CDCl_3$): 1.34 (s, 9H), 5.45 (s, 2H), 7.06 – 7.13 (m, 2H), 7.28 (s, 1H), 7.31 – 7.41 (m, 3H), 7.46 – 7.53 (m, 2H), 7.60 – 7.67 (m, 2H), 7.95 (s, 1H).
$^{13}C\{^1H\}$ NMR, δ, ppm. ($CDCl_3$): 30.74, 34.54, 48.29, 111.44, 120.42, 125.36, 125.60, 126.60, 127.76, 128.52, 128.91, 134.70, 134.98, 153.71, 155.57.

1-benzyl-5,6-dichloro-2-(4-chlorophenyl)-1H-benzo[d]imidazole (tcbim), brown powder, yield 71%.

^{1}H NMR, δ, ppm. ($CDCl_3$): 5.39 (s, 2H), 7.02 – 7.09 (m, 2H), 7.30 (s, 1H), 7.32 – 7.41 (m, 3H), 7.41 – 7.47 (m, 2H), 7.56 – 7.64 (m, 2H), 7.92 (s, 1H).
^{13}C{^{1}H} NMR, δ, ppm. ($CDCl_3$): 48.21, 111.43, 120.72, 125.28, 126.67, 126.92, 127.12, 127.90, 128.87, 128.99, 130.04, 134.78, 134.90, 136.46, 141.79, 154.39.

1-benzyl-5,6-dimethyl-2-phenyl-1H-benzo[d]imidazole (dmbim), white powder, yield 82%.
^{1}H NMR, δ, ppm. ($CDCl_3$): 2.34 (s, 3H), 2.40 (s, 3H), 5.41 (s, 2H), 6.99 (s, 1H), 7.08 – 7.15 (m, 2H), 7.27 – 7.38 (m, 3H), 7.40 – 7.50 (m, 3H), 7.65 (s, 1H), 7.66 – 7.72 (m, 2H).
^{13}C{^{1}H} NMR, δ, ppm. ($CDCl_3$): 19.95, 20.20, 47.84, 110.18, 119.62, 125.49, 127.24, 128.27, 128.64, 128.76, 129.24, 129.92, 131.15, 131.84, 134.30, 136.32, 141.41, 152.96.

1-benzyl-2-(*p*-tolyl)-1H-naphtho[2,3-d]imidazole (mnim), beige powder, yield 79%.
^{1}H NMR, δ, ppm. ($CDCl_3$): 2.43 (s, 3H), 5.51 (s, 2H), 7.14 – 7.21 (m, 2H), 7.27 – 7.44 (m, 7H), 7.59 (s, 1H), 7.64 – 7.71 (m, 2H), 7.79 – 7.87 (m, 1H), 8.00 – 8.08 (m, 1H), 8.36 (s, 1H).
^{13}C{^{1}H} NMR, δ, ppm. ($CDCl_3$): 21.12, 48.25, 105.88, 116.26, 123.22, 123.97, 125.54, 126.30, 127.09, 127.38, 128.10, 128.73, 128.85, 129.19, 130.18, 130.23, 135.97, 136.42, 140.37, 142.55, 157.75.

Synthesis of dimeric Ir(III) complexes was performed according to a following procedure:
50 mg (0.142 mol) of iridium trichloride hydrate and 0.355 mmol of the corresponding ligand were suspended in a mixture of 2-ethoxyethanol (10 ml) and water (3 ml). The reaction mixture was refluxed for 12 hours in argon atmosphere. The resulting precipitate was filtered, washed with ethanol, ether and dried in vacuo at 50 °C. Yield of the crude product varies from 50 to 84%. Insufficient solubility of these compounds prevented acquisition of meaningful ^{1}H NMR spectra.

Synthesis of acetylacetonate complexes was performed according to a following procedure (acac – acetylacetone):
***[Ir(bim)$_2$(acac)]*, *[Ir(tbim)$_2$(acac)]*, *[Ir(cbim)$_2$(acac)]*, *[Ir(mbim)$_2$(acac)]*, *[Ir(dcbim)$_2$(acac)]*, *[Ir(tdcbim)$_2$(acac)]*, *[Ir(tcbim)$_2$(acac)]*, *[Ir(dmbim)$_2$(acac)]*, *[Ir(mnim)$_2$(acac)]*:**
In an 8 ml vial, 30 mg of a corresponding dimeric chloride, 18 mg K_2CO_3 and 8 μl of acetylacetone were suspended in 4 ml of acetonitrile. The suspensions were flushed with argon for 5 minutes and sealed tightly. After that the reaction mixture was heated to 65°C for 24 h. The resulting yellow-orange solids were filtered in vacuo, thoroughly washed with deionized water and dried in vacuo (unless otherwise specified). The purification of the products was conducted as follows:

***[Ir(bim)$_2$(acac)]*:** crude product was pure.
Yellow powder, yield: 46%.

^{1}H NMR(DMSO-d_6) δ, ppm.: 7.82 (d, J = 8.1 Hz, 2H), 7.60 – 7.50 (m, 4H), 7.40 – 7.30 (m, 8H), 7.27 – 7.21 (m, 2H), 7.17 – 7.12 (m, 4H), 6.63 (td, J = 7.5, 1.3 Hz, 2H), 6.47 (td, J = 7.5, 1.2 Hz, 2H), 6.22 – 6.09 (m, 6H), 5.21 (s, 1H), 1.71 (s, 6H).

HRMS (ESI) m/z: $[M]^+$ Calcd for $C_{45}H_{37}IrN_4O_2$ 858.2543; Found 858.2545.

***[Ir(tbim)$_2$(acac)]*:** crude product was pure.

Yellow powder, yield: 55%.

^{1}H NMR(DMSO-d_6) δ, ppm.: 7.79 (d, J = 7.9 Hz, 2H), 7.58 – 7.54 (m, 2H), 7.44 (d, J = 8.4 Hz, 2H), 7.40 – 7.27 (m, 10H), 7.21 – 7.17 (m, 4H), 6.67 (dd, J = 8.3, 2.1 Hz, 2H), 6.31 (d, J = 2.0 Hz, 2H), 6.17 (d, J = 17.7 Hz, 2H), 6.05 (d, J = 17.7 Hz, 2H), 5.18 (s, 1H), 1.71 (s, 6H), 0.80 (s, 18H).

HRMS (ESI) m/z: $[M]^+$ Calcd for $C_{53}H_{53}IrN_4O_2$ 970.3797; Found 970.3813.

The signal of $[M]^+$ ion is overlapped with the $[M+H]^+$ ion.

***[Ir(cbim)$_2$(acac)]*:** the complex was purified by column chromatography (Al_2O_3, eluent: dichloromethane → dichloromethane:methanol 20:1 vol.)

Yellow powder, yield: 18%.

^{1}H NMR(CD_2Cl_2) δ, ppm.: 7.65 (d, J = 8.3 Hz, 2H), 7.50 (d, J = 8.0 Hz, 2H), 7.43 – 7.31 (m, 12H), 7.20 (d, J = 7.6 Hz, 4H), 6.75 (d, J = 8.3 Hz, 2H), 6.34 (s, 2H), 6.01 – 5.93 (m, 4H), 1.86 (s, 6H).

N.b. the signal of acetylacetonate resonance at c.a. 5.35 ppm is overlapped with the residual dichloromethane signal.

HRMS (ESI) m/z: $[M]^+$ Calcd for $C_{45}H_{35}Cl_2IrN_4O_2$ 926.1749; Found 926.1742.

***[Ir(mbim)$_2$(acac)]*:** the reaction mixture contained small amount of precipitate, the crystalline solid appeared after slow evaporation of acetonitrile, it was filtered in vacuo, thoroughly washed with deionized water and dried in vacuo.

Yellow powder, yield: 45%.

^{1}H NMR($CDCl_3$) δ, ppm.: 7.74 – 7.70 (m, 2H), 7.40 – 7.37 (m, 2H), 7.32 – 7.28 (m, 10H), 7.26 – 7.22 (m, 4H), 6.97 (s, 2H), 5.98 – 5.90 (m, 2H), 5.89 (s, 2H), 5.86 – 5.78 (m, 2H), 5.23 (s, 1H), 3.47 (s, 6H), 3.22 (s, 6H), 1.84 (s, 6H).

HRMS (ESI) m/z: $[M]^+$ Calcd for $C_{49}H_{45}IrN_4O_6$ 978.2969; Found 978.2965.

***[Ir(dcbim)$_2$(acac)]*:** crude product was pure.

Yellow powder, yield: 59%.

^{1}H NMR($CDCl_3$) δ, ppm.: 7.82 (s, 2H), 7.48 – 7.46 (m, 4H), 7.39 – 7.34 (m, 6H), 7.24 (s, 2H), 7.22 (s, 2H), 6.72 (t, J = 7.7 Hz, 2H), 6.64 (t, J = 7.7 Hz, 2H), 6.46 (d, J = 7.9 Hz, 2H), 5.93 (d, J = 17.5 Hz, 2H), 5.84 (d, J = 17.5 Hz, 2H), 5.25 (s, 1H), 1.85 (s, 6H).

HRMS (ESI) m/z: $[M]^+$ Calcd for $C_{45}H_{33}Cl_4IrN_4O_2$ 996.0951; Found 996.0943.

***[Ir(tdcbim)$_2$(acac)]*:** the complex was purified by column chromatography (Al_2O_3, eluent: dichloromethane – hexane 1:3 vol.)

Yellow powder, yield: 37%.

^{1}H NMR($CDCl_3$) δ, ppm.: 7.87 (s, 2H), 7.45 (s, 2H), 7.36 – 7.32 (m, 8H), 7.25 – 7.22 (m, 4H), 6.75 (dd, J = 8.3, 2.0 Hz, 2H), 6.47 (d, J = 2.0 Hz, 2H), 5.97 – 5.90 (m, 2H), 5.79 – 5.73 (m, 2H), 5.24 (s, 1H), 1.86 (s, 6H), 0.94 (s, 18H).

HRMS (ESI) m/z: $[M]^+$ Calcd for $C_{53}H_{49}Cl_4IrN_4O_2$ 1108.2206; Found 1108.2227.

***[Ir(tcbim)$_2$(acac)]*:** crude product was pure.

Yellow powder, yield: 57%.

^{1}H NMR(DMSO-d6) δ, ppm.: 8.44 (s, 2H), 7.66 (d, J = 8.6 Hz, 2H), 7.58 (s, 2H), 7.33 (t, J = 7.4 Hz, 6H), 7.26 (d, J = 7.4 Hz, 2H), 7.08 (s, 2H), 7.06 (s, 2H), 6.80 (dd, J = 8.4, 2.2 Hz, 2H), 6.21 (s, 4H), 6.06 (d, J = 2.2 Hz, 2H), 5.38 (s, 1H), 1.77 (s, 6H).

HRMS (ESI) m/z: $[M]^+$ Calcd for $C_{45}H_{30}Cl_6IrN_4O_2$ 1063.0085; Found 1063.0147.

The signal of $[M]^+$ ion is overlapped with the $[M+H]^+$ ion.

***[Ir(dmbim)$_2$(acac)]*:** the complex was purified by recrystallization from dichloromethane – hexane 1:1 vol.

Yellow powder, yield: 69%.

^{1}H NMR($CDCl_3$) δ, ppm.: 7.53 (s, 2H), 7.40 – 7.28 (m, 10H), 7.24 (s, 2H), 7.14 (s, 2H), 6.66 – 6.61 (m, 2H), 6.57 – 6.51 (m, 2H), 6.49 – 6.45 (m, 2H), 5.92 (d, J = 17.4 Hz, 2H), 5.84 (d, J = 17.4 Hz, 2H), 5.21 (s, 1H), 2.37 (s, 6H), 2.34 (s, 6H), 1.83 (s, 6H).

HRMS (ESI) m/z: $[M]^+$ Calcd for $C_{49}H_{45}IrN_4O_2$ 914.3172; Found 914.3184.

The signal of $[M]^+$ ion is overlapped with the $[M+H]^+$ ion.

***[Ir(mnim)$_2$(acac)]*:** the complex was purified by recrystallization from dichloromethane – acetonitrile 1:1 vol.

Orange powder, yield: 72%.

^{1}H NMR(CD_2Cl_2) δ, ppm.: 8.17 (s, 2H), 7.97 (d, J = 8.0 Hz, 2H), 7.93 (d, J = 7.7 Hz, 2H), 7.86 (s, 2H), 7.54 – 7.33 (m, 16H), 6.61 (d, J = 8.0 Hz, 2H), 6.42 (s, 2H), 6.13 (d, J = 17.5 Hz, 2H), 6.05 (d, J = 17.6 Hz, 2H), 1.99 (s, 6H), 1.96 (s, 6H).

N.b. the signal of acetylacetonate resonance at c.a. 5.35 ppm is overlapped with the residual dichloromethane signal.

HRMS (ESI) m/z: $[M]^+$ Calcd for $C_{55}H_{45}IrN_4O_2$ 986.3171; Found 986.3170.

Insufficient solubility of these complexes prevented acquisition of meaningful ^{13}C NMR spectra.

Complexes containing diimine ancillary ligands were prepared as follows (bpy – 2,2'-bipyridine, dmbpy – 4,4'-dimethyl-2,2'-bipyridine, dcmbpy – dimethyl 2,2'-bipyridine-4,4'-dicarboxylate):

[Ir(phi)$_2$(dmbpy)]: cyclometalated Ir(III) chloride (50 mg, 0.052 mmol), 4,4'-dimethyl-2,2'-bipyridyl (10 mg, 0.104 mmol) were mixed in dry chloroform (5 ml) and ethanol (5 ml), and then 130 μl of 0.5M AgOTf solution in methanol was added, and the mixture was refluxed for 8-10 h under Ar in darkness. The resulting solution was filtered through paper filter, evaporated to dryness, dissolved in dichloromethane, filtered through paper filter again and recrystallized from CH_2Cl_2/hexane 1:1 vol.

Yellow powder, yield 77%.

^{1}H NMR (400 MHz, $CDCl_3$) δ, ppm.: 8.53 (d, J = 8.4 Hz, 2H), 8.41 (d, J = 8.3 Hz, 2H), 8.29 (d, J = 5.7 Hz, 2H), 8.01 (dd, J = 8.2, 0.9 Hz, 2H), 7.94 – 7.83 (m, 2H), 7.82 – 7.77 (m, 2H), 7.65 – 7.58 (m, 2H), 7.50 – 7.43 (m, 4H), 7.36 (d, J = 5.7 Hz, 2H), 7.25 – 7.15 (m, 6H), 7.03 – 6.97 (m, 2H), 6.79 – 6.69 (m, 4H), 6.68 – 6.64 (m, 2H), 6.52 – 6.44 (m, 2H), 2.29 (s, 6H).

HRMS (ESI) m/z: $[M]^+$ Calcd for $C_{66}H_{46}IrN_6$ 1115.3414; Found 1115.3418.

[Ir(phi)$_2$(bpy)]**:** similar to ***[Ir(phi)$_2$(dmbpy)]*** with 2,2'-bipyridyl (8.5 mg, 0.104 mmol). The product was additionally purified by column chromatography (SiO_2, from EtOAC/hexane 20/1 vol. to EtOAc/MeOH 20/1 vol.)

yellow-orange powder, yield 59%

^{1}H NMR (400 MHz, Acetone-d_6) δ 8.80 – 8.72 (m, 4H), 8.63 (d, J = 8.4 Hz, 2H), 8.26 (dd, J = 8.1, 1.0 Hz, 2H), 8.15 (dd, J = 7.8, 1.4 Hz, 2H), 8.10 – 8.02 (m, 9H), 8.01 – 7.98 (m, 3H), 7.94 – 7.86 (m, 2H), 7.60 – 7.52 (m, 2H), 7.40 (dd, J = 7.5, 0.9 Hz, 2H), 7.37 – 7.28 (m, 4H), 7.16 – 7.10 (m, 2H), 6.92 – 6.75 (m, 6H), 6.63 (dd, J = 7.8, 1.2 Hz, 2H).

HRMS (ESI) m/z: $[M]^+$ Calcd for $C_{64}H_{42}IrN_6$ 1087.3100; Found 1087.3105.

[Ir(phi)$_2$(dcmbpy)]: similar to ***[Ir(phi)$_2$(dmbpy)]*** with 4,4'-bis(carbomethoxy)-2,2'-bipyridine (14.8 mg, 0.104 mmol).

red powder, yield 58%.

^{1}H NMR (400 MHz, $CDCl_3$) δ 8.76 (d, J = 5.6 Hz, 2H), 8.56 (d, J = 8.3 Hz, 2H), 8.44 (d, J = 8.5 Hz, 2H), 8.36 – 8.31 (m, 4H), 8.08 (t, J = 7.5 Hz, 2H), 8.02 – 7.96 (m, 4H), 7.94 – 7.88 (m, 2H), 7.87 – 7.82 (m, 2H), 7.81 – 7.76 (m, 2H), 7.51 (t, J = 7.5 Hz, 2H), 7.32 – 7.28 (m, 4H), 7.25 – 7.22 (m, 2H), 7.06 (d, J = 8.4 Hz, 2H), 6.90 – 6.82 (m, 4H), 6.75 (t, J = 7.6 Hz, 2H), 6.62 – 6.56 (m, 2H), 3.96 (s, 6H).

HRMS (ESI) m/z: $[M]^+$ Calcd for $C_{68}H_{46}IrN_6O_4$ 1203.3211; Found 1203.3209.

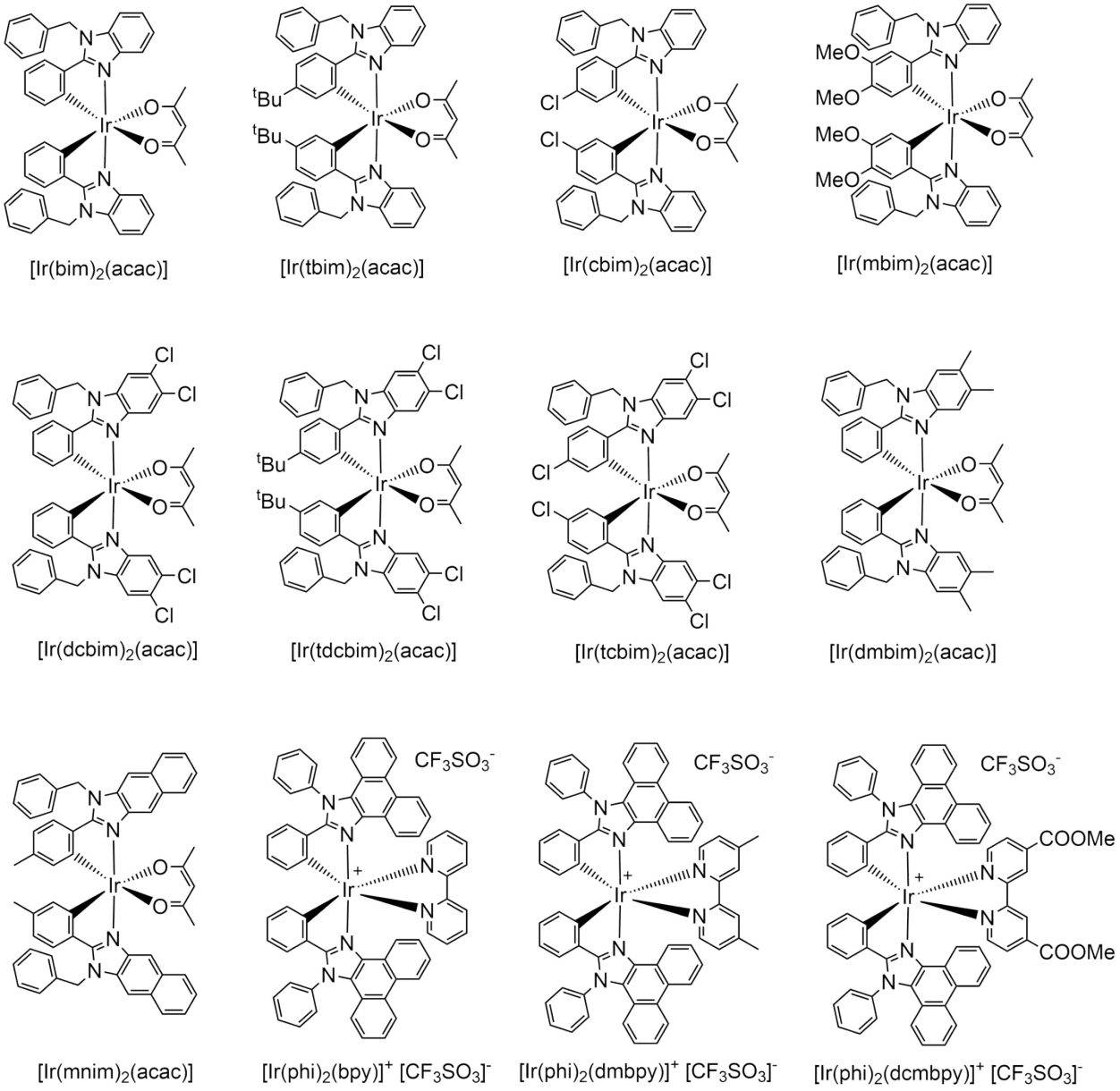

Scheme S1. Structural formulas of the complexes synthesized in this work.

2. NMR and mass spectra.

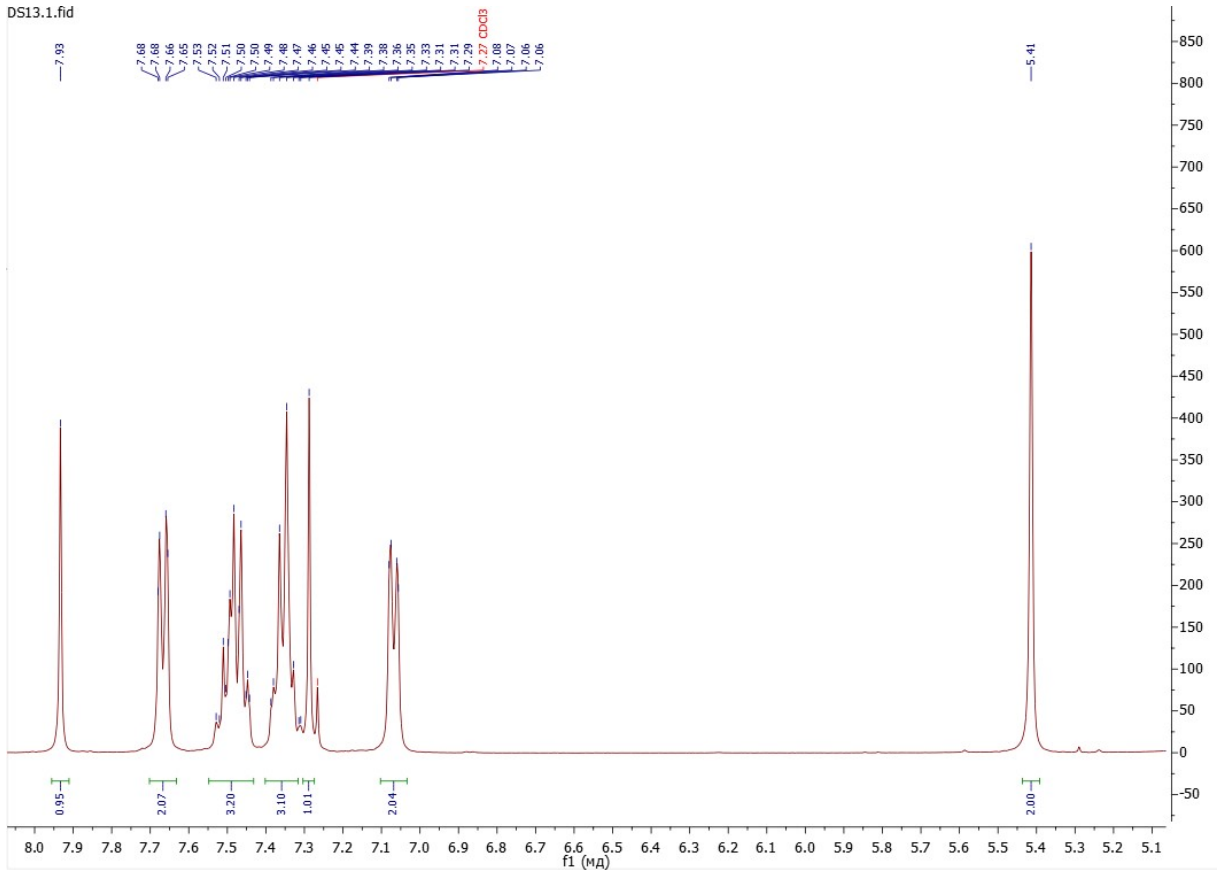

Figure S1. ^{1}H NMR of dcbim (400MHz, $CDCl_3$).

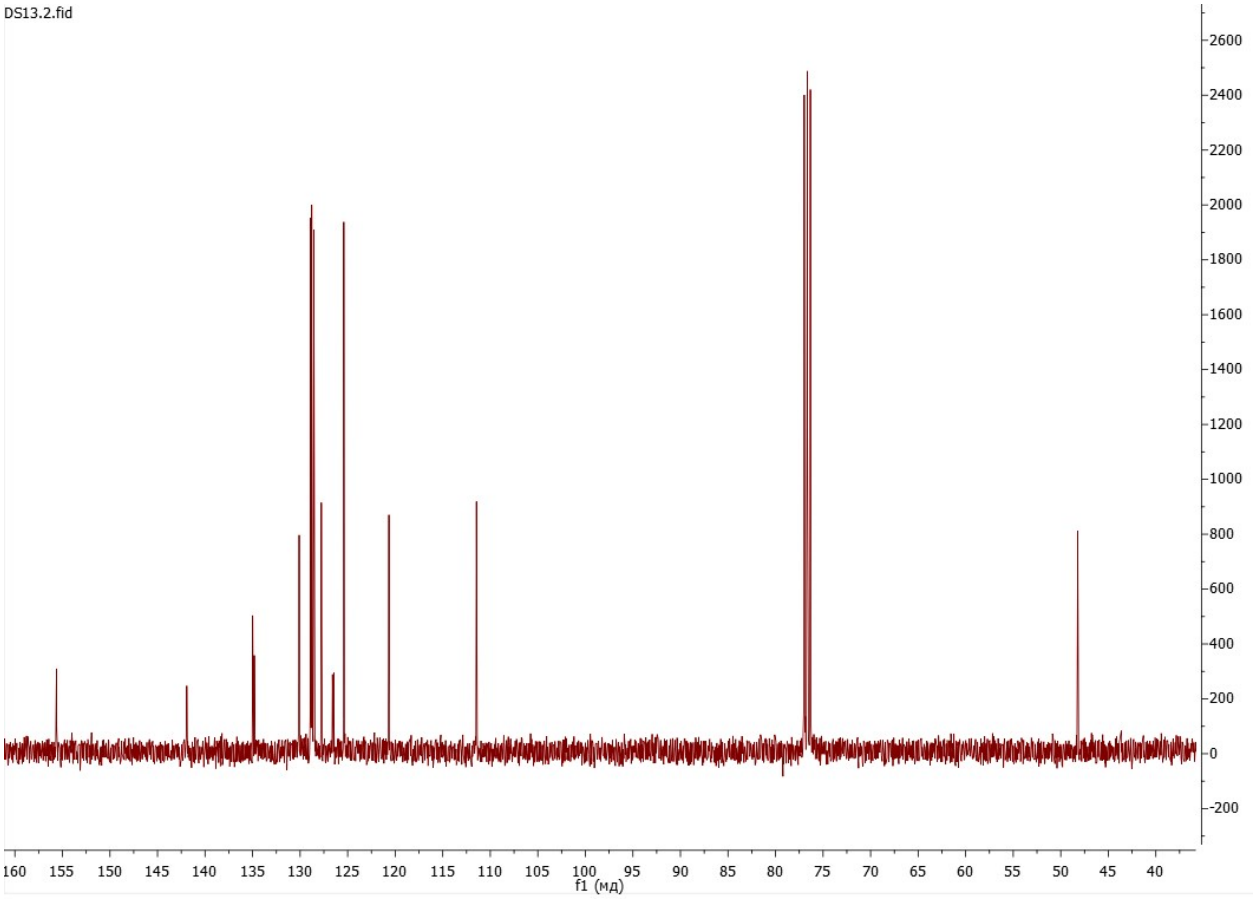

Figure S2. $^{13}C\{^{1}H\}$ NMR of dcbim (100MHz, $CDCl_3$).

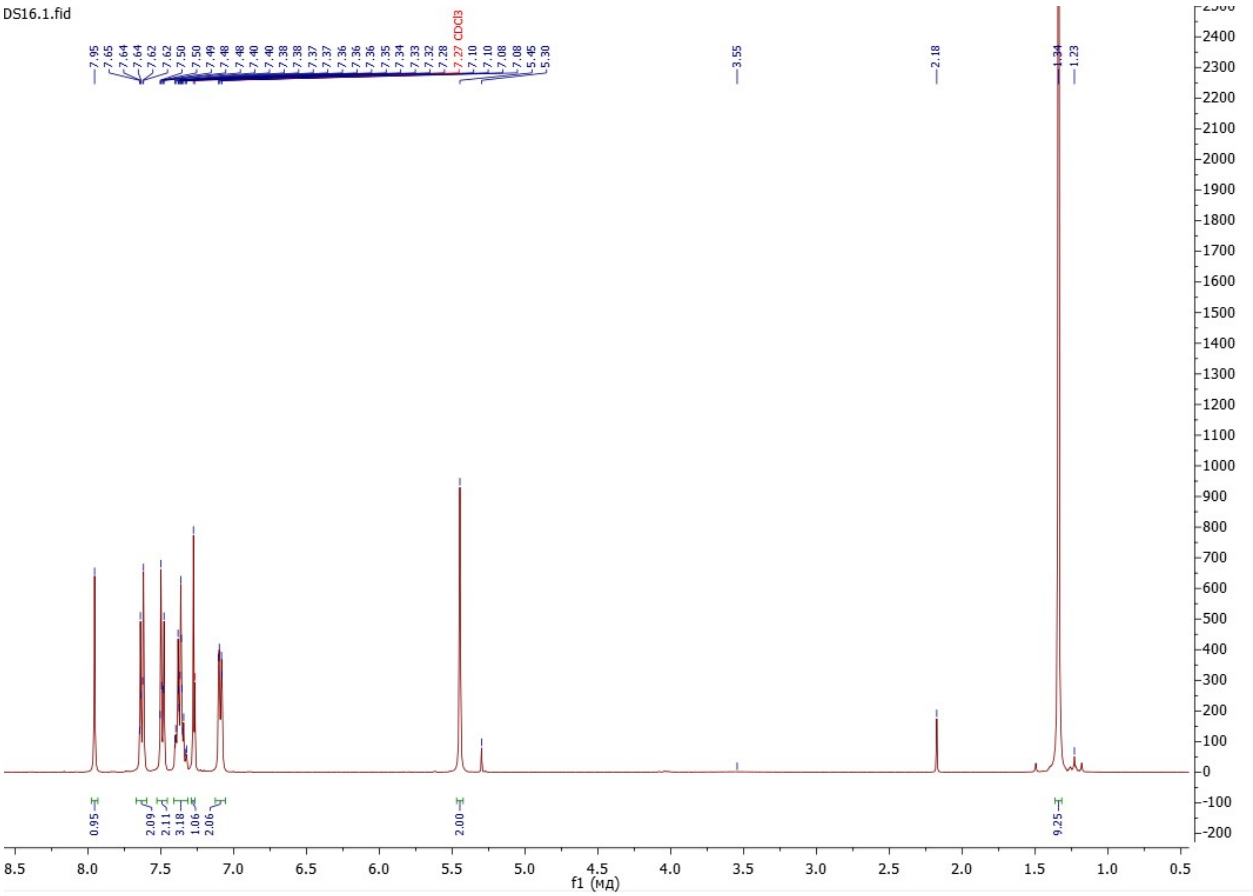

Figure S3. ^{1}H NMR of tdcbim (400MHz, $CDCl_3$).

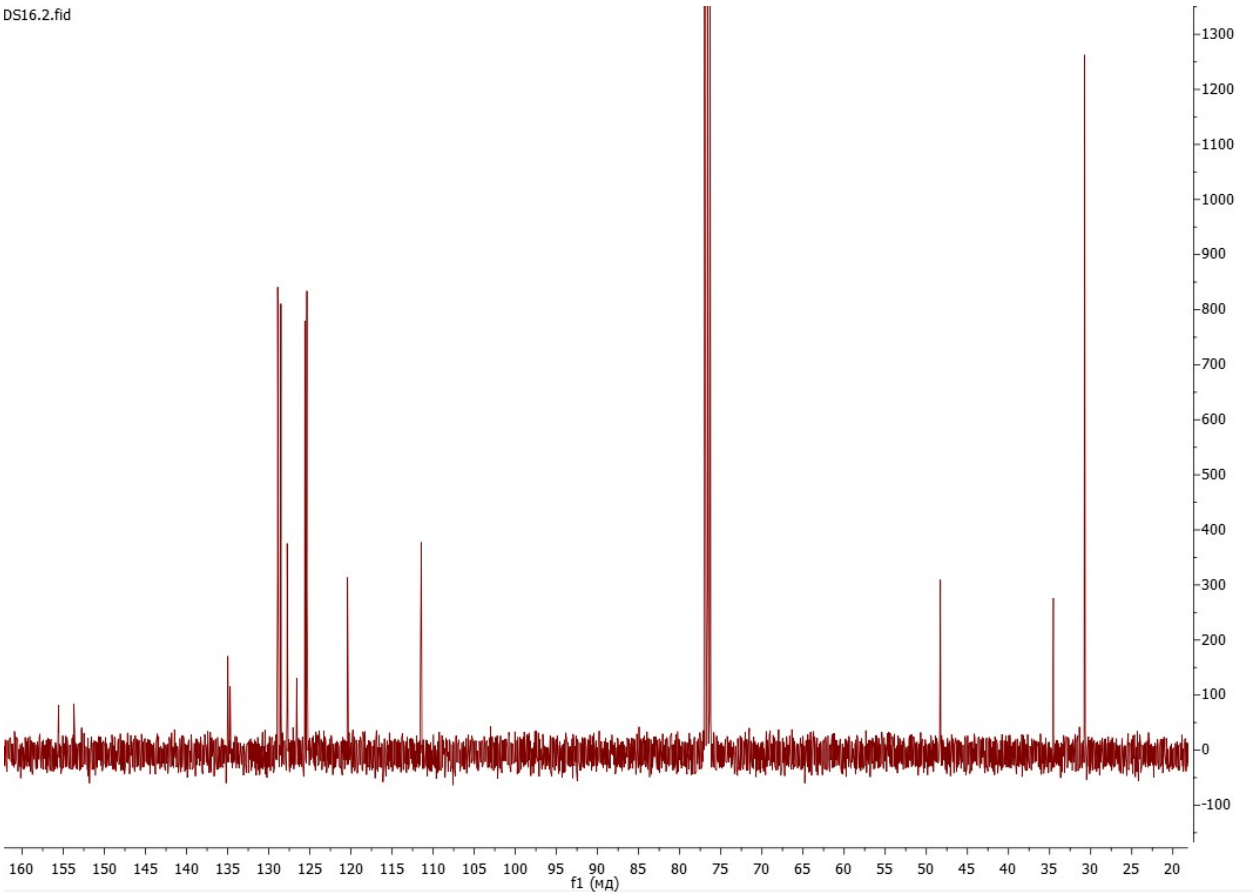

Figure S4. $^{13}C\{^{1}H\}$ NMR of tdcbim (100MHz, $CDCl_3$).

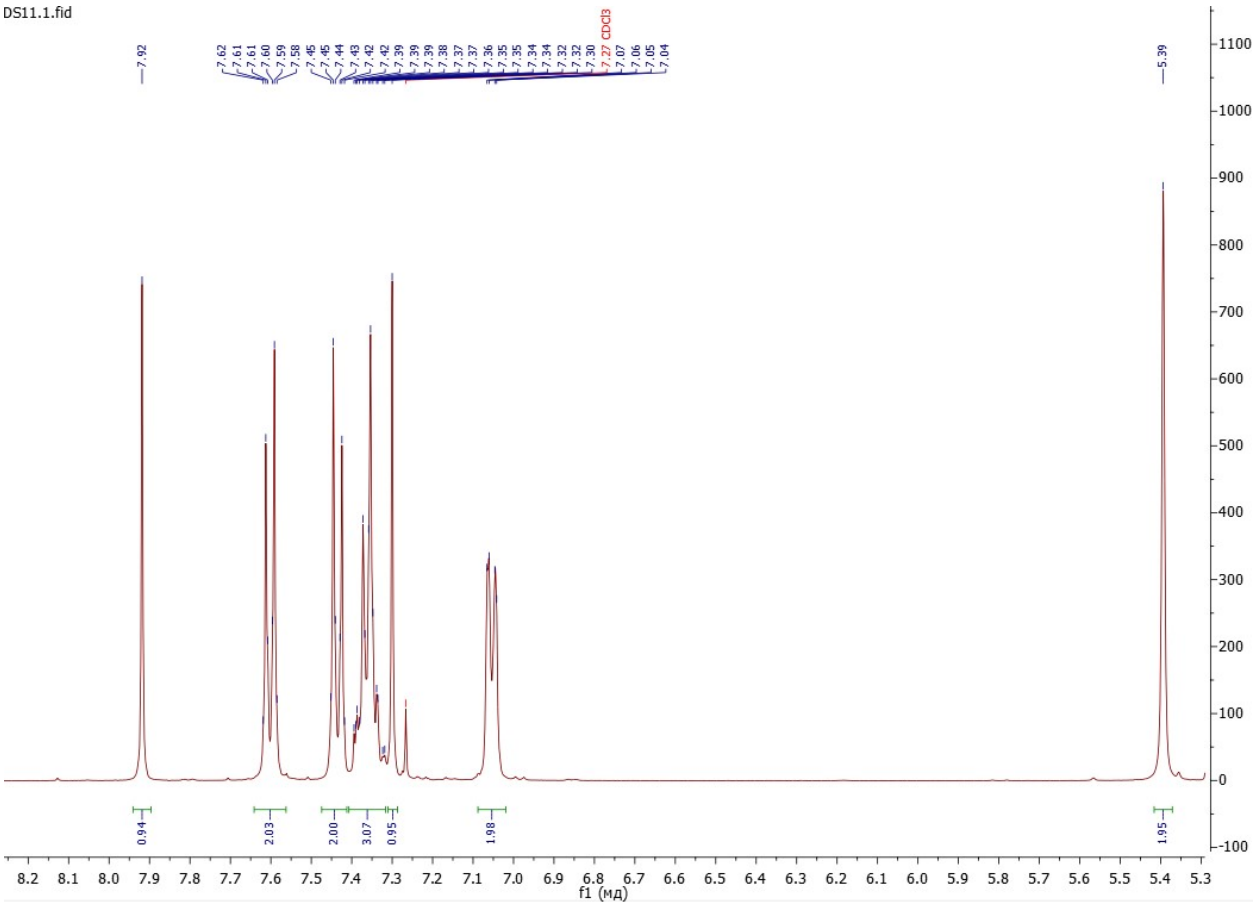

Figure S5. ^{1}H NMR of tcbim (400MHz, $CDCl_3$).

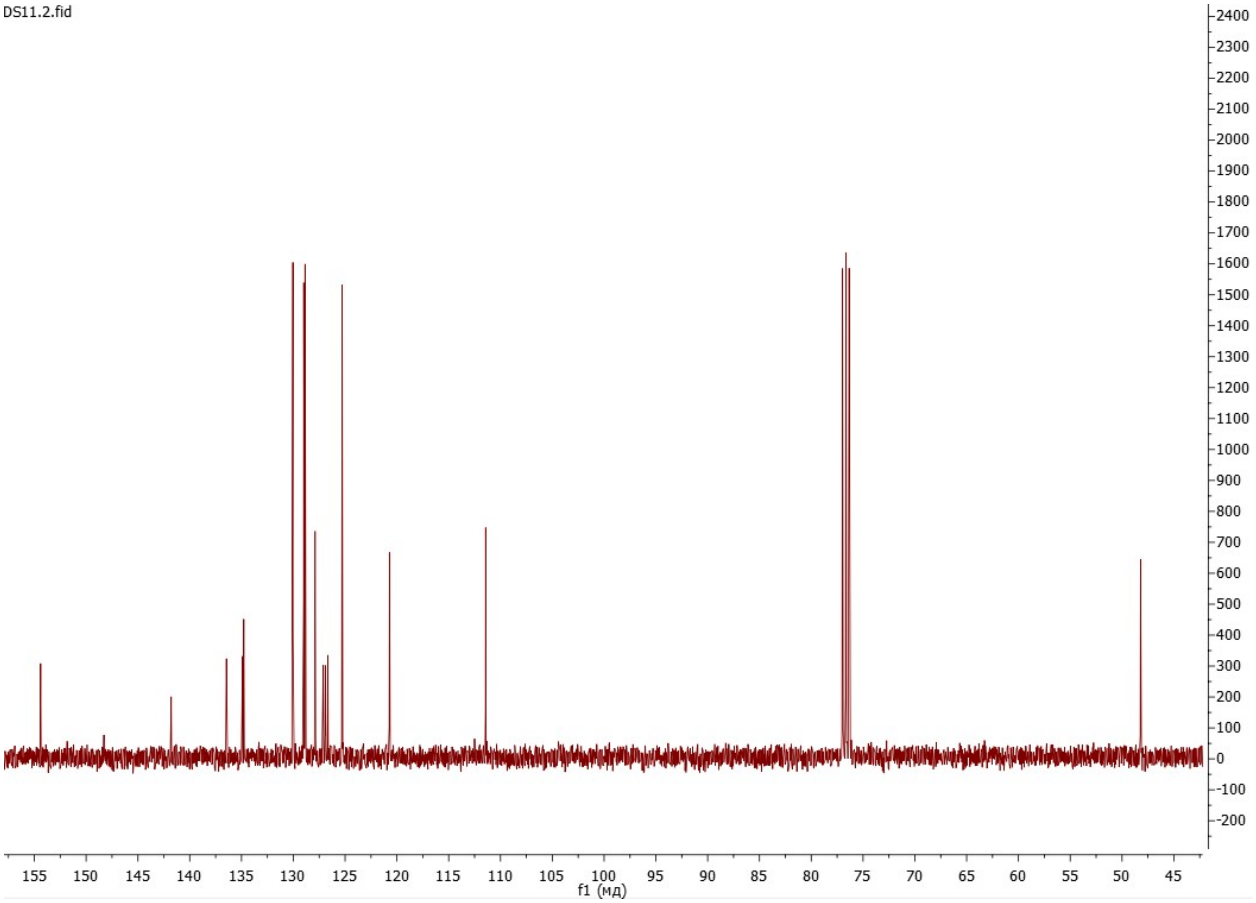

Figure S6. $^{13}C\{^{1}H\}$ NMR of tcbim (100MHz, $CDCl_3$).

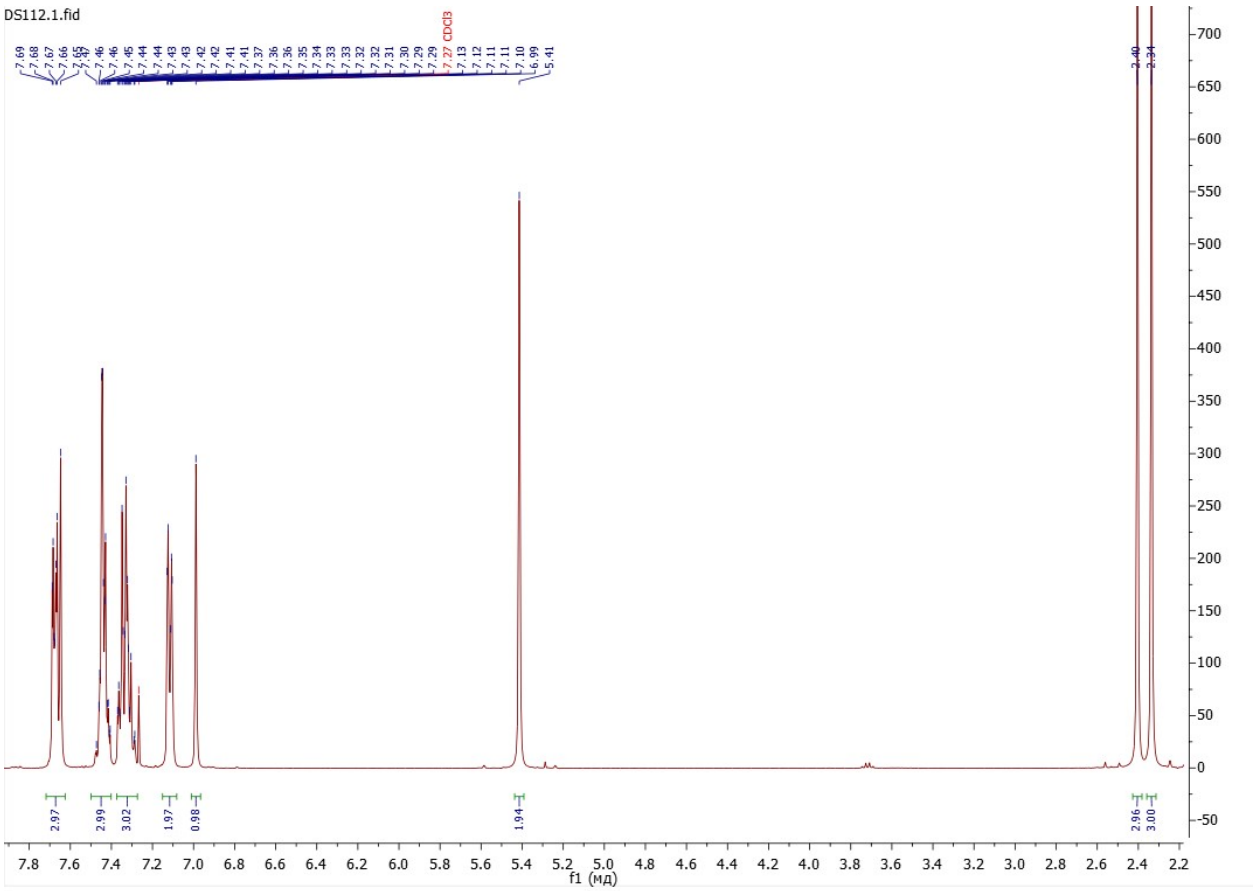

Figure S7. ^{1}H NMR of dmbim (400MHz, $CDCl_3$).

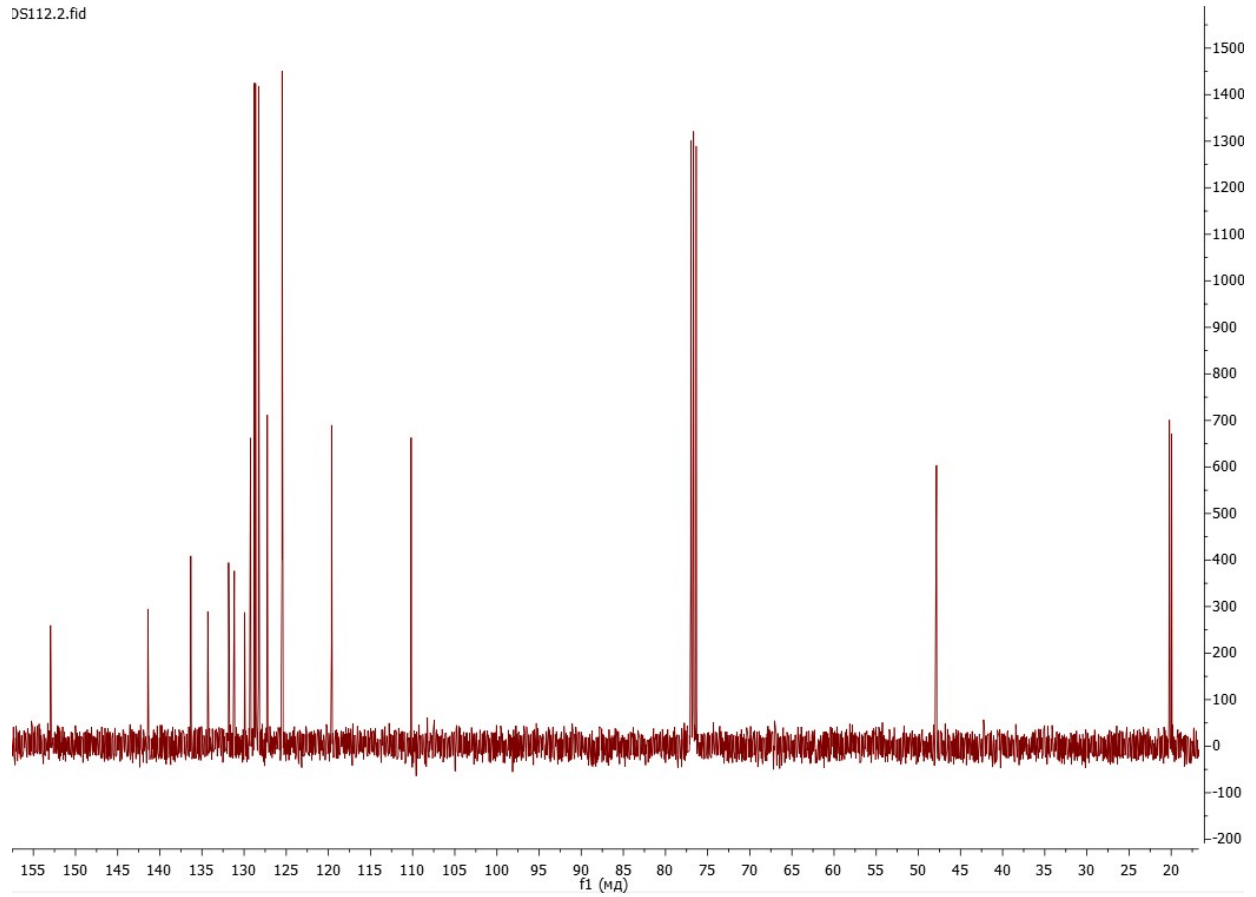

Figure S8. $^{13}C\{^{1}H\}$ NMR of dmbim (100MHz, $CDCl_3$).

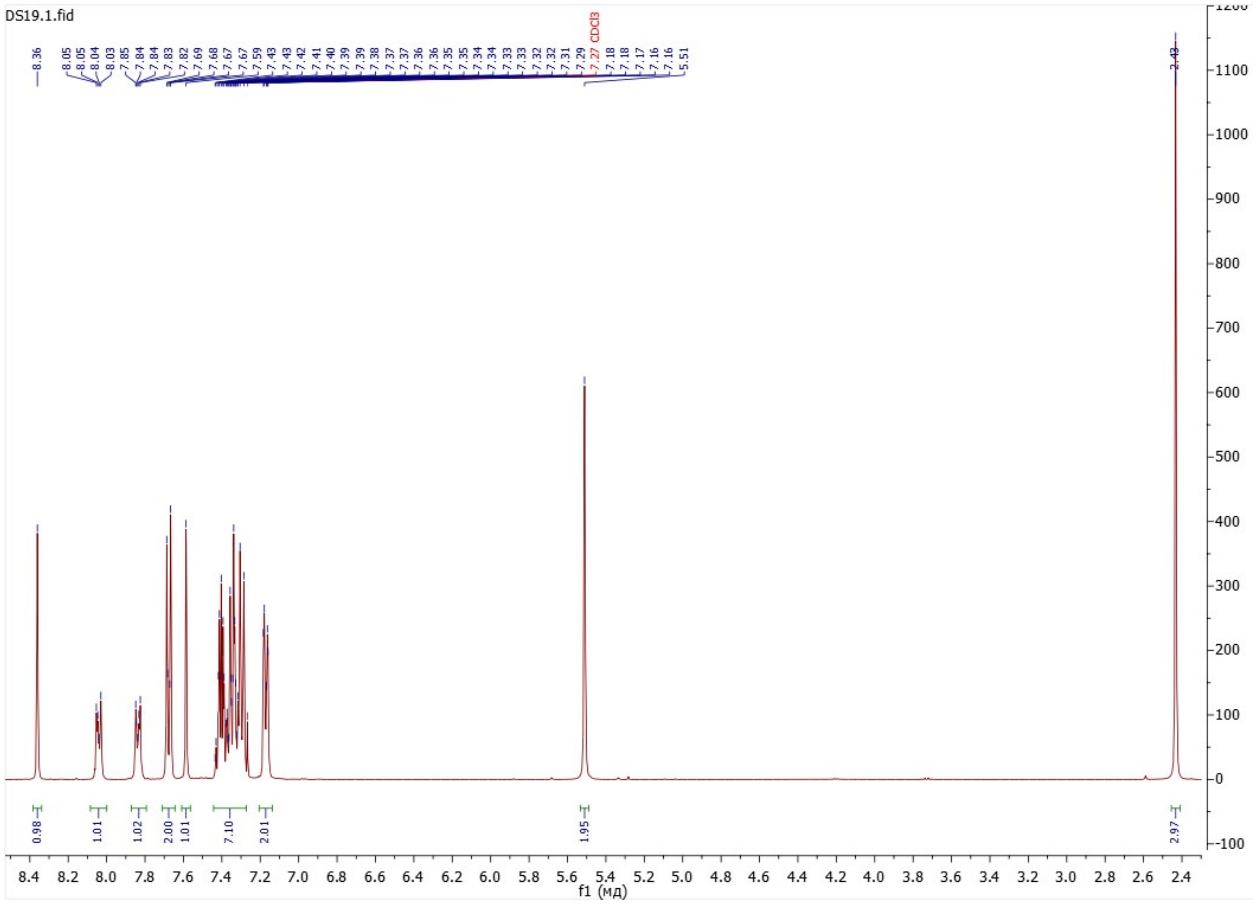

Figure S9. ^{1}H NMR of mnim (400MHz, $CDCl_3$)

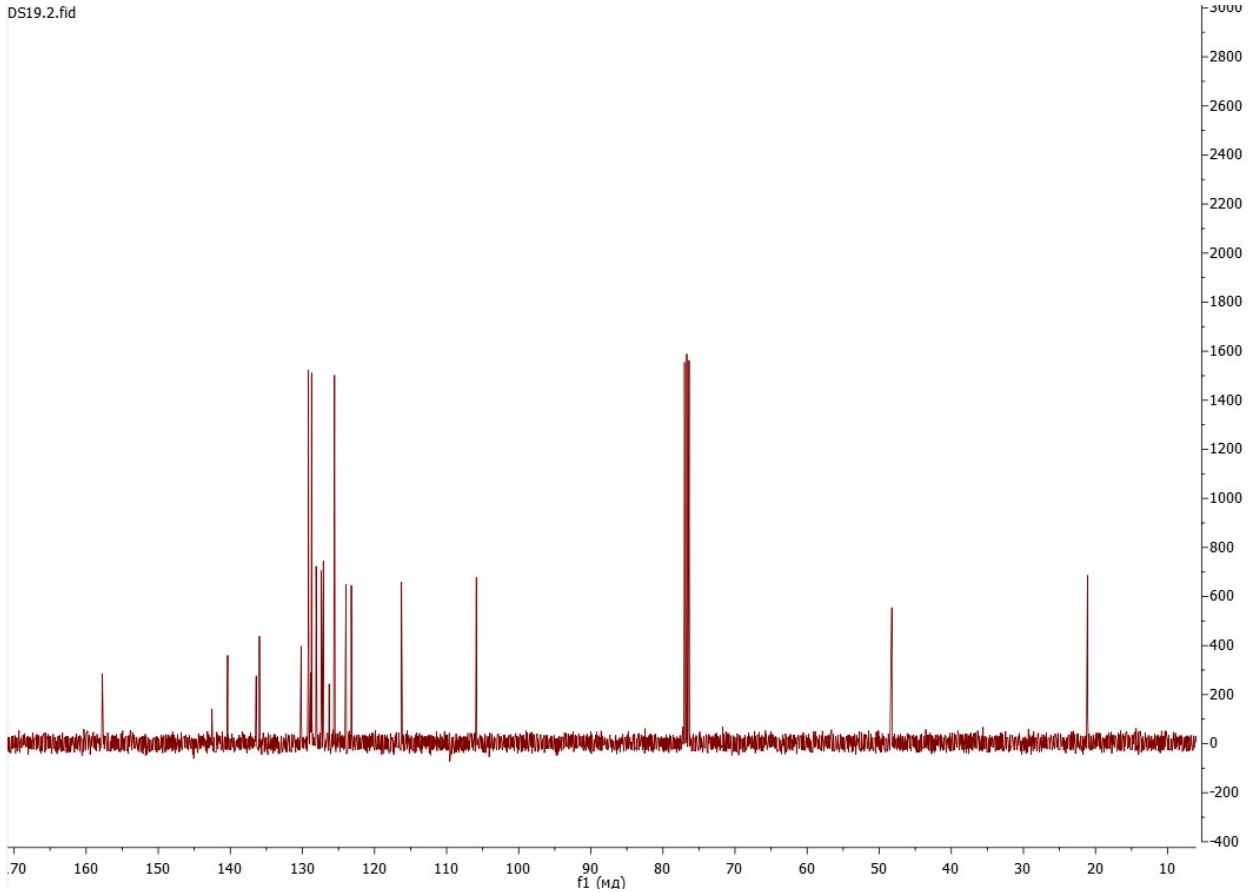

Figure S10. $^{13}C\{^{1}H\}$ NMR of mnim (100MHz, $CDCl_3$).

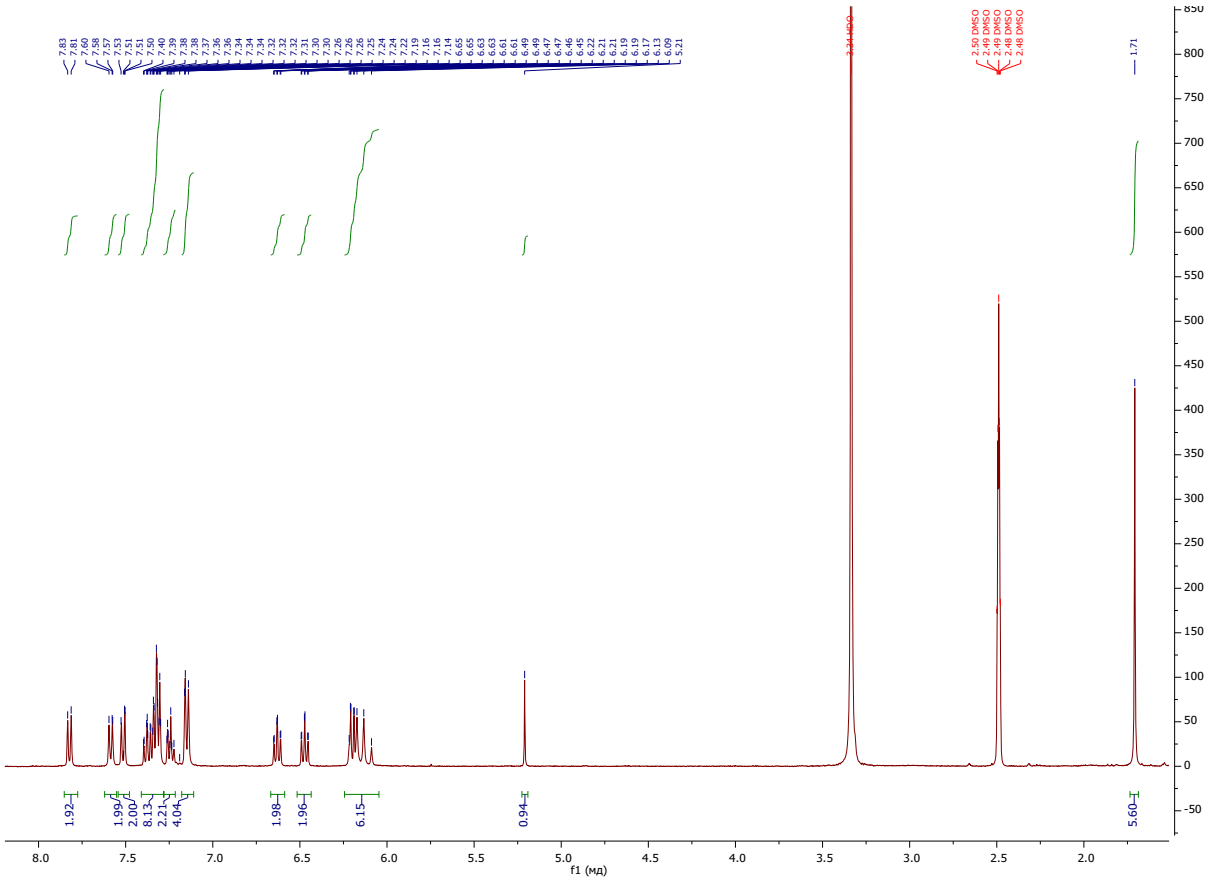

Figure S11. ^{1}H NMR of $[Ir(bim)_2(acac)]$ (400MHz, DMSO-d_6)

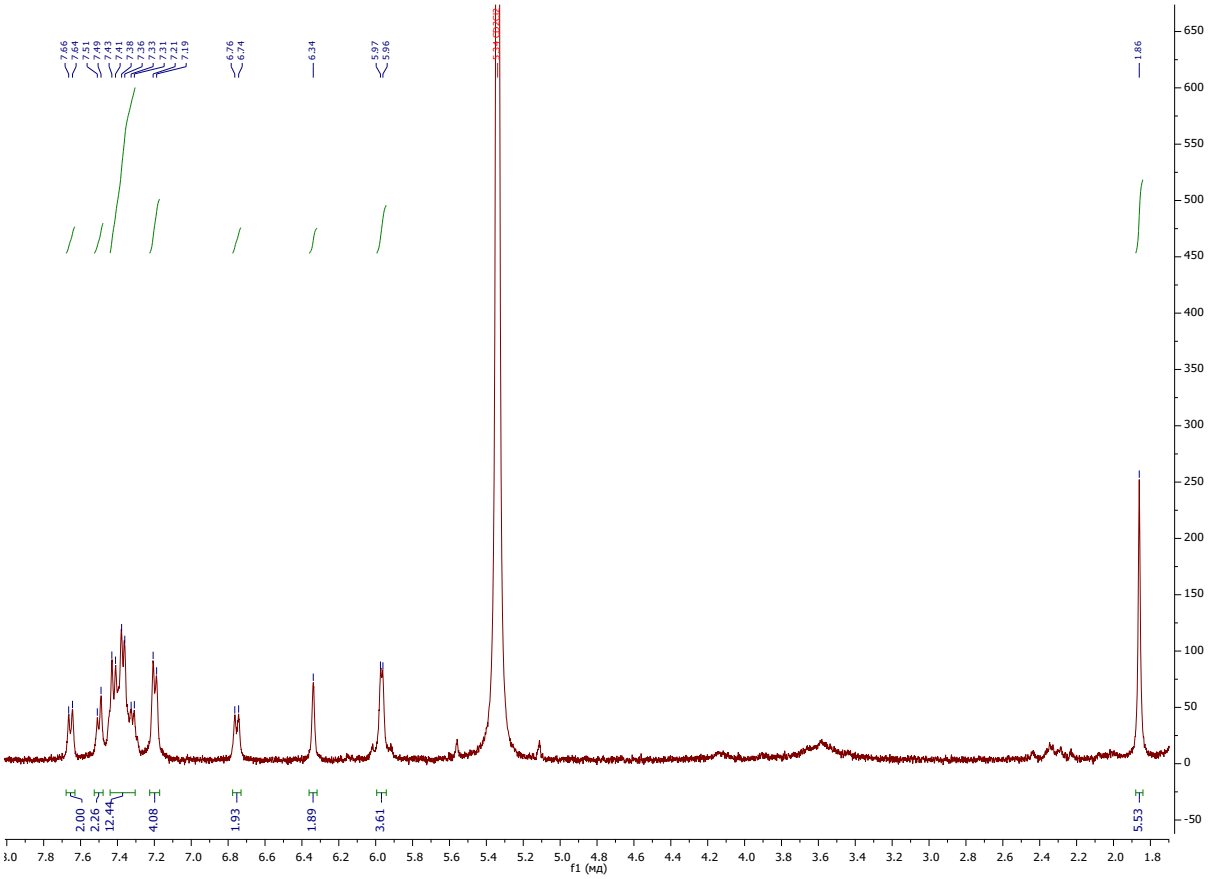

Figure S12. ^{1}H NMR of $[Ir(cbim)_2(acac)]$ (400MHz, CD_2Cl_2)

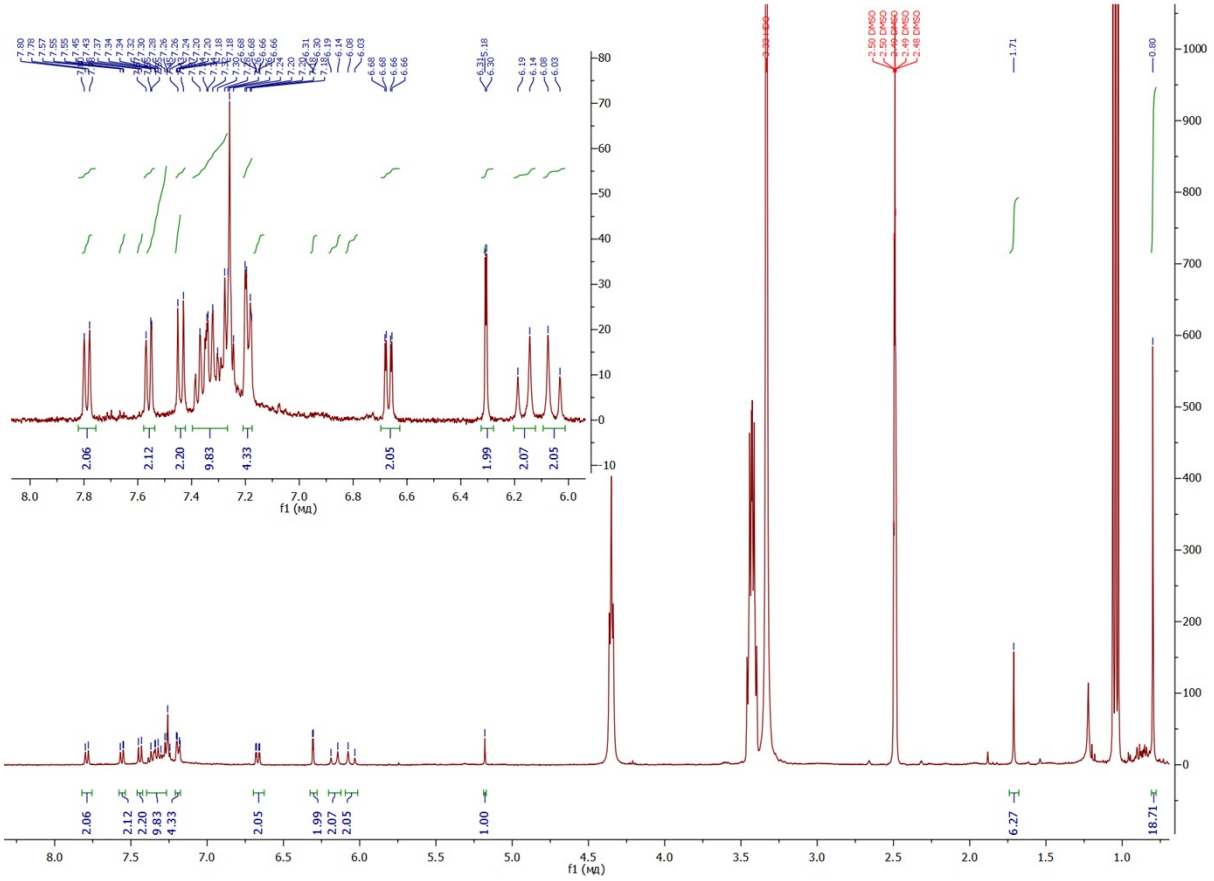

Figure S13. ^{1}H NMR of $[Ir(tbim)_2(acac)]$ (400MHz, DMSO-d_6)

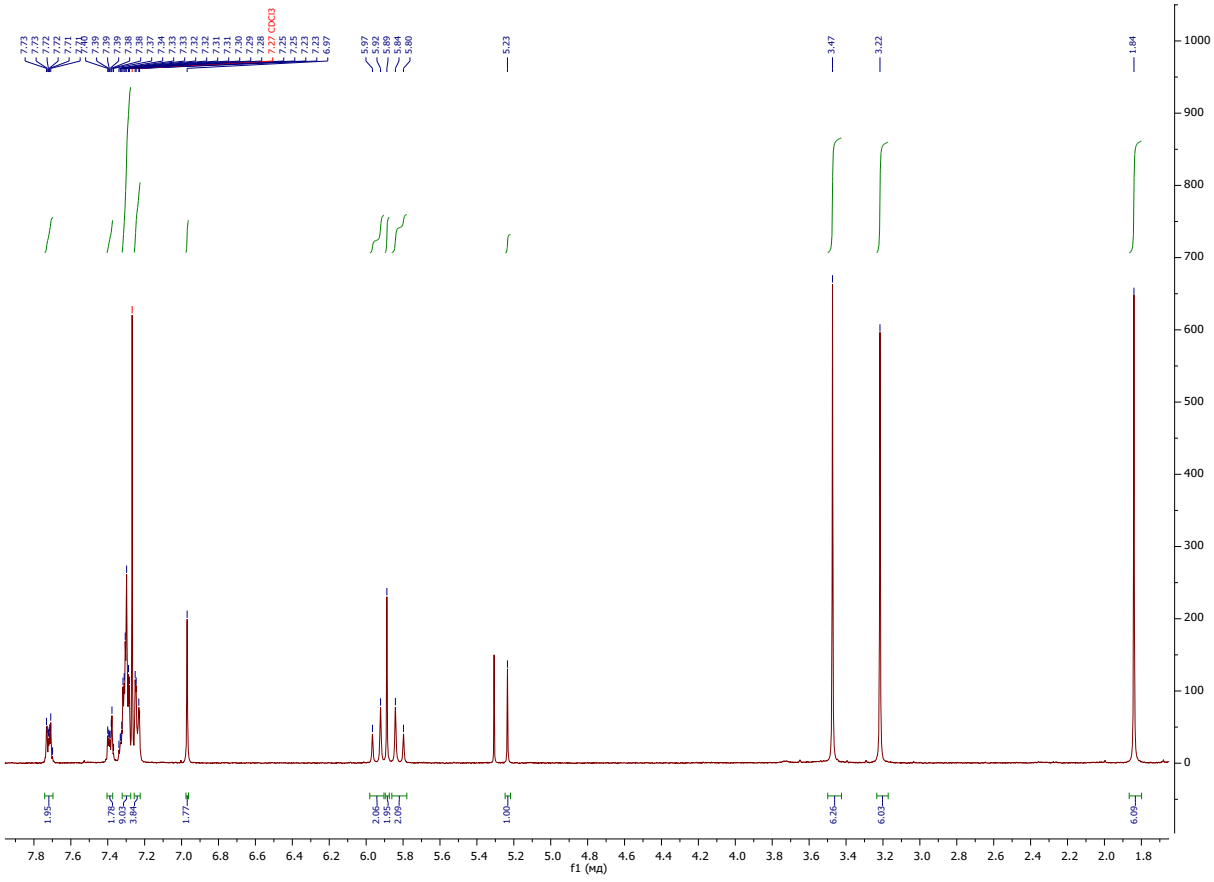

Figure S14. ^{1}H NMR of $[Ir(mbim)_2(acac)]$ (400MHz, $CDCl_3$)

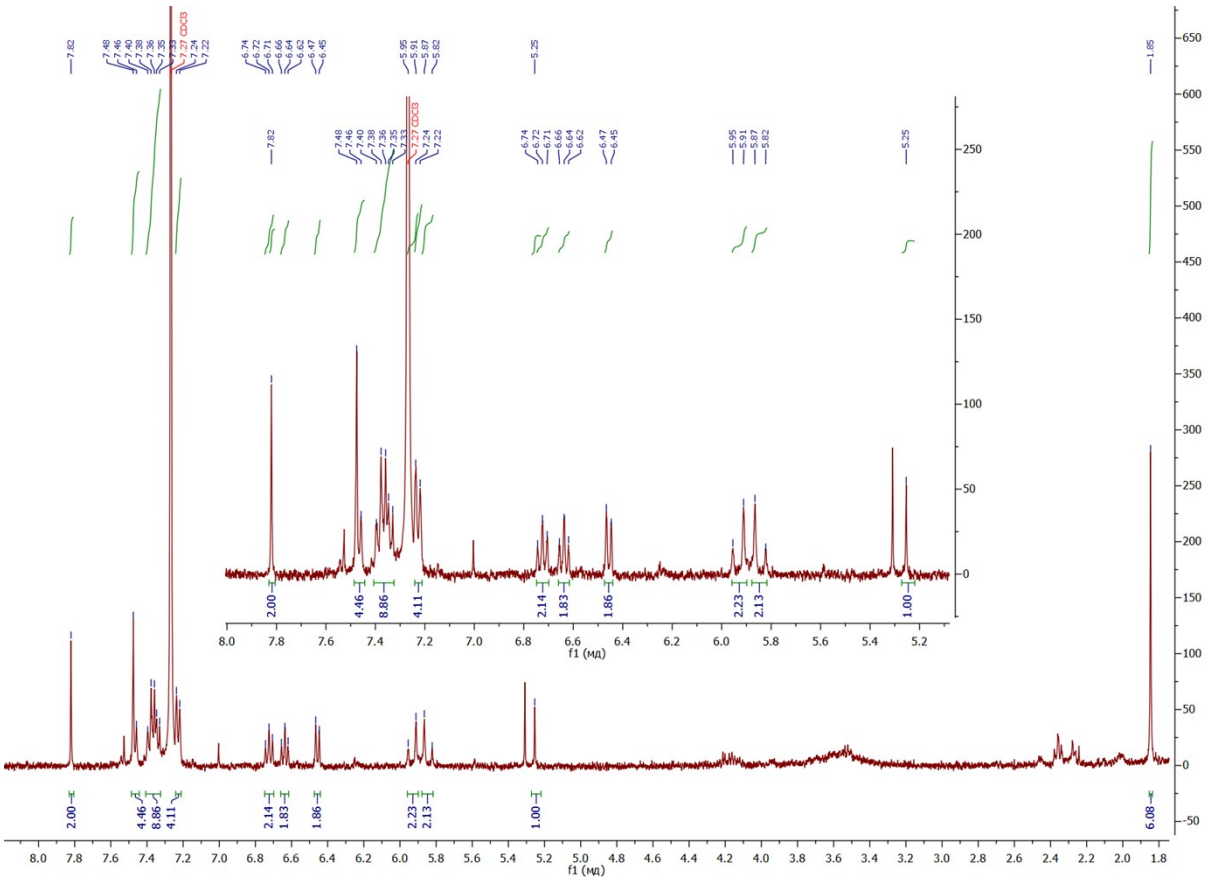

Figure S15. ^{1}H NMR of $[Ir(dcbim)_2(acac)]$ (400MHz, $CDCl_3$)

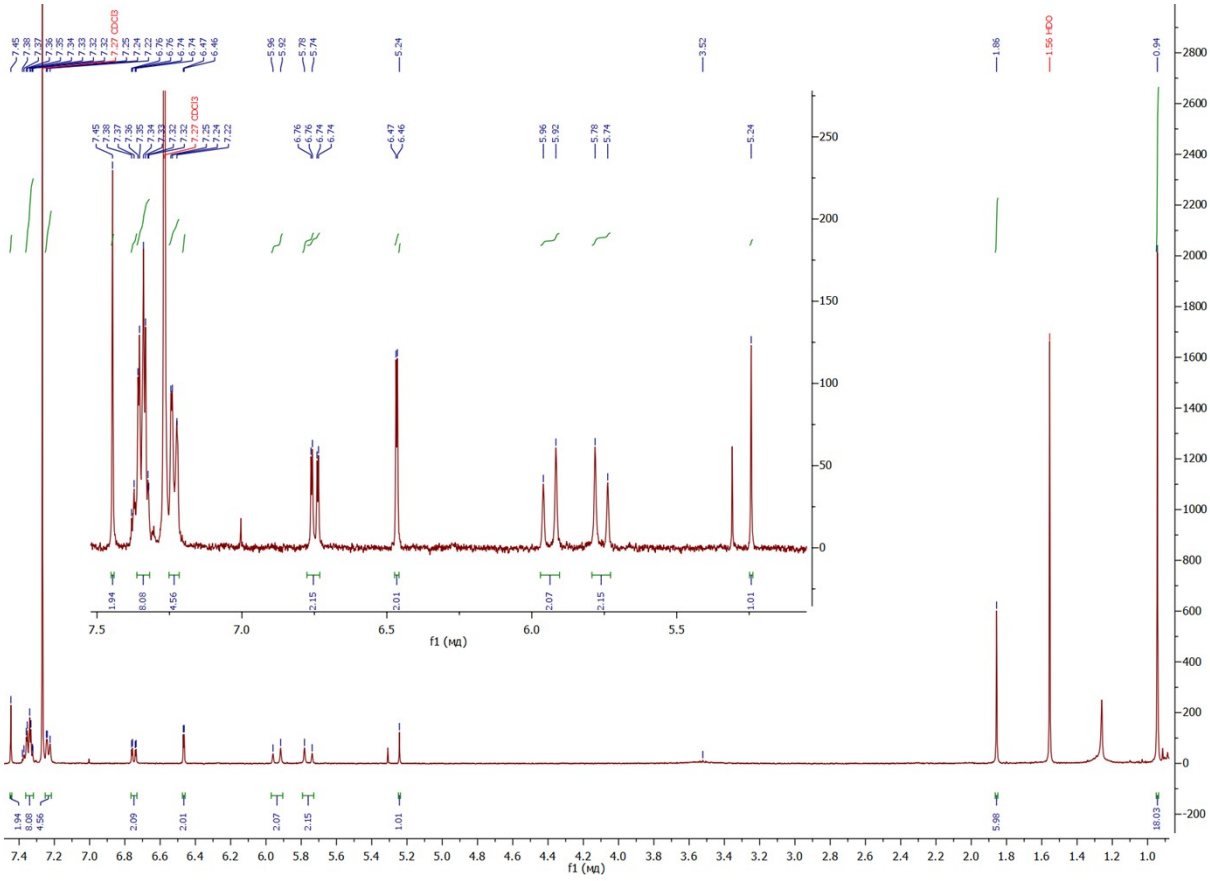

Figure S16. ^{1}H NMR of $[Ir(tdcbim)_2(acac)]$ (400MHz, $CDCl_3$)

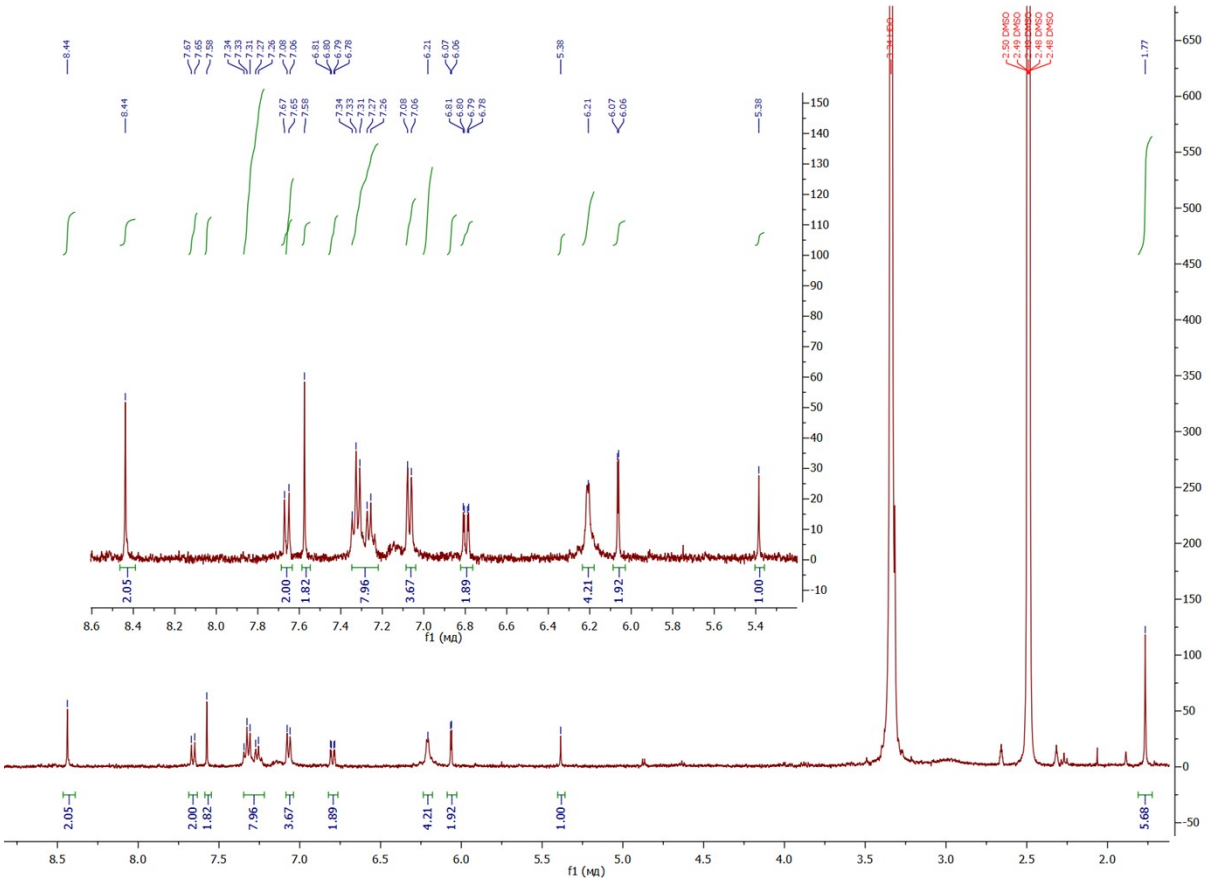

Figure S17. ^{1}H NMR of [Ir(tcbim)$_2$(acac)] (400MHz, DMSO-d$_6$)

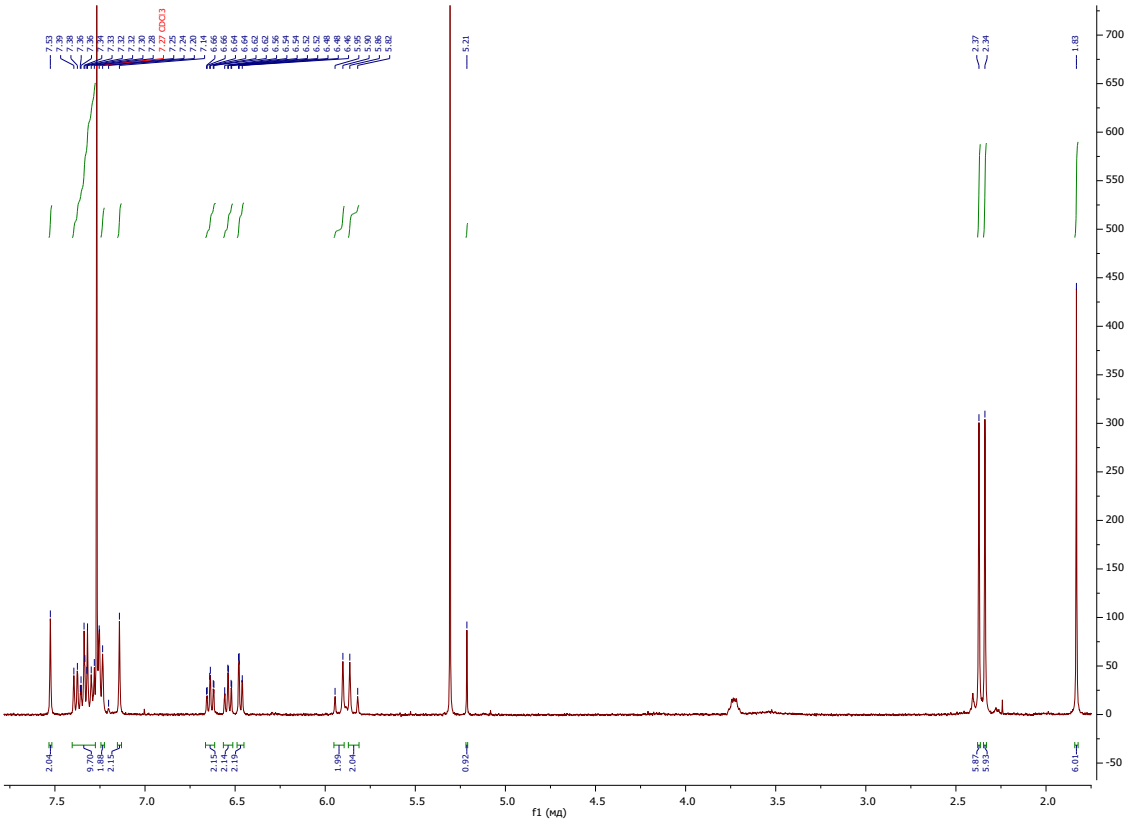

Figure S18. ^{1}H NMR of [Ir(dmbim)$_2$(acac)] (400MHz, CDCl$_3$)

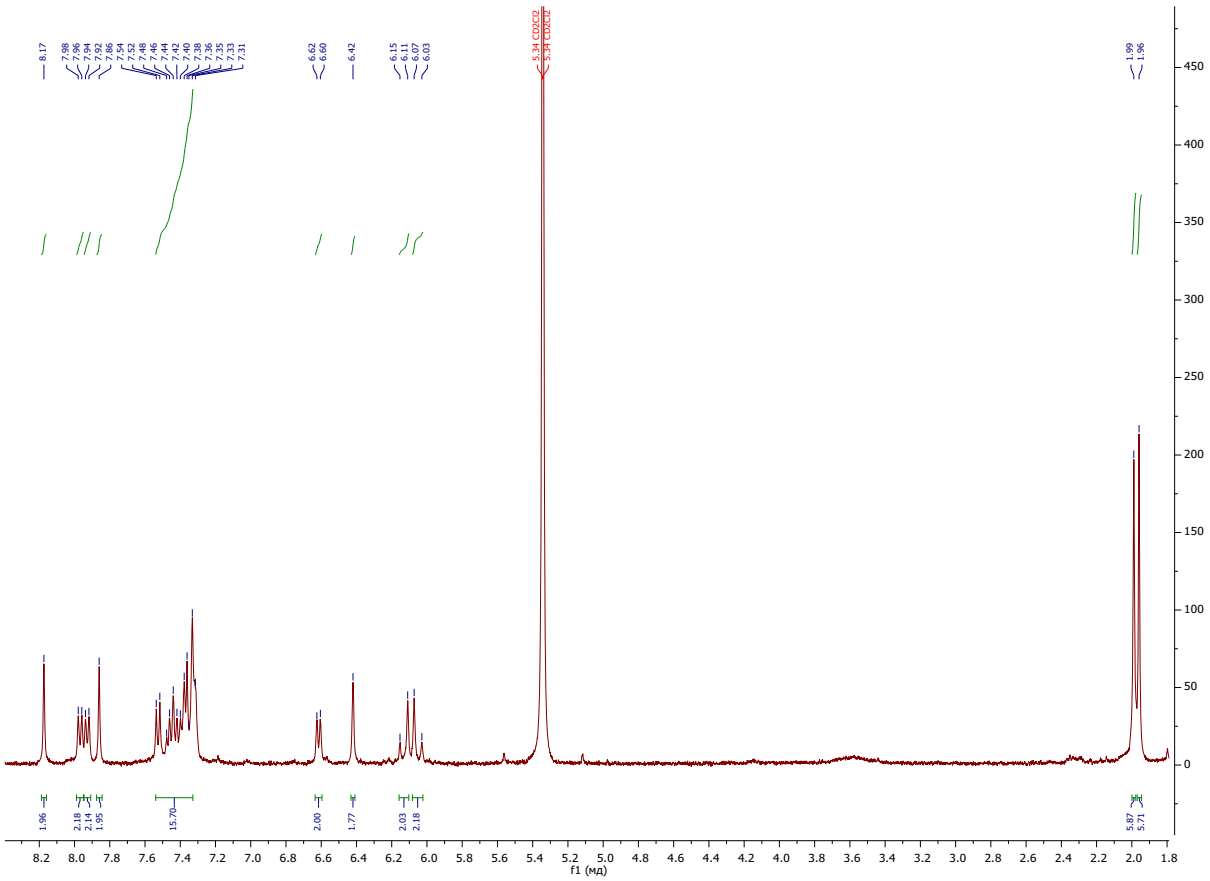

Figure S19. ^{1}H NMR of $[Ir(mnim)_2(acac)]$ (400MHz, CD_2Cl_2)

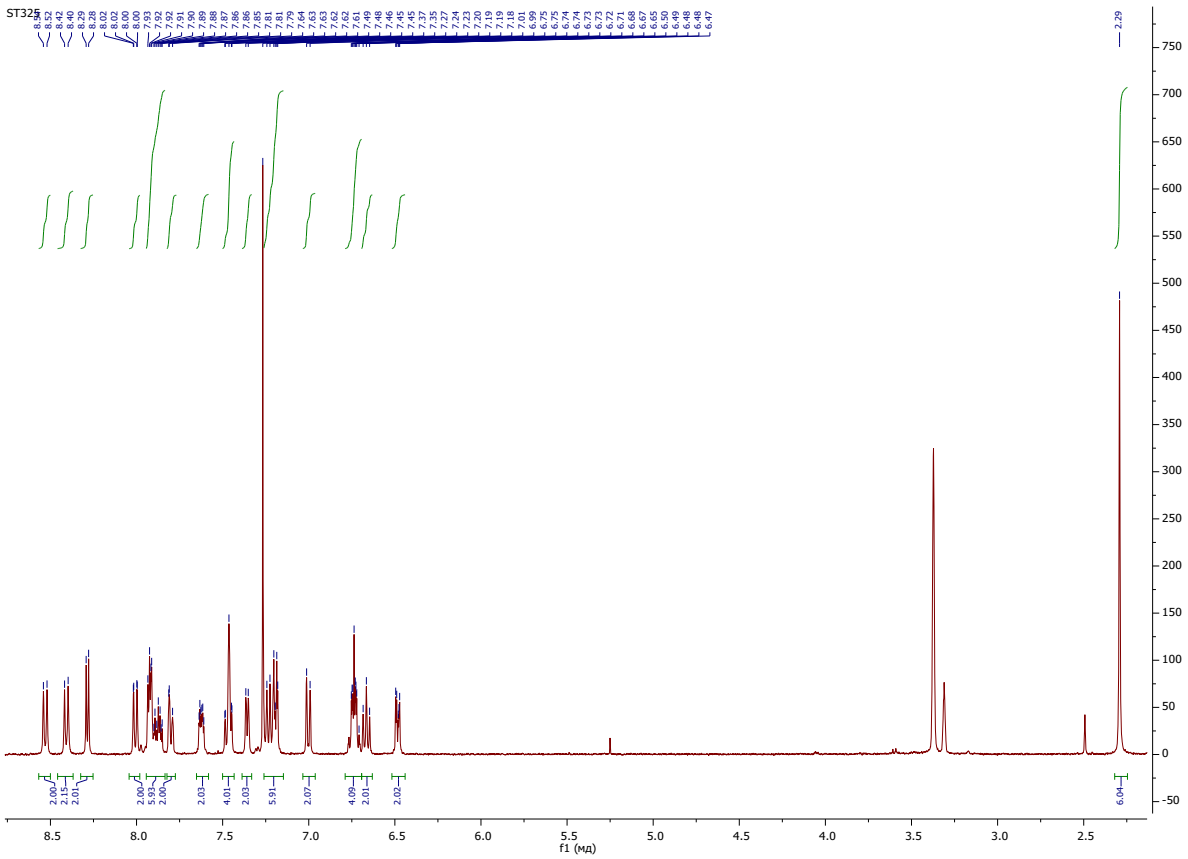

Figure S20. ^{1}H NMR of $[Ir(phi)_2(dmbpy)]$ (400MHz, $CDCl_3$)

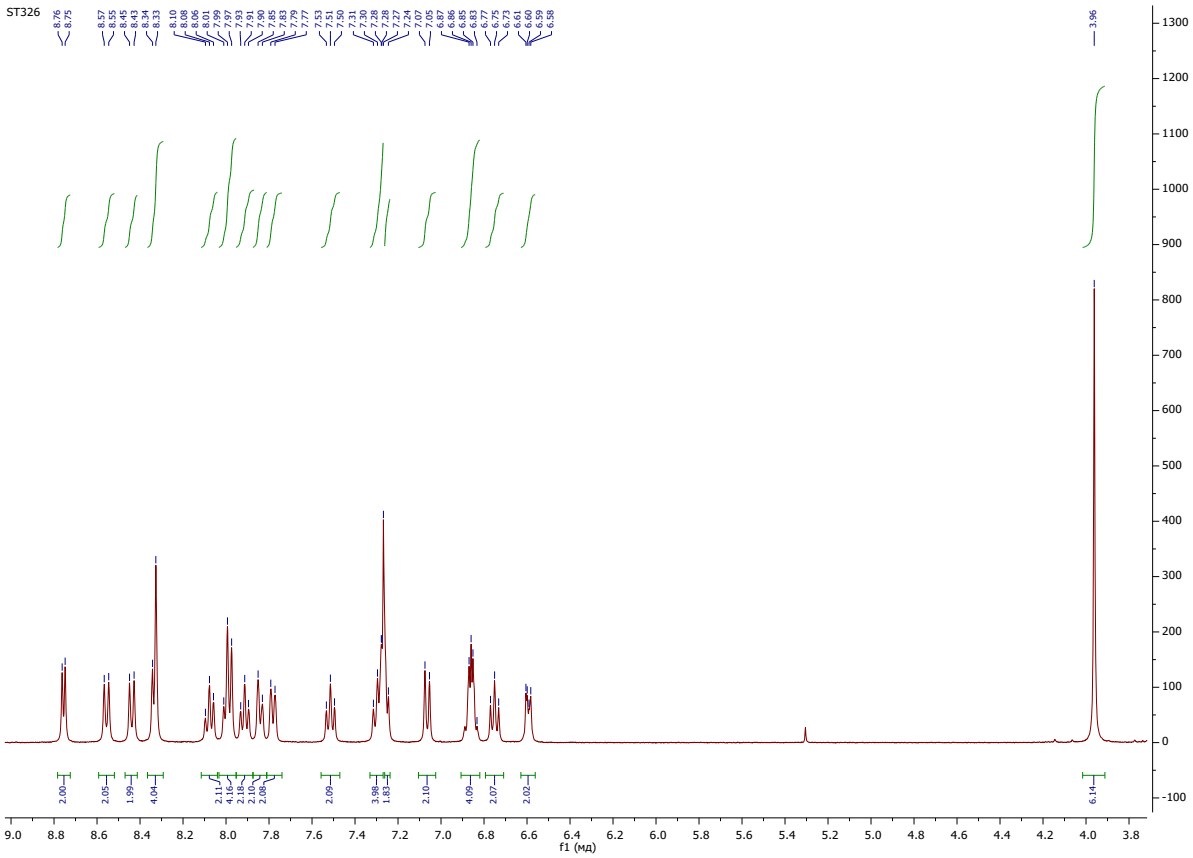

Figure S21. ^{1}H NMR of [Ir(phi)$_2$(dcmbpy)] (400MHz, $CDCl_3$)

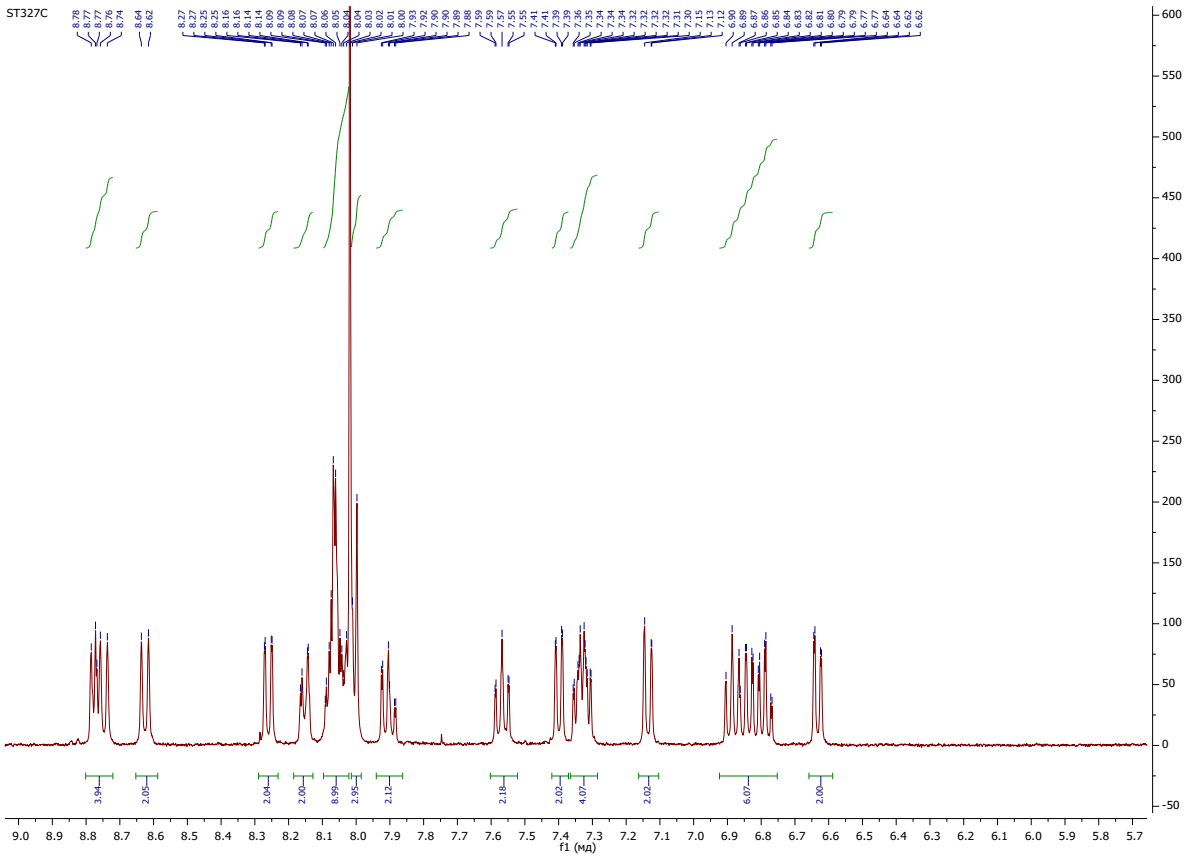

Figure S22. ^{1}H NMR of [Ir(phi)$_2$(bpy)] (400MHz, acetone-d_6)

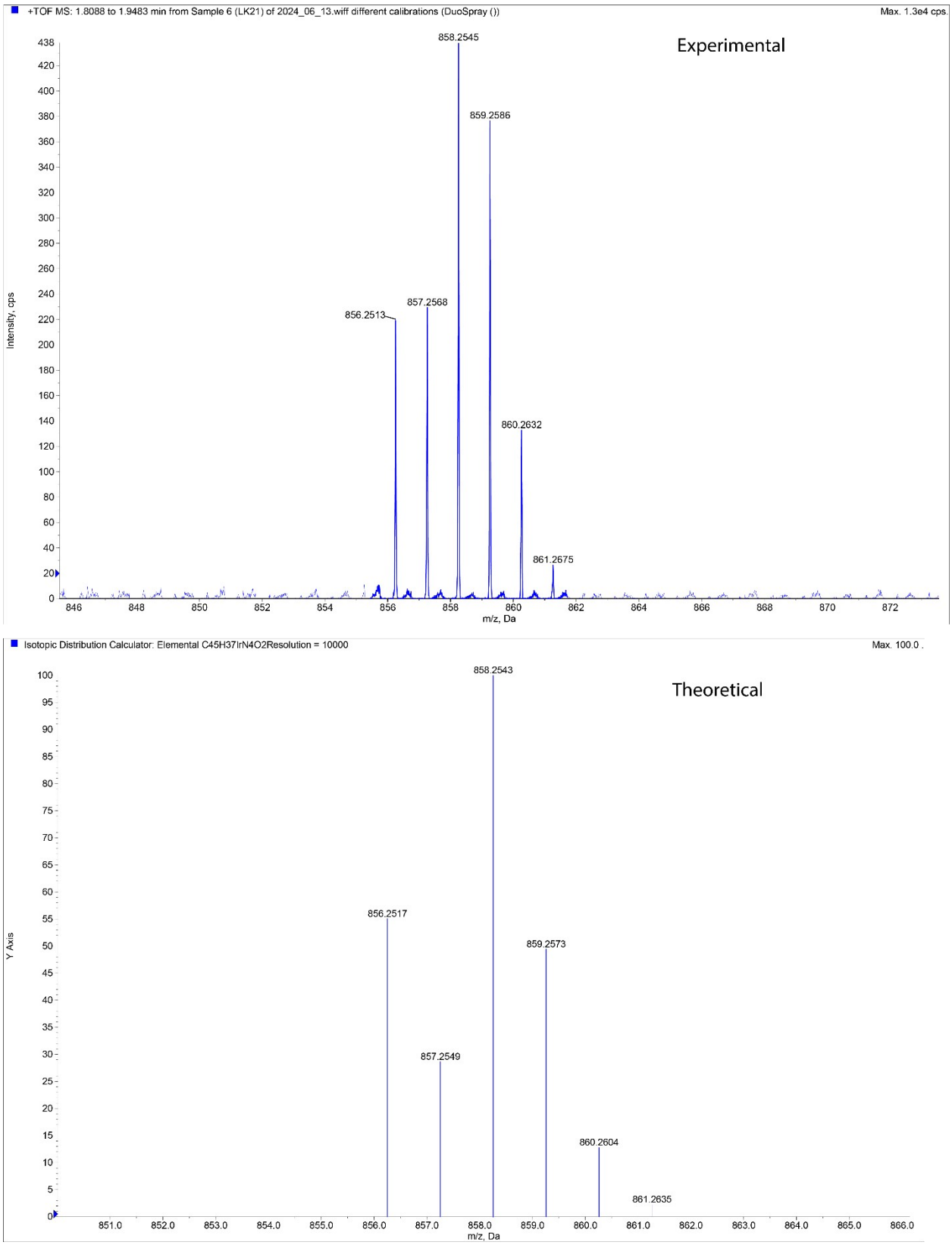

Figure S23. High resolution mass spectrum of [Ir(bim)$_2$(acac)]

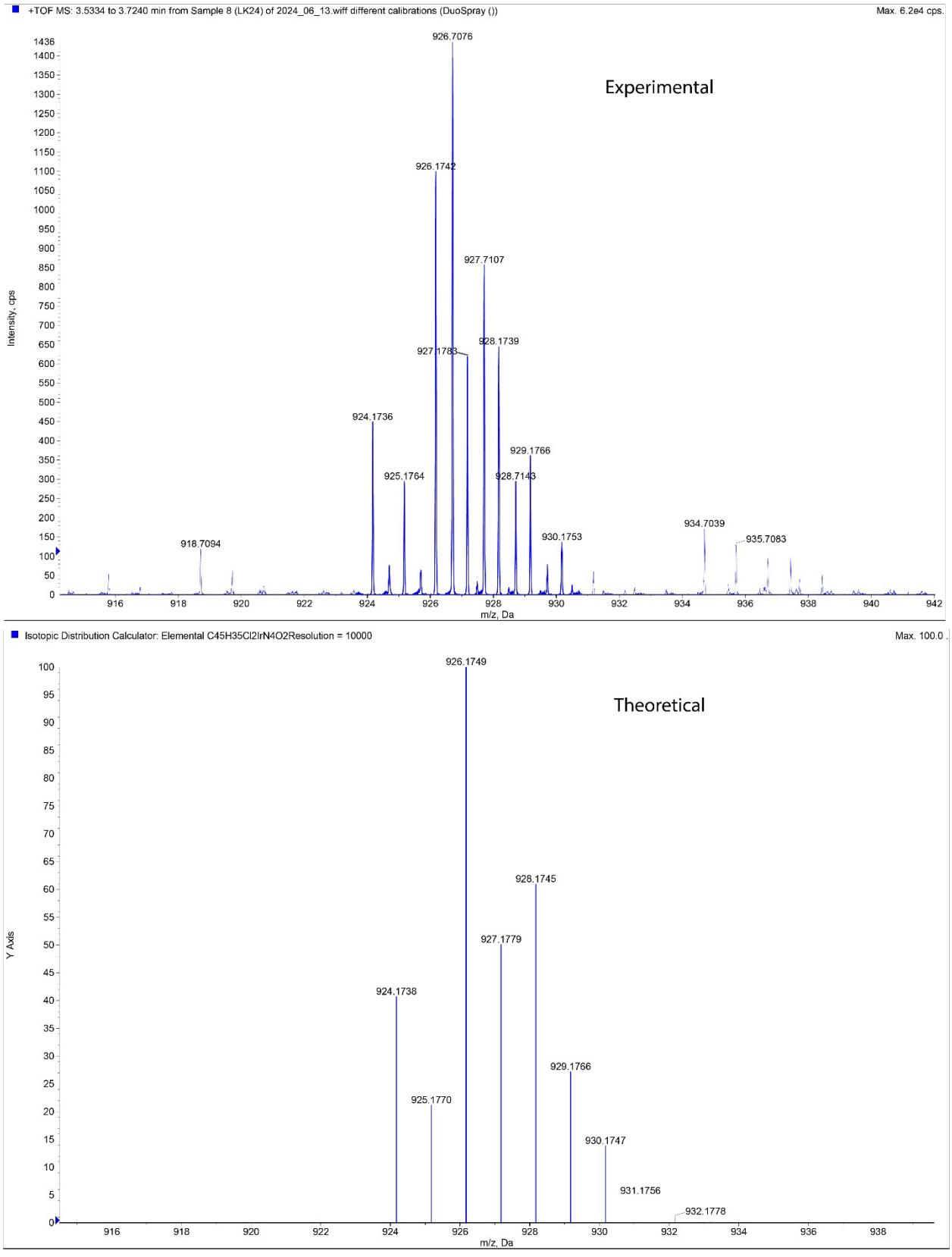

Figure S24. High resolution mass spectrum of [Ir(cbim)$_2$(acac)].

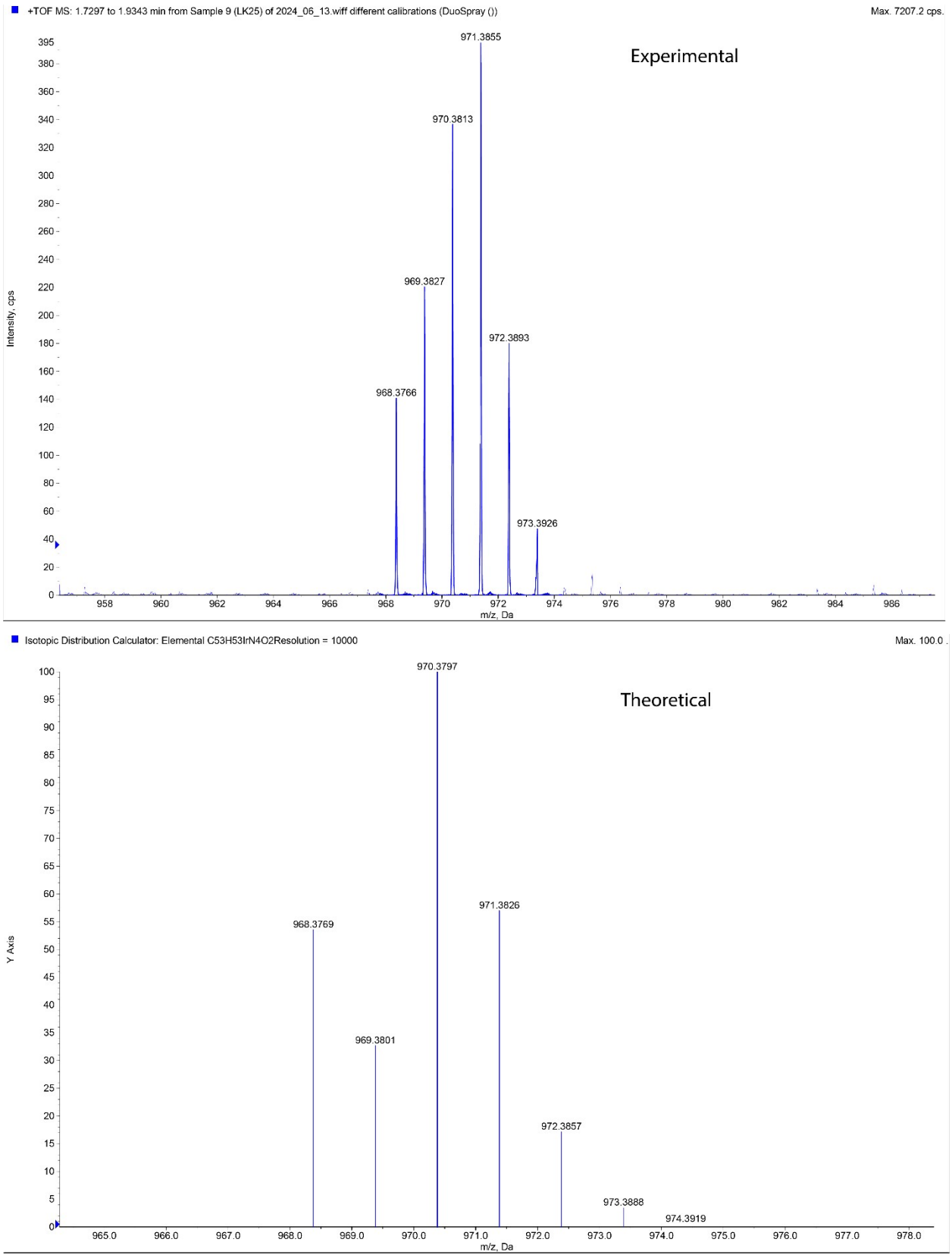

Figure S25. High resolution mass spectrum of [Ir(tbim)$_2$(acac)].

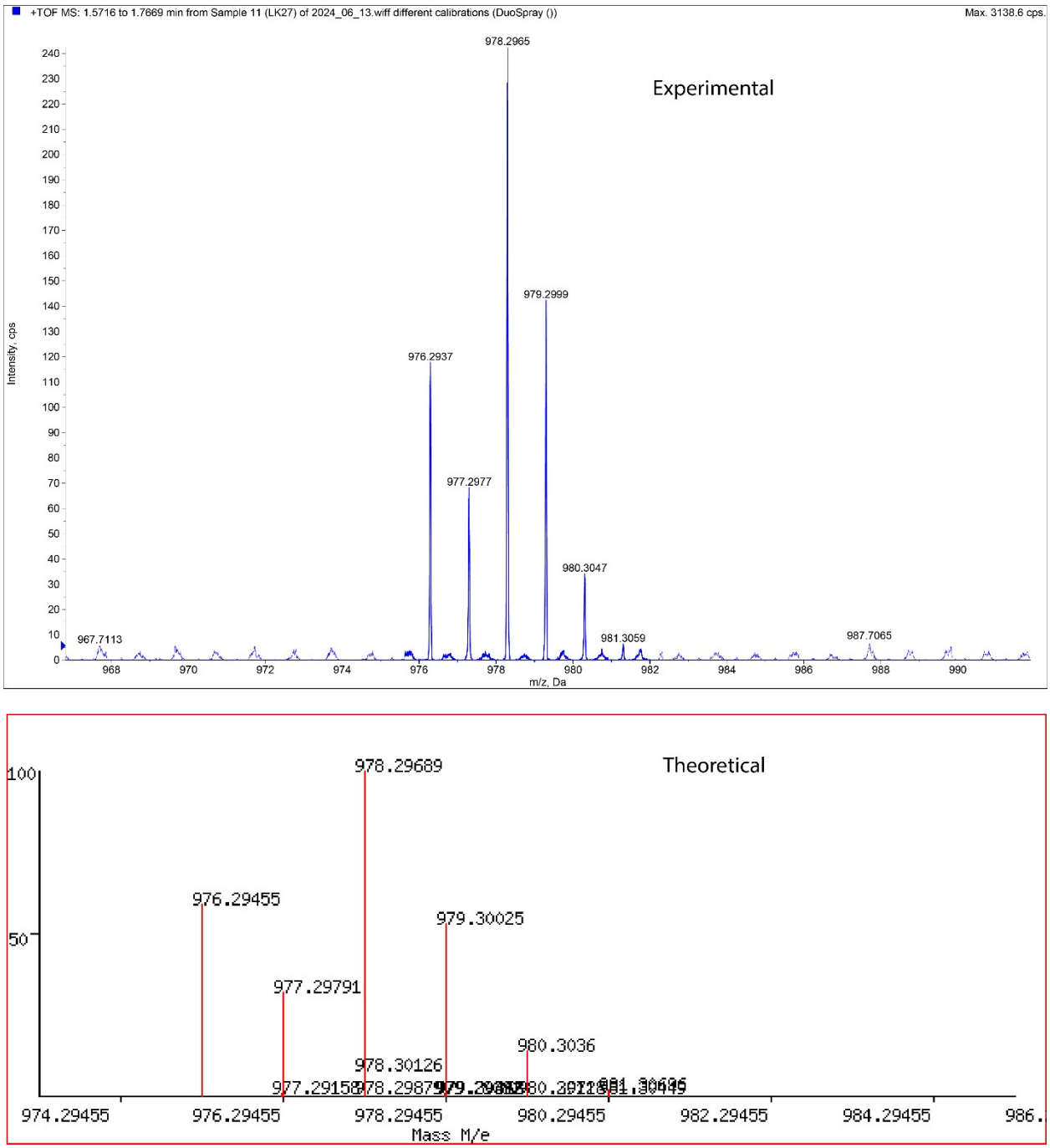

Figure S26. High resolution mass spectrum of [Ir(mbim)$_2$(acac)].

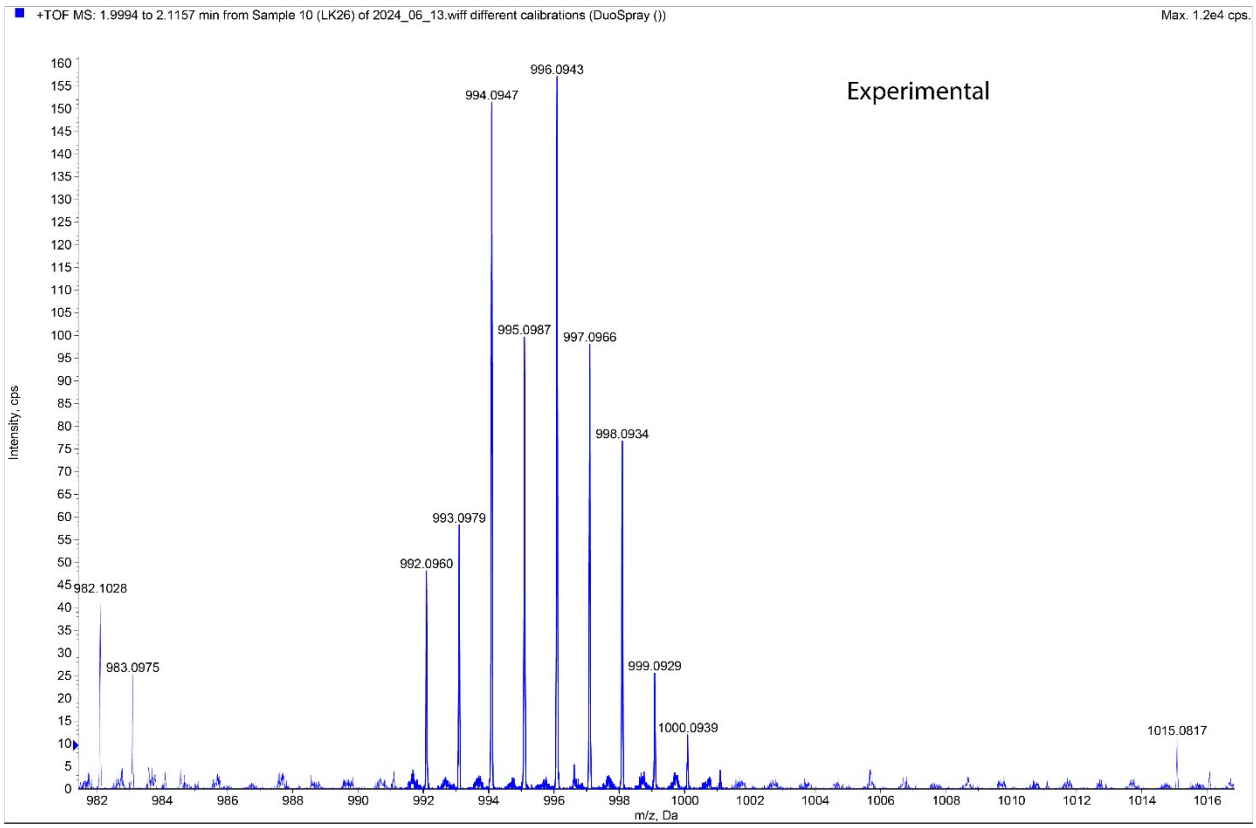

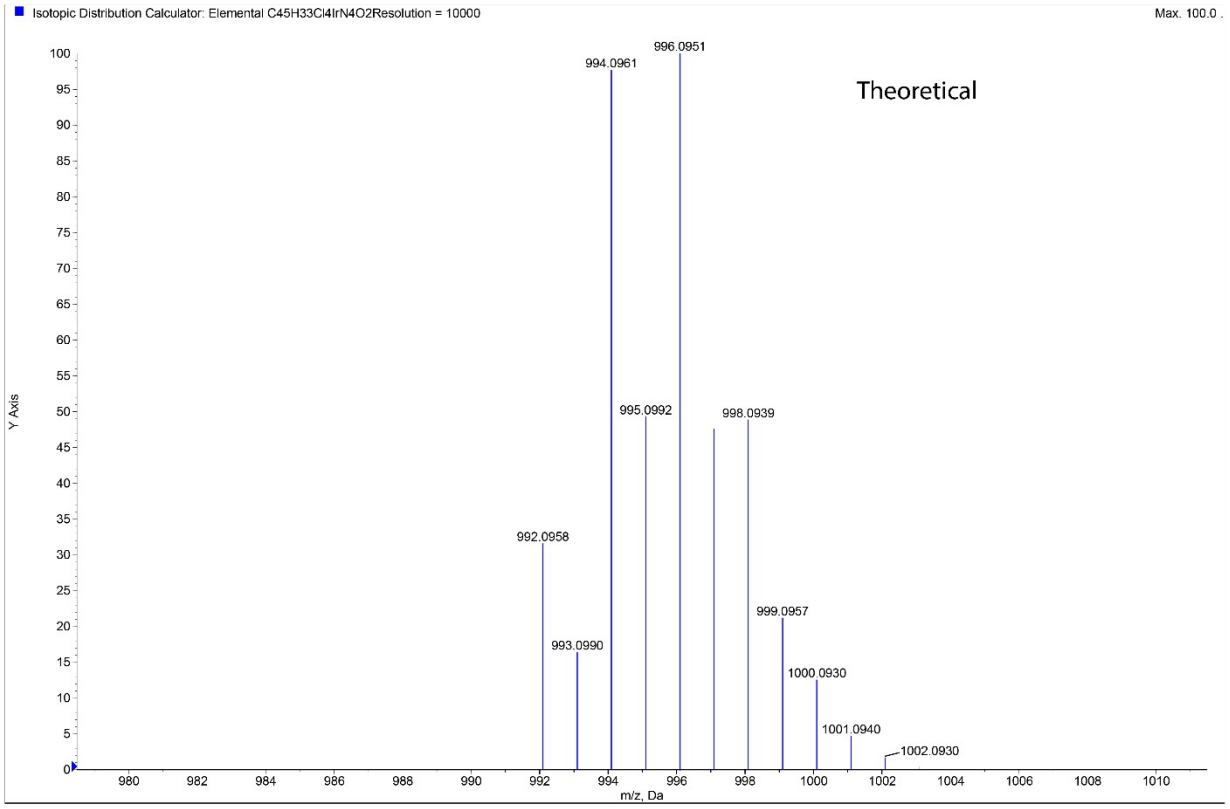

Figure S27. High resolution mass spectrum of [Ir(dcbim)$_2$(acac)].

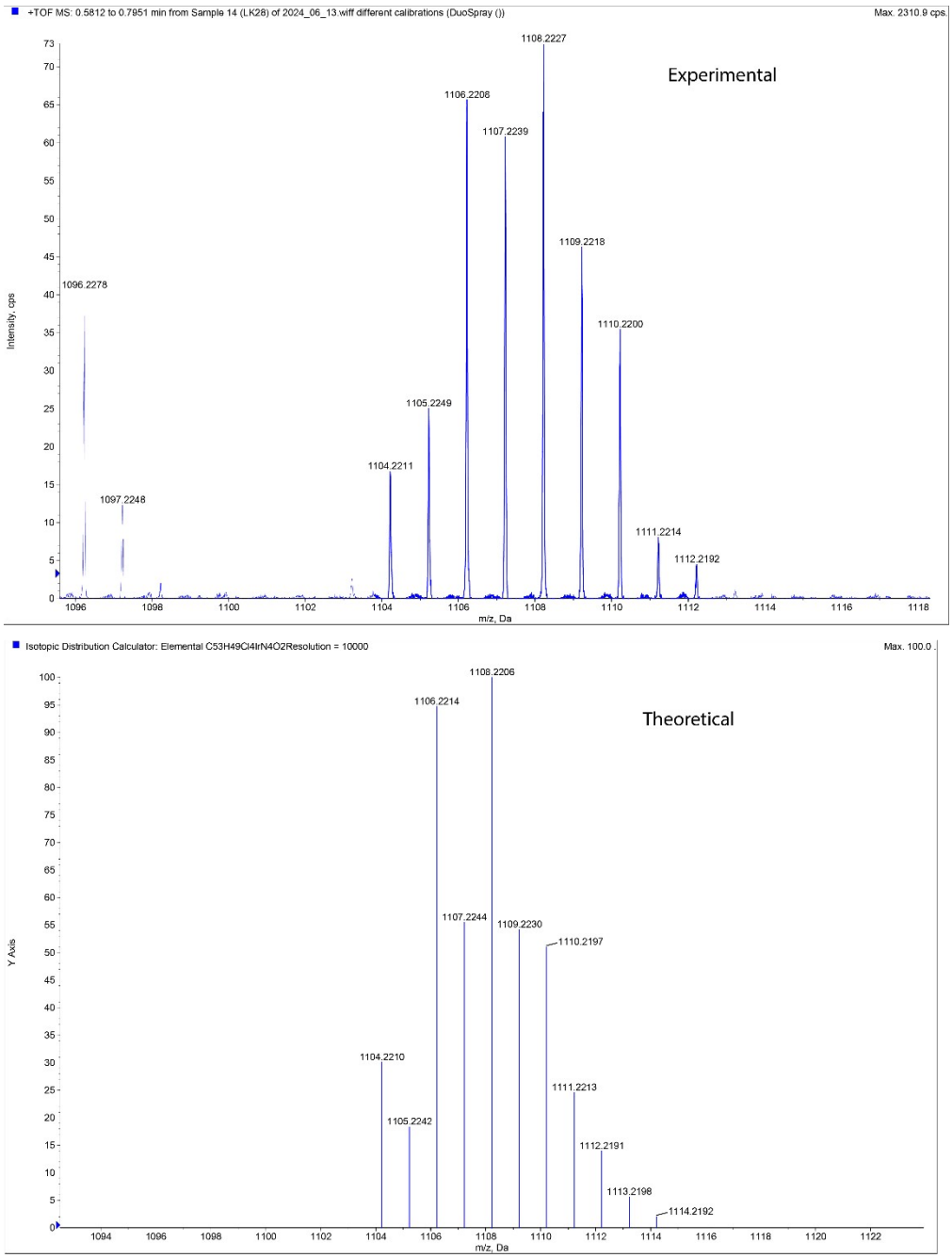

Figure S28. High resolution mass spectrum of [Ir(tdcbim)$_2$(acac)].

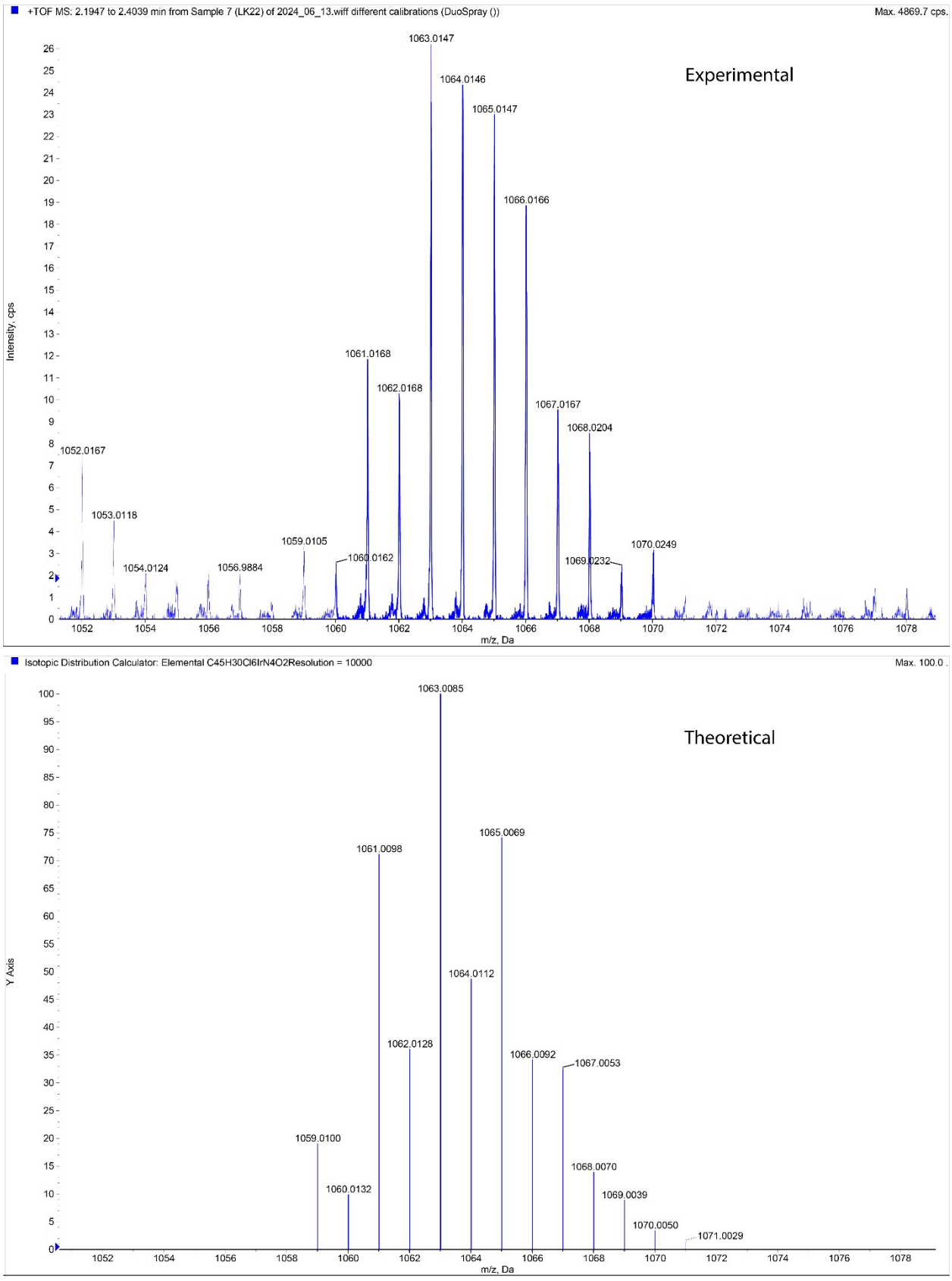

Figure S29. High resolution mass spectrum of [Ir(tcbim)$_2$(acac)].

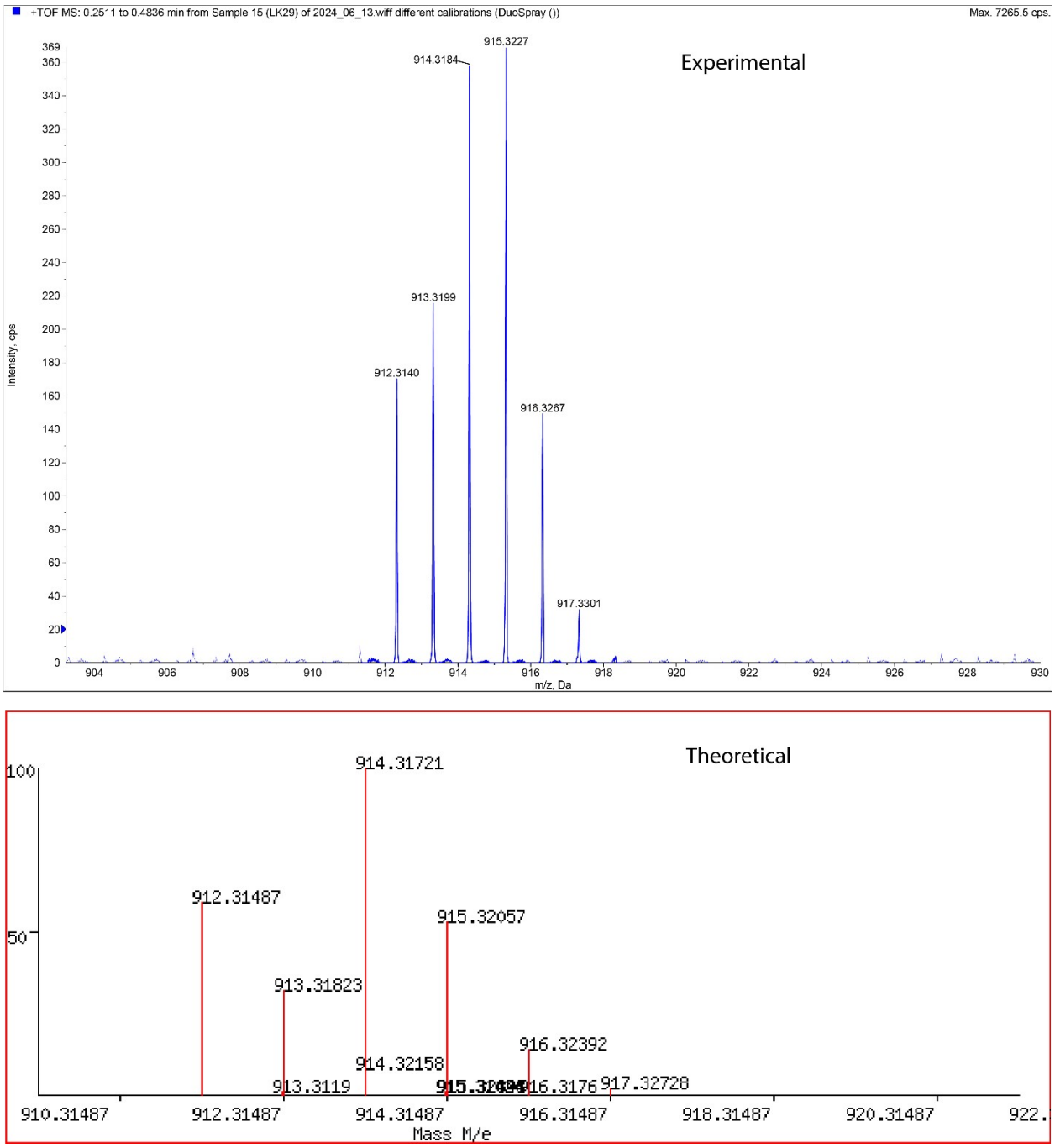

Figure S30. High resolution mass spectrum of [Ir(dmbim)$_2$(acac)].

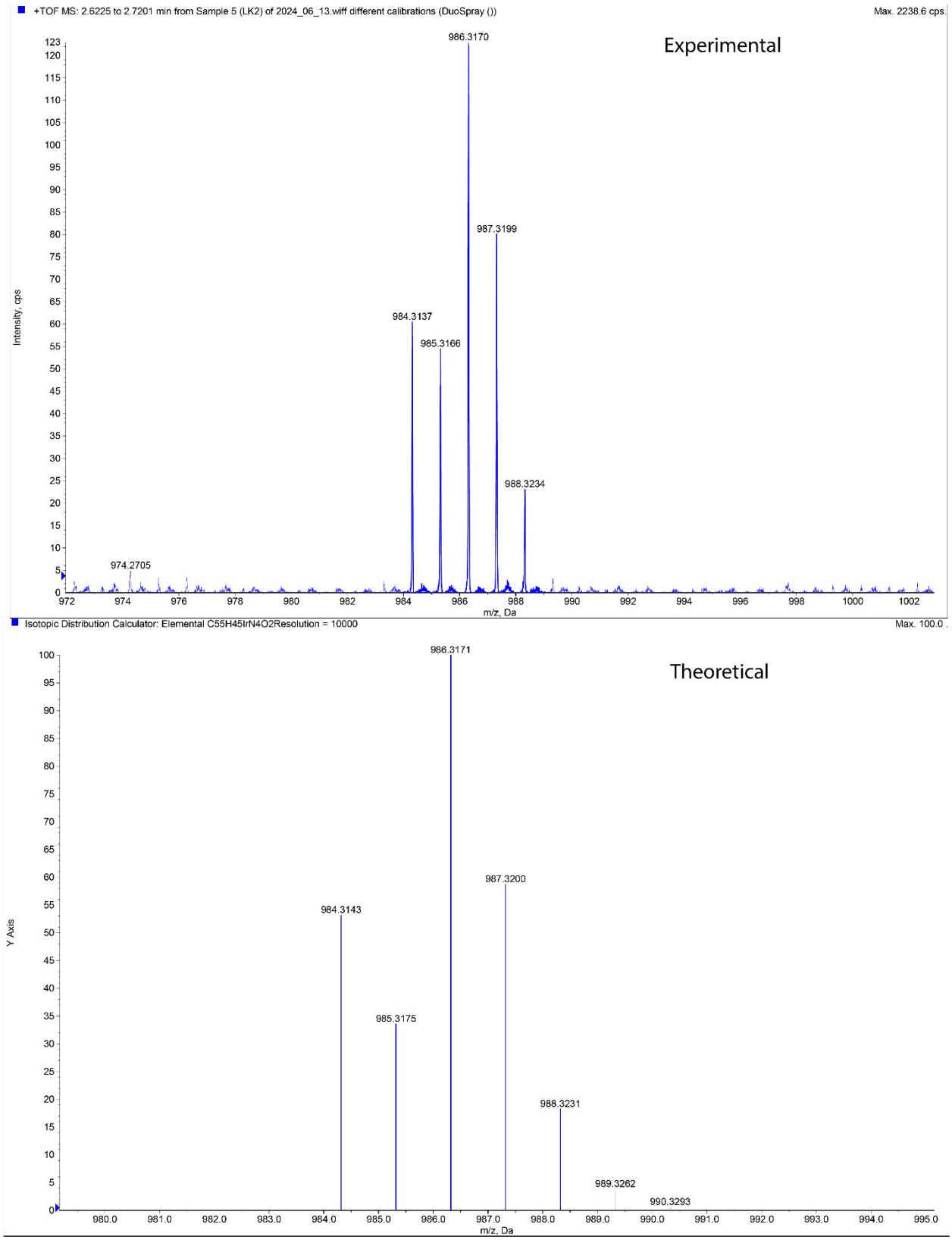

Figure S31. High resolution mass spectrum of [Ir(mnim)$_2$(acac)].

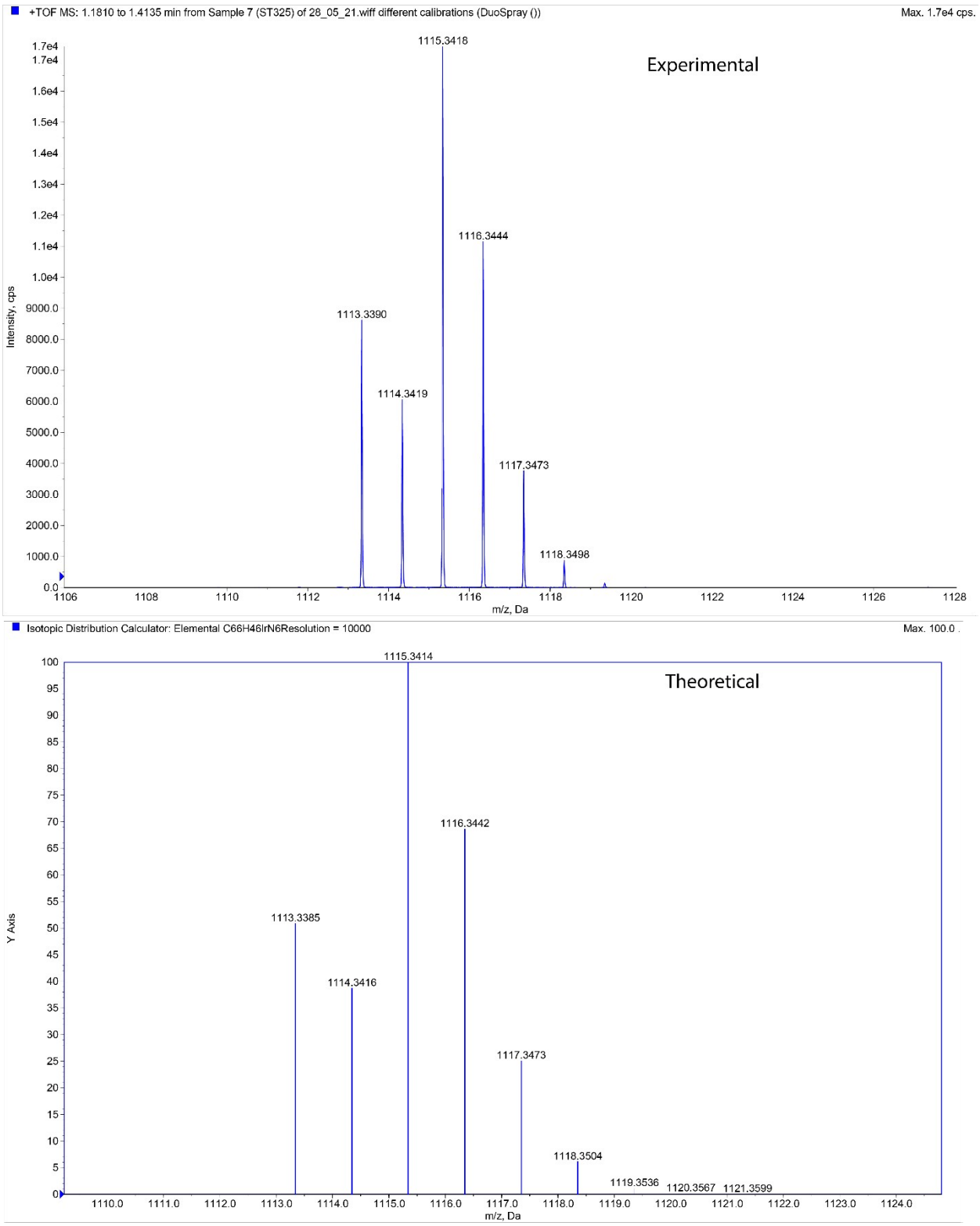

Figure S32. High resolution mass spectrum of [Ir(phi)$_2$(dmbpy)].

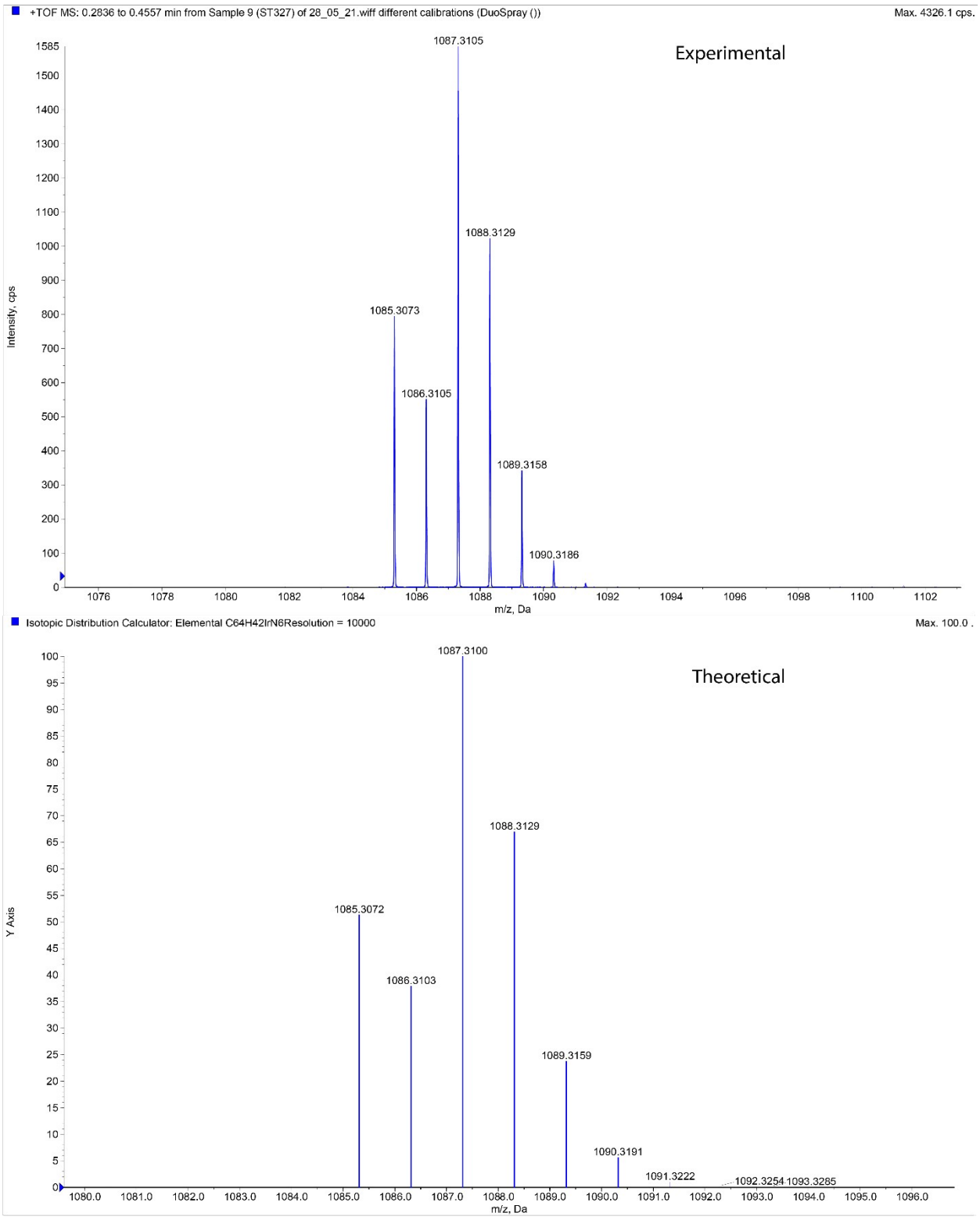

Figure S33. High resolution mass spectrum of [Ir(phi)$_2$(bpy)].

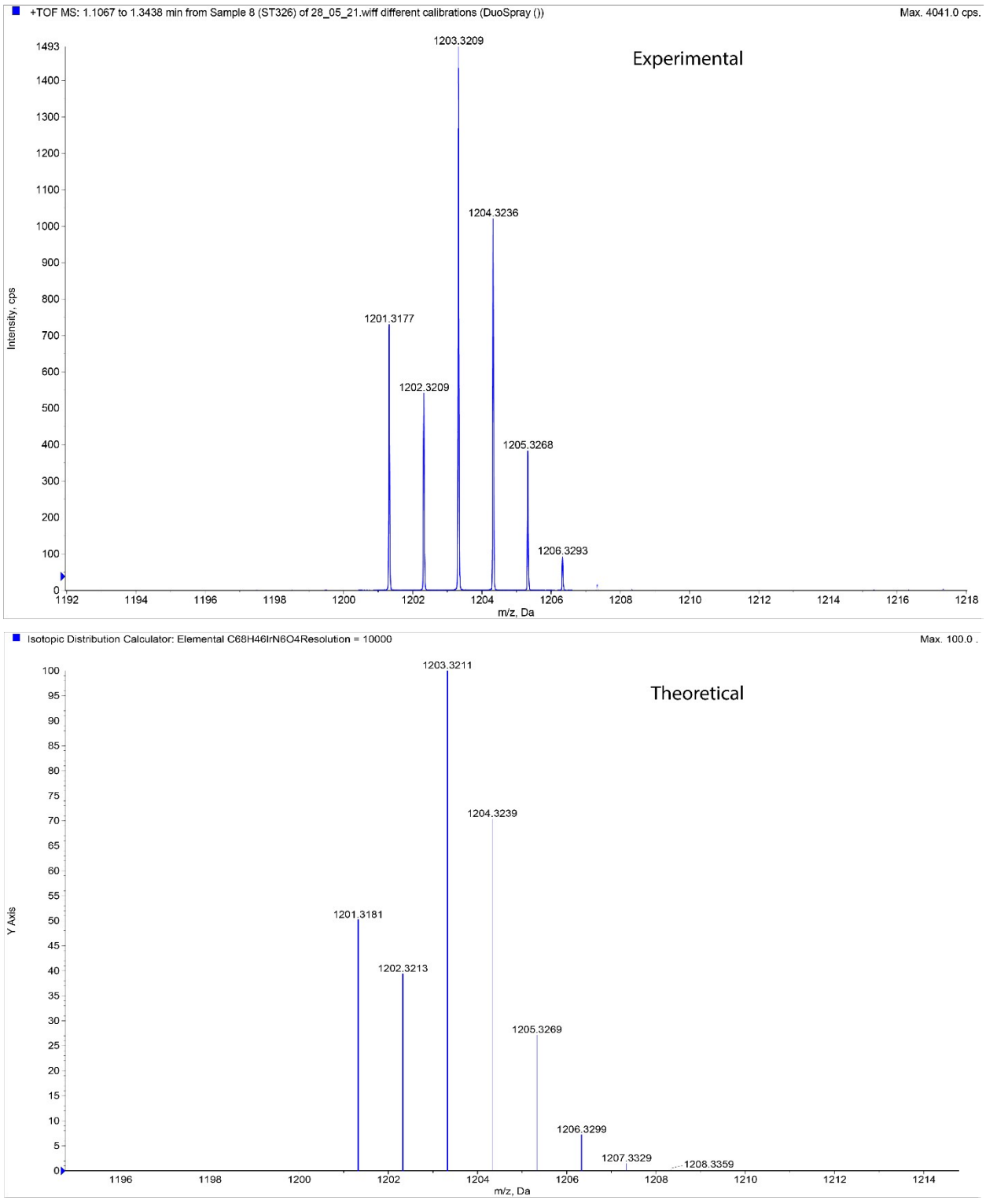

Figure S34. High resolution mass spectrum of [Ir(phi)$_2$(dcmbpy)].

3. X-ray data

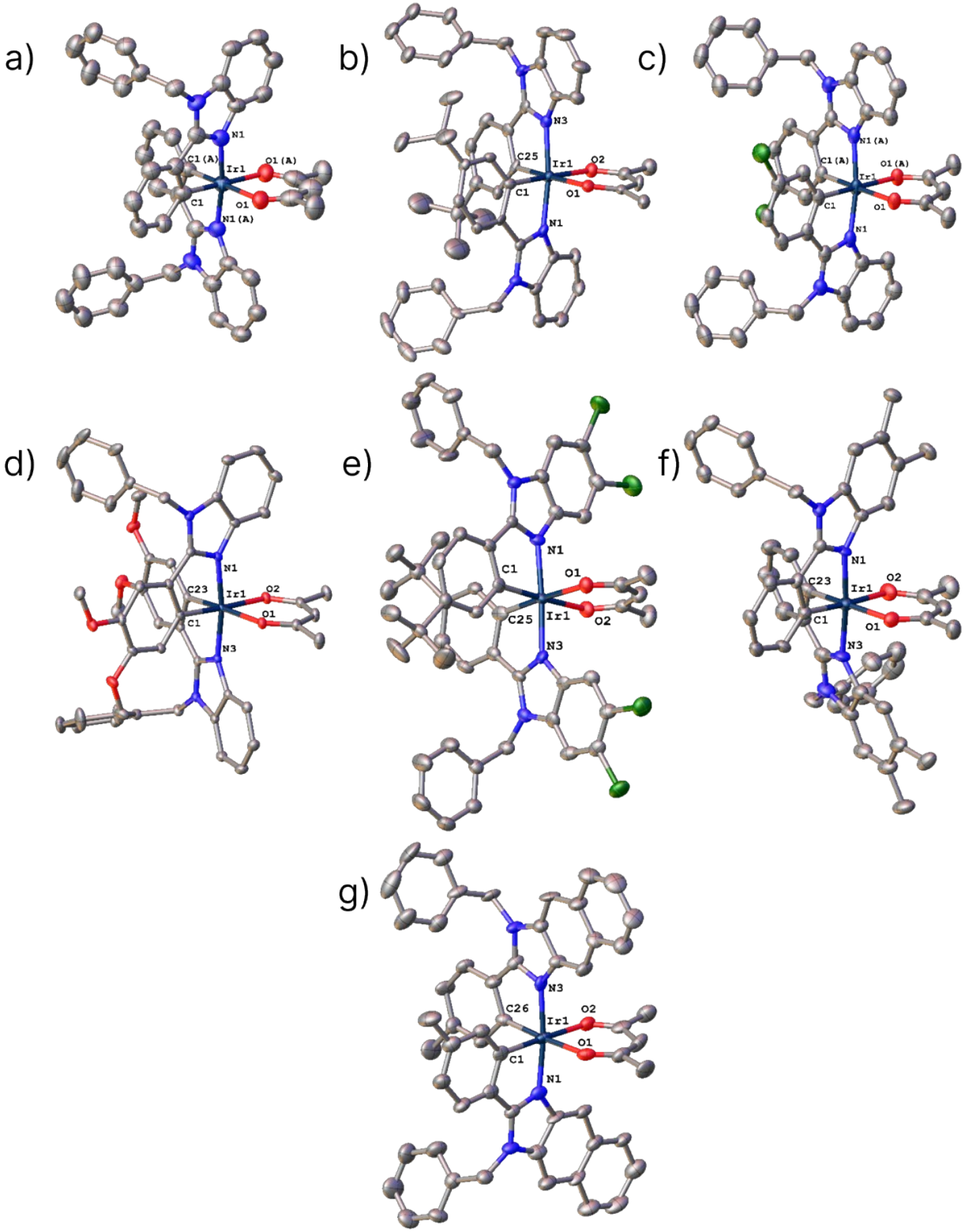

Figure S35. Molecular structures of acac Ir(III) complexes: a) [Ir(bim)$_2$(acac)], b) [Ir(tbim)$_2$(acac)], c) [Ir(cbim)$_2$(acac)], d) [Ir(mbim)$_2$(acac)], e) [Ir(tdcbim)$_2$(acac)], f) [Ir(dmbim)$_2$(acac)], and g) [Ir(mnim)$_2$(acac)] (lower row). Displacement ellipsoids are shown at 50% probability level. Disordered fragments and hydrogen atoms are omitted for clarity. In the structures of [Ir(bim)$_2$(acac)] and [Ir(cbim)$_2$(acac)] atoms C(A), N(A) and O(A) are devoted to a symmetrically equivalent part of the molecule because of the 2 axis symmetry element.

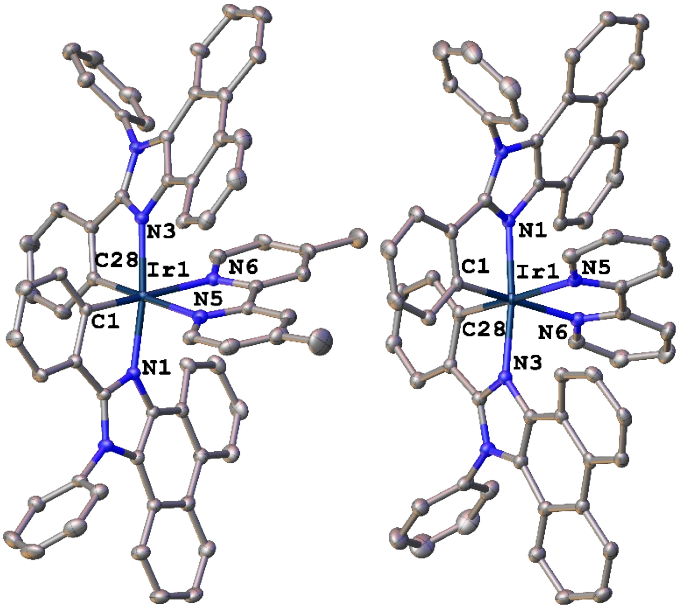

Figure S36. Molecular structures of complexes [Ir(phi)$_2$(dmbpy)] and [Ir(phi)$_2$(bpy)]. Displacement ellipsoids are shown at 50% probability level. Disordered fragments, counterion $CF_3SO_3^-$ and hydrogen atoms are omitted for clarity.

Table S1. Details of the X-ray crystal data collection and structure refinement for acac complexes.

	[Ir(bim)$_2$acac]	[Ir(mnim)$_2$acac]	[Ir(cbim)$_2$acac]	[Ir(tbim)$_2$acac]	[Ir(mbim)$_2$acac]	[Ir(tdcbim)$_2$acac]	[Ir(dmbim)$_2$acac]
Radiation	CuKα (λ = 1.54178)	MoKα (λ = 0.71073)	CuKα (λ = 1.54178)	MoKα (λ = 0.71073)	MoKα (λ = 0.71073)	MoKα (λ = 0.71073)	CuKα (λ = 1.54178)
Empirical formula	$C_{45}H_{37}IrN_4O_2{\cdot}CH_2Cl_2$	$C_{55}H_{45}IrN_4O_2{\cdot}2CH_2Cl_2$	$C_{45}H_{35}IrN_4O_2$	$C_{53}H_{53}IrN_4O_2{\cdot}1.9CH_2Cl_2$	$C_{49}H_{45}IrN_4O_6{\cdot}3CH_3CN$	$C_{53}H_{49}Cl_4IrN_4O_2{\cdot}2CHCl_3$	$C_{49}H_{45}IrN_4O_2{\cdot}0.5C_2H_5OH$
M_w	942.91	1156	926.87	1131.55	1101.25	1346.69	936.62
Cryst. system	monoclinic	triclinic	monoclinic	triclinic	triclinic	triclinic	triclinic
Space group	P2/c	P-1	P2/n	P-1	P-1	P-1	P-1
a, Å	12.9767(7)	12.760(2)	12.5977(3)	13.3198(19)	12.4916(4)	13.6550(7)	9.7982(8)
b, Å	10.1078(5)	14.925(2)	10.4319(2)	13.6801(18)	12.6126(4)	15.3418(8)	13.9488(11)
c, Å	15.6040(7)	15.052(3)	15.5631(4)	15.721(2)	16.5493(5)	16.3956(9)	15.6778(13)
V, Å^3	1999.23(17)	2433.2(7)	1878.99(8)	2559.3(6)	2442.95(13)	2808.4(3)	2134.2(3)
α/°	90	66.747(4)	90	91.040(5)	69.7300(10)	64.479(2)	93.774(6)
β/°	102.366(4)	67.495(4)	113.2630(10)	96.672(5)	89.6670(10)	88.608(2)	92.282(5)
γ/°	90	81.271(4)	90	115.560(5)	87.2640(10)	66.938(2)	92.442(6)
Z	2	2	4	2	2	2	2
ρ_{cald} (g·cm^{-3})	1.566	1.578	1.638	1.468	1.497	1.593	1.457
Abs coeff (mm^{-1})	8.037	3.012	8.542	2.851	2.792	2.898	6.408
F(000)	940	1160	920	1144	1116	1344	945
2θ range (deg)	6.974 to 136.886	4.55 to 50.1	7.70 to 137.96	3.31 to 50.1	4.16 to 64.00	3.246 to 50.1	5.654 to 150.388
Total/independent reflections	18386/3661	22410/8494	16789/3471	21178/8911	44348/16480	33867/9929	27083/8573
Completeness to θ (%)	99.3	98.6	99.1	98.4	97.2	99.8	97.1
no. of data/restraints/params	3661/7/264	8494/10/617	3471/0/246	8911/34/600	16480/0/631	9929/9/672	8573/5/550
Goodness of fit on F^2	1.037	0.959	1.046	1.074	1.045	1.046	1.008
R_1 ($I > 2\sigma(I)$)	0.0553	0.0613	0.0349	0.0653	0.0247	0.0563	0.0569
wR_2(all data)	0.1446	0.1497	0.0884	0.1104	0.0511	0.1217	0.1471
T, K	100	150	100	100	100	100	100
Largest diff peak/hole (e/Å^3)	1.24/-2.41	2.65/-1.85	1.90/-0.53	1.78/-1.58	0.93/-1.20	2.34/-1.71	1.99/-1.83

Table S2. Details of the X-ray crystal data collection and structure refinement for complexes $[Ir(phi)_2(dmbpy)]$ and $[Ir(phi)_2(bpy)]$.

	$[Ir(phi)_2dmbpy]$	$[Ir(phi)_2bpy]$
Radiation	MoKα (λ = 0.71073)	MoKα (λ = 0.71073)
Empirical formula	$[C_{66}H_{46}IrN_6]^+\cdot[CF_3SO_3]^-\cdot CH_2Cl_2$	$[C_{64}H_{40}IrN_6]^+\cdot[CF_3SO_3]^-\cdot 4C_2H_5OH\cdot$[+solvent]
M_w	1349.28	1443.61
Cryst. system	monoclinic	triclinic
Space group	$P2_1/n$	P-1
a, Å	12.4597(3)	12.8765(4)
b, Å	27.2824(7)	16.2996(5)
c, Å	16.6337(5)	17.5981(5)
V, Å^3	5652.5(3)	3189.69(17)
α/°	90	67.5950(10)
β/°	91.4360(10)	83.5250(10)
γ/°	90	69.1370(10)
Z	4	2
ρ_{cald} (g·cm^{-3})	1.586	1.503
Abs coeff (mm^{-1})	2.560	2.197
F(000)	2704	1470
2θ range (deg)	4.036 to 66.372	3.812 to 61.086
Total/independent reflections	78855/20858	60180/17880
Completeness to θ (%)	96.4	91.4
no. of data/restraints/params	20859/15/752	17880/9/832
Goodness of fit on F^2	1.028	1.051
R_1 ($I > 2\sigma(I)$)	0.0354	0.0347
wR_2(all data)	0.0785	0.0825
T, K	150	100
Largest diff peak/hole (e/Å^3)	1.08/-1.26	2.34/-1.39

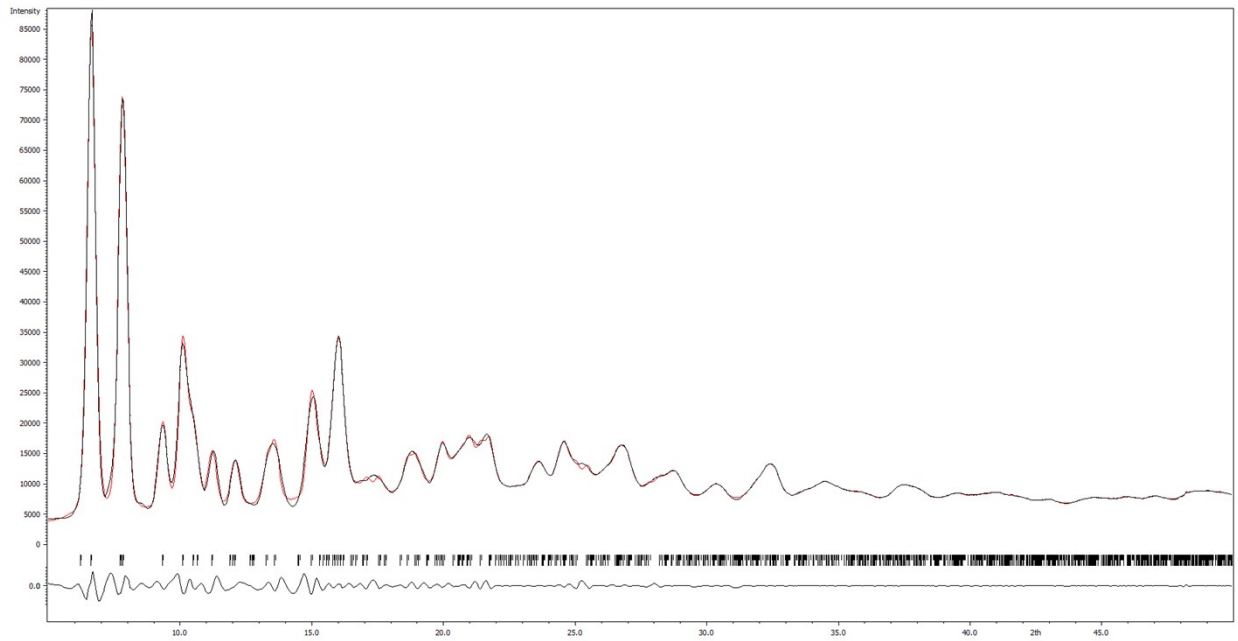

Figure S37. Powder XRD pattern of complex [Ir(mnim)$_2$acac] (black line) with the simulated pattern (red line). The differential is presented in the bottom.

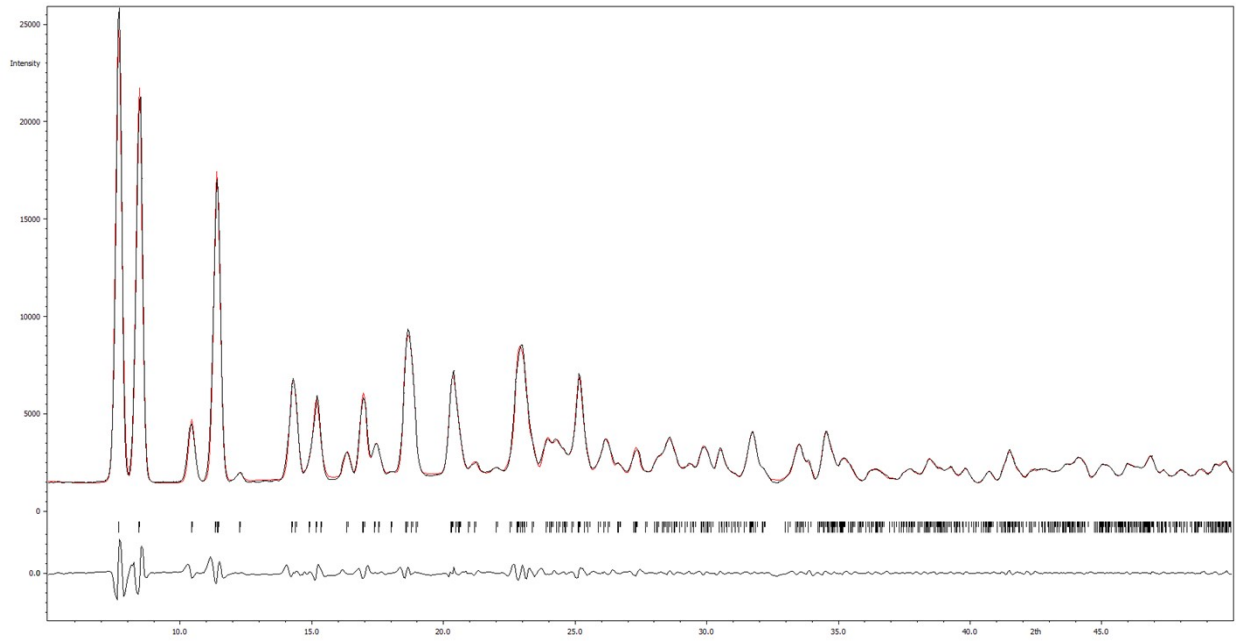

Figure S38. Powder XRD pattern of complex [Ir(cbim)$_2$acac] (black line) with the simulated pattern (red line). The differential is presented in the bottom.

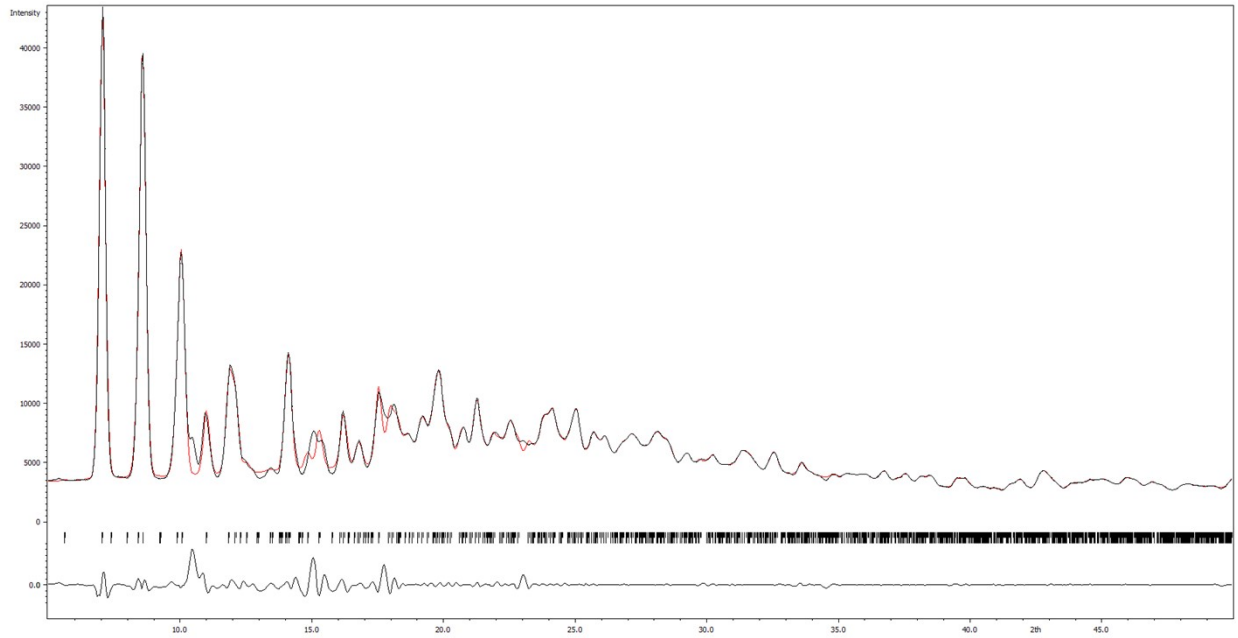

Figure S39. Powder XRD pattern of complex [Ir(tbim)$_2$acac] (black line) with the simulated pattern (red line). The differential is presented in the bottom.

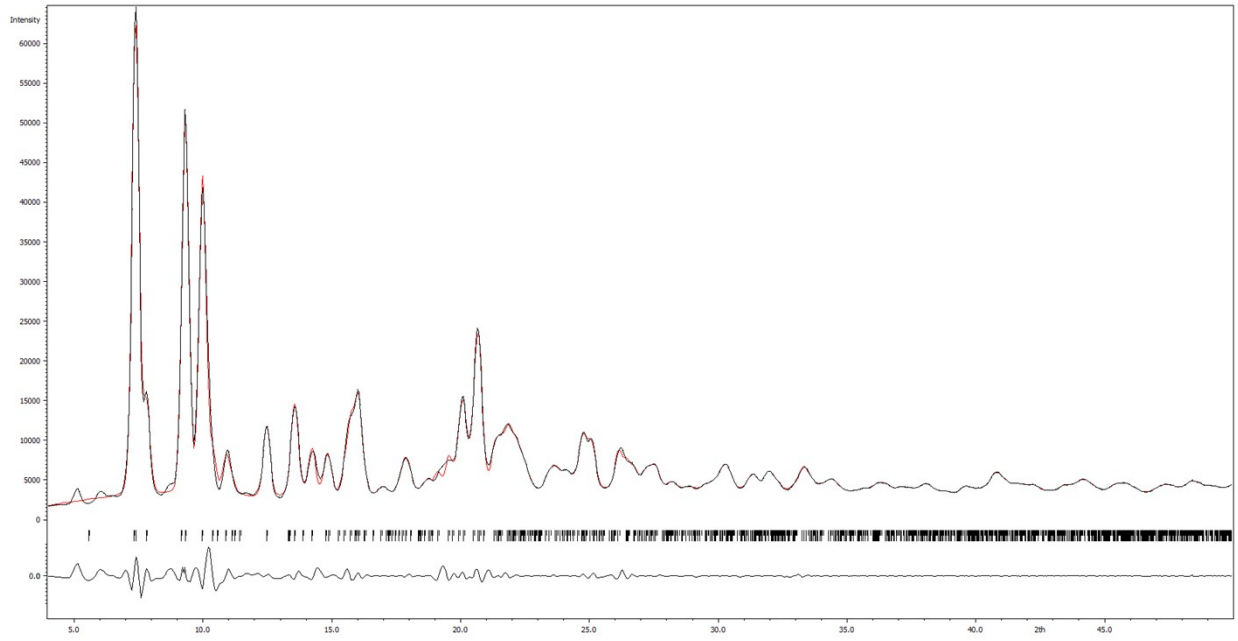

Figure S40. Powder XRD pattern of complex [Ir(mbim)$_2$acac] (black line) with the simulated pattern (red line). The differential is presented in the bottom.

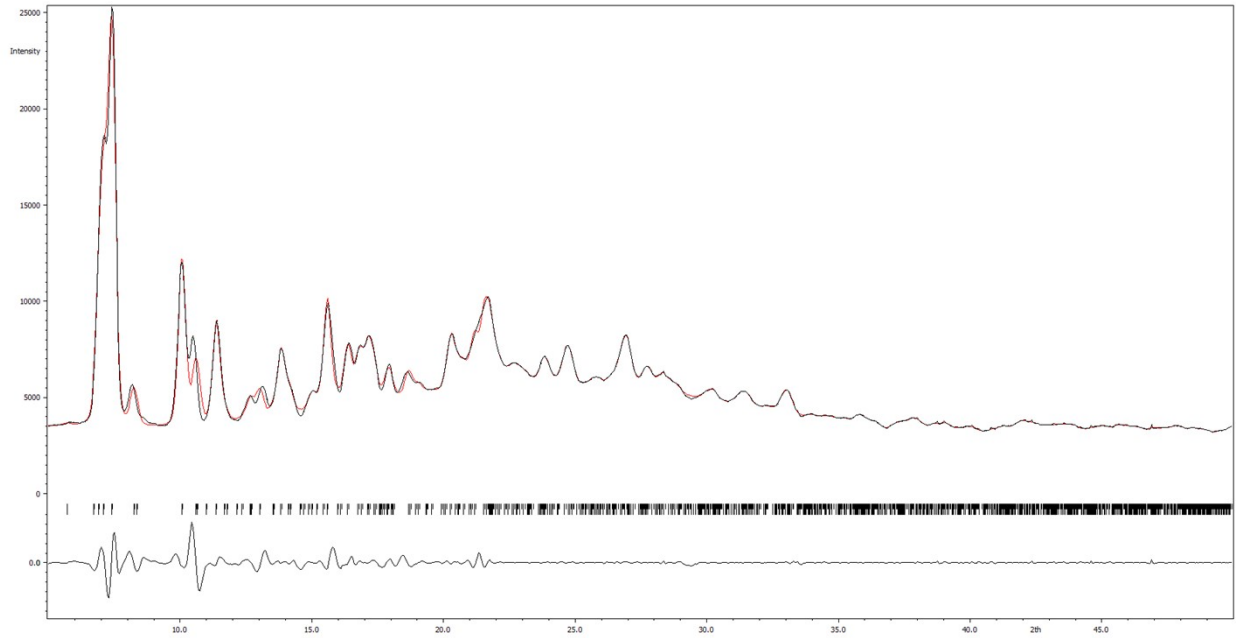

Figure S41. Powder XRD pattern of complex [Ir(tdcbim)$_2$acac] (black line) with the simulated pattern (red line). The differential is presented in the bottom

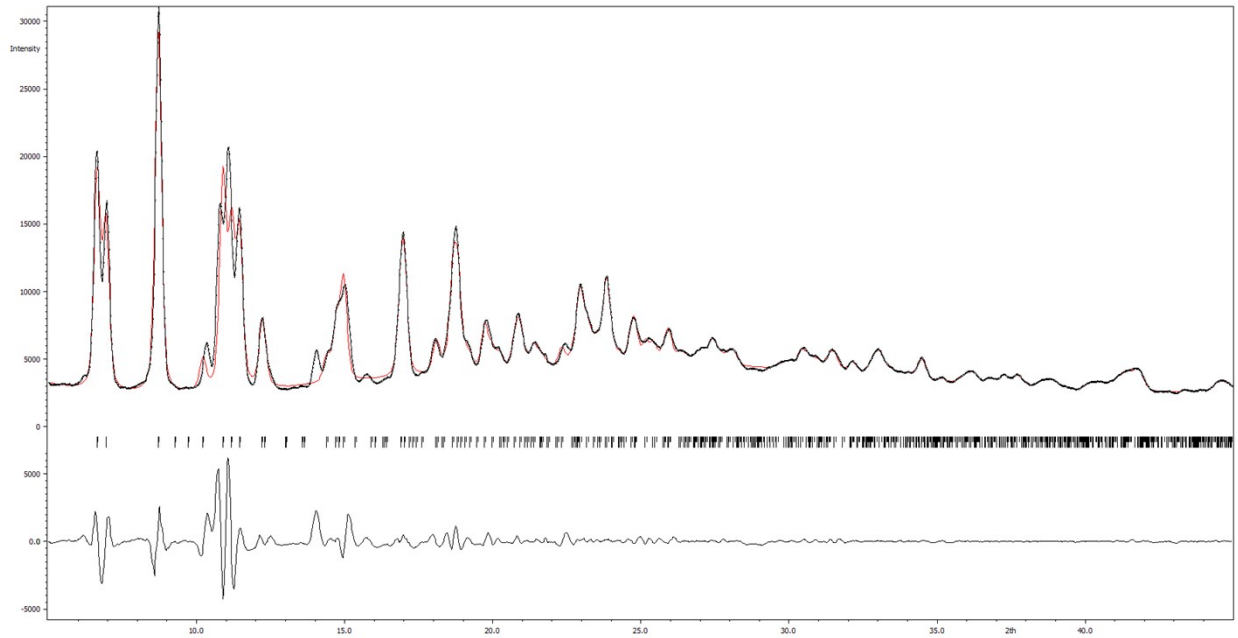

Figure S42. Powder XRD pattern of complex [Ir(dmbim)$_2$acac] (black line) with the simulated pattern (red line). The differential is presented in the bottom

4. Redox and optical properties.

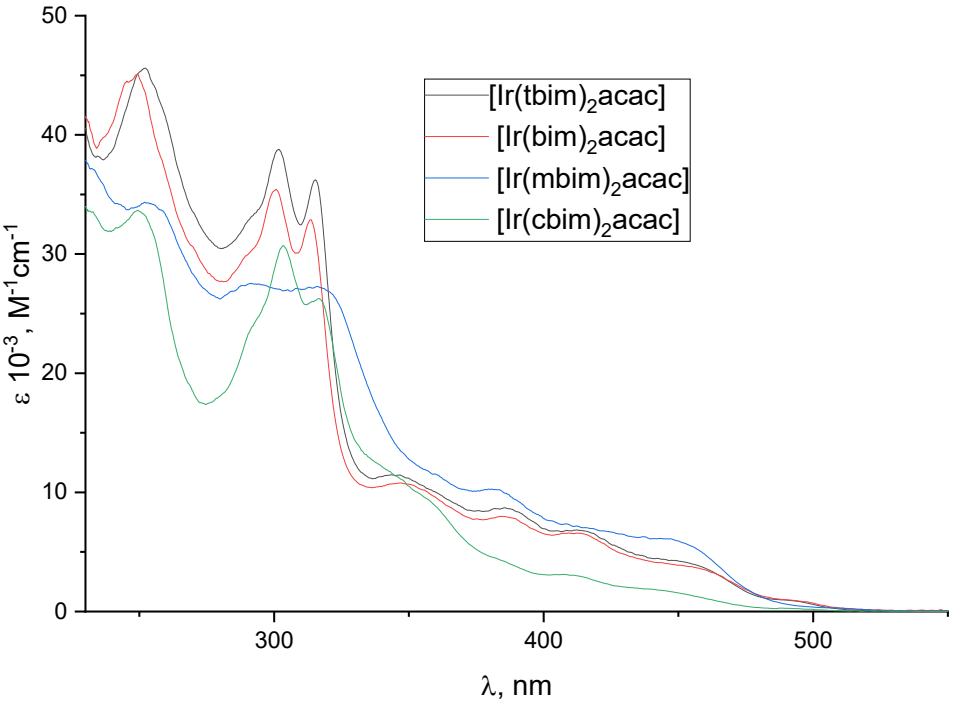

Figure S43. Absorption spectra of [Ir(mbim)$_2$acac], [Ir(tbim)$_2$acac], [Ir(bim)$_2$acac], [Ir(cbim)$_2$acac] measured in CH_2Cl_2 (25°C, air).

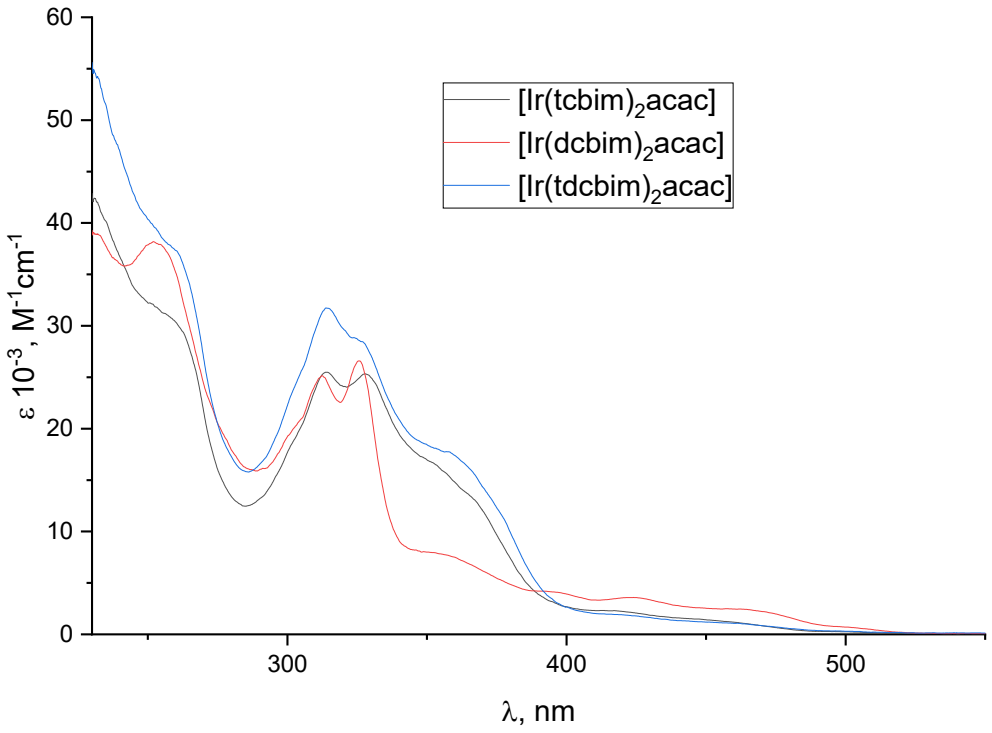

Figure S44. Absorption spectra of [Ir(tdcbim)$_2$acac], [Ir(dcbim)$_2$acac], [Ir(tcbim)$_2$acac] measured in CH_2Cl_2 (25°C, air).

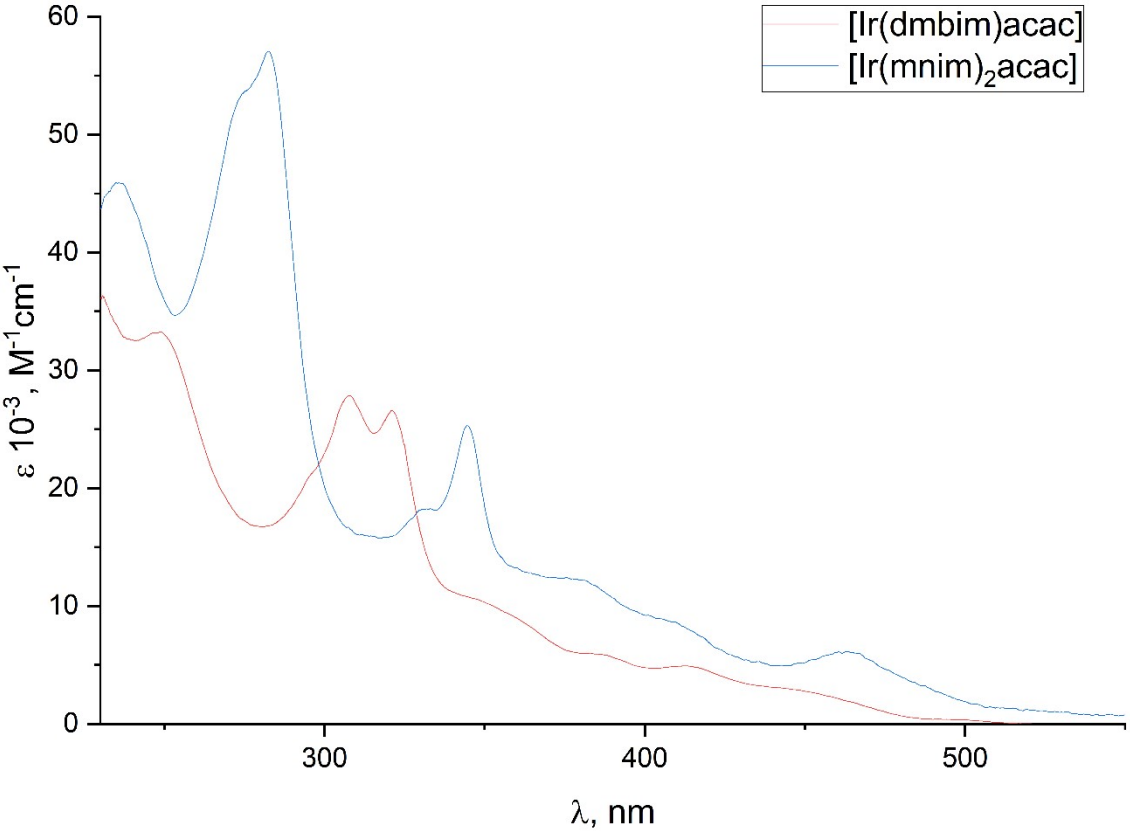

Figure S45. Absorption spectra of [Ir(dmbim)$_2$acac], [Ir(mnim)$_2$acac] measured in CH_2Cl_2 (25°C, air).

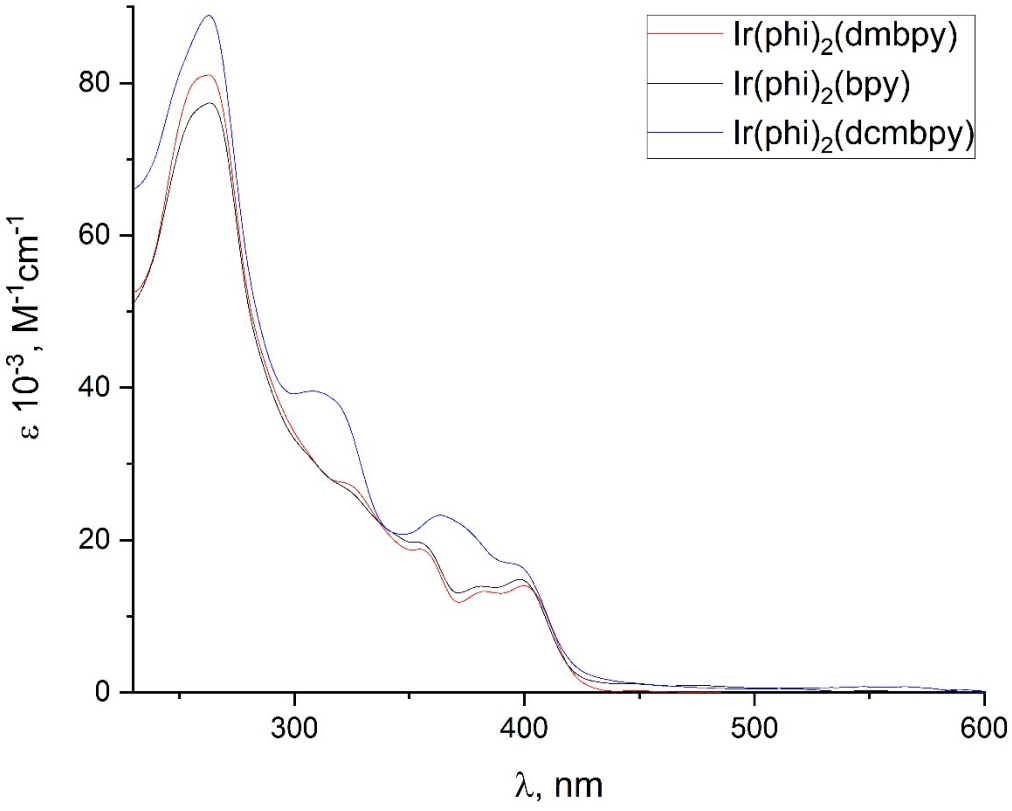

Figure S46. Absorption spectra of [Ir(phi)$_2$(dmbpy)], [Ir(phi)$_2$(bpy)], [Ir(phi)$_2$(dcmbpy)] measured in CH_2Cl_2 (25°C, air)..

Table S3. Values of the λ_{max} of the luminescence for the newly synthesized complexes.

Complex	Luminescence λ_{max}
[Ir(mnim)$_2$acac]	571, 618(sh)
[Ir(bim)$_2$acac]	513
[Ir(tcbim)$_2$acac]	517
[Ir(cbim)$_2$acac]	509, 543(sh)
[Ir(tbim)$_2$acac]	511
[Ir(dcbim)$_2$acac]	523
[Ir(mbim)$_2$acac]	528
[Ir(tdcbim)$_2$acac]	522
[Ir(dmbim)$_2$acac]	515, 548(sh)
[Ir(phi)$_2$(dmbpy)]	588*
[Ir(phi)$_2$(bpy)]	610*
[Ir(phi)$_2$(dcmbpy)]	644*

*These compounds have complex emission spectra with several luminescence maxima of similar relative intensities.

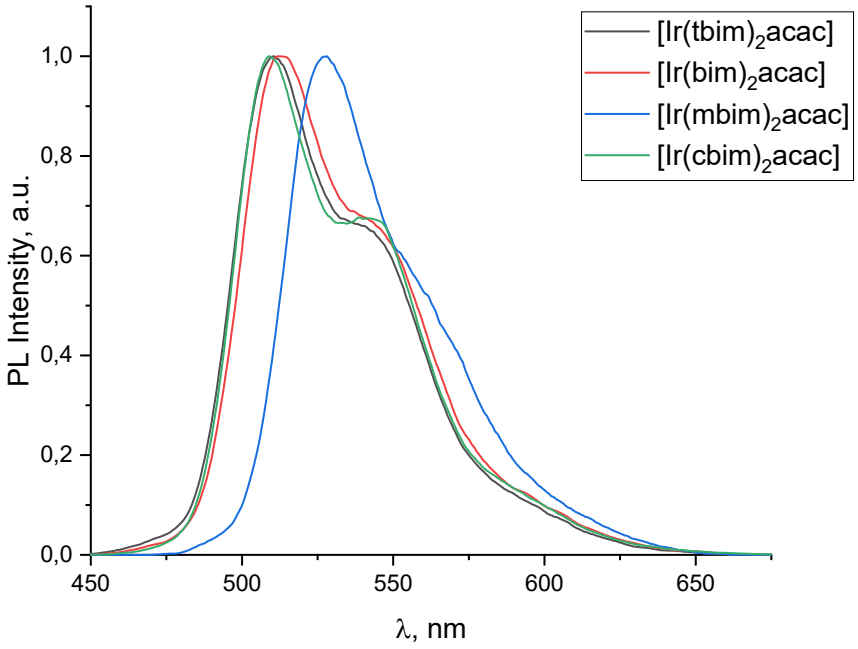

Figure S47. Normalized luminescence spectra of [Ir(mbim)$_2$acac], [Ir(tbim)$_2$acac], [Ir(bim)$_2$acac], [Ir(cbim)$_2$acac] measured in nitrogen-saturated CH_2Cl_2 (25°C).

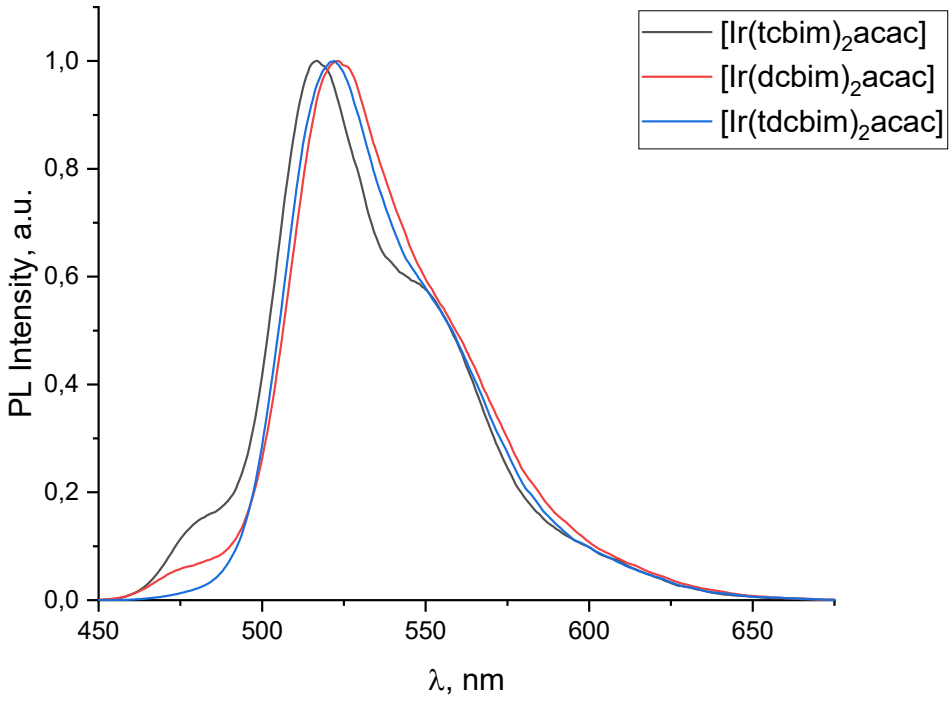

Figure S48. Normalized luminescence spectra of [Ir(tdcbim)$_2$acac], [Ir(dcbim)$_2$acac], [Ir(tcbim)$_2$acac] measured in nitrogen-saturated CH_2Cl_2 (25°C).

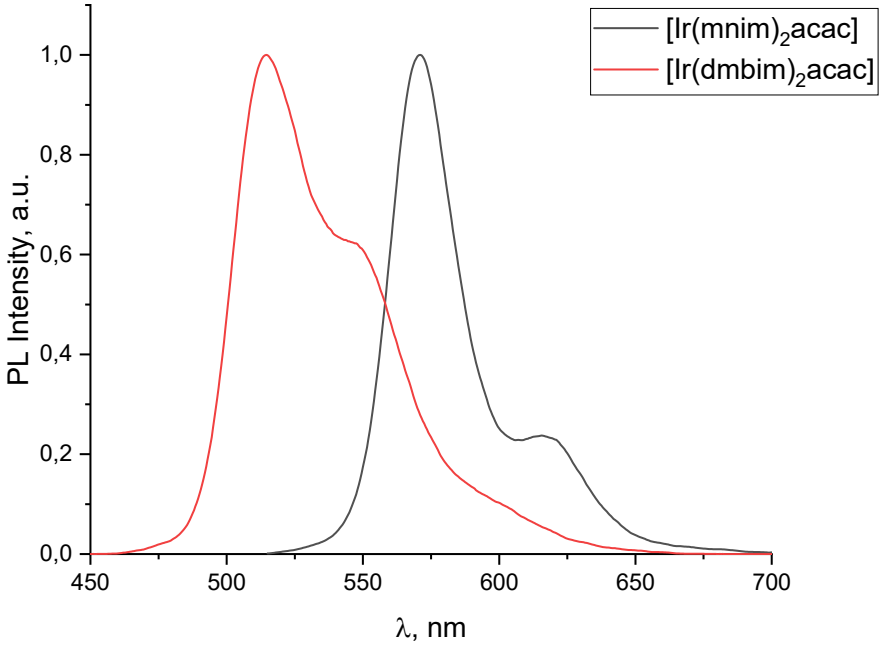

Figure S49. Normalized luminescence spectra of [Ir(dmbim)$_2$acac] and [Ir(mnim)$_2$acac] measured in nitrogen-saturated CH_2Cl_2 (25°C).

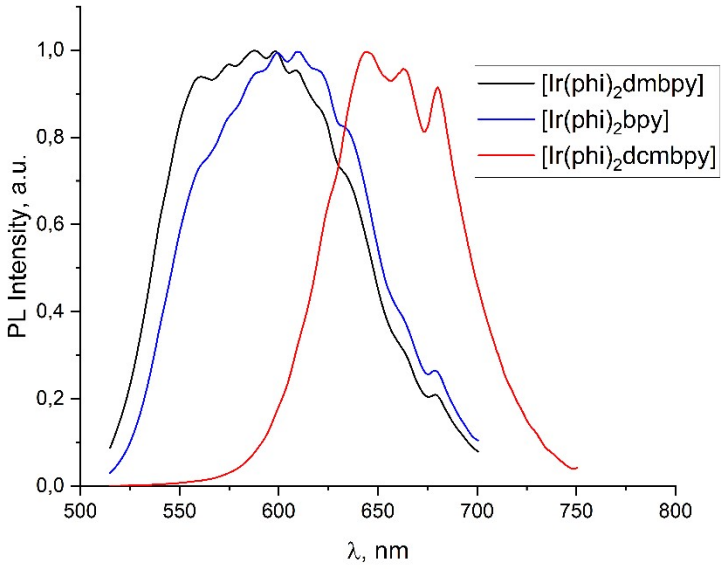

Figure S50. Normalized luminescence spectra of [Ir(phi)$_2$(dmbpy)], [Ir(phi)$_2$(bpy)], [Ir(phi)$_2$(dcmbpy)] measured in nitrogen-saturated CH_2Cl_2 (25°C).

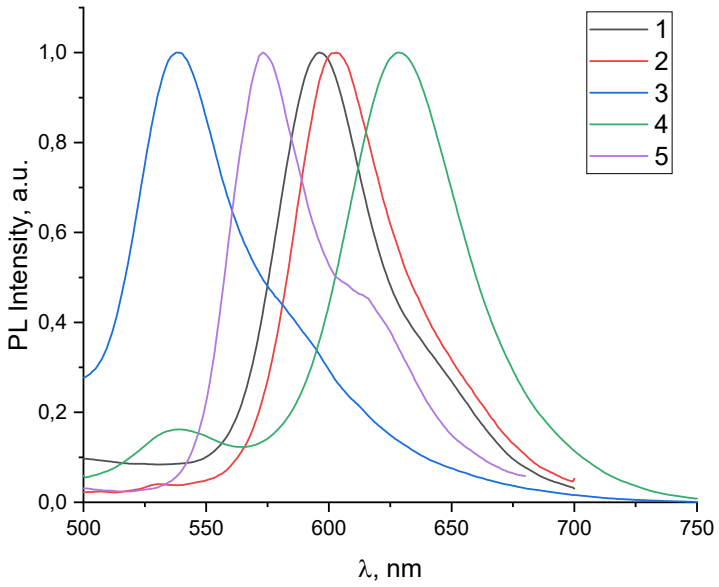

Figure S51. Normalized luminescence spectra of the complexes 1 – 5 measured in nitrogen-saturated CH_2Cl_2 (25°C); (synthesis and characterization were reported previously in [3])

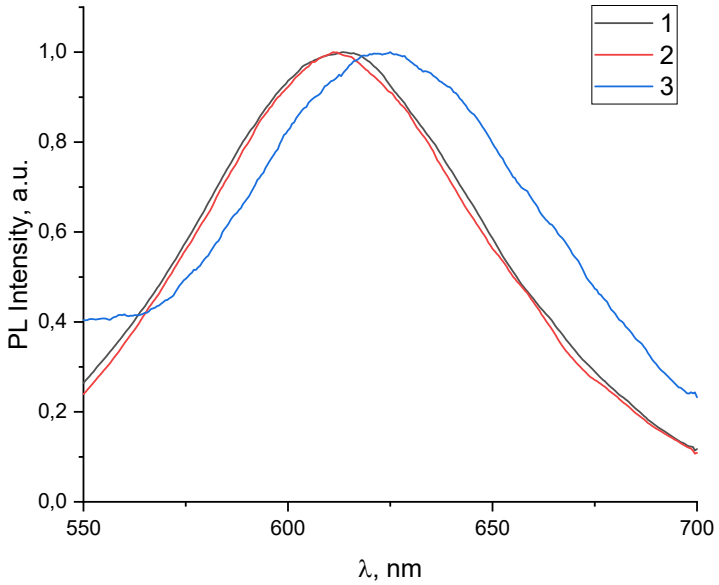

Figure S52. Normalized luminescence spectra of the complexes 1 – 3 measured in nitrogen-saturated CH_2Cl_2 (25°C); (synthesis and characterization were reported previously in [4]).

Table S4. Oxidation potentials of the newly synthesized complexes.

Complex	E_{ox}, vs. Fc^+/Fc, V	
$[Ir(mnim)_2acac]$	0.31	
$[Ir(bim)_2acac]$	0.30	
$[Ir(tcbim)_2acac]$	0.38*	0.63
$[Ir(cbim)_2acac]$	0.37*	0.50
$[Ir(tbim)_2acac]$	0.25	
$[Ir(dcbim)_2acac]$	0.46	
$[Ir(mbim)_2acac]$	0.13	0.85*
$[Ir(tdcbim)_2acac]$	0.41	
$[Ir(dmbim)_2acac]$	0.27	
$[Ir(phi)_2dmbpy]$	0.77	
$[Ir(phi)_2bpy]$	0.81	
$[Ir(phi)_2dcmbpy]$	0.92*	
*irreversible processes		

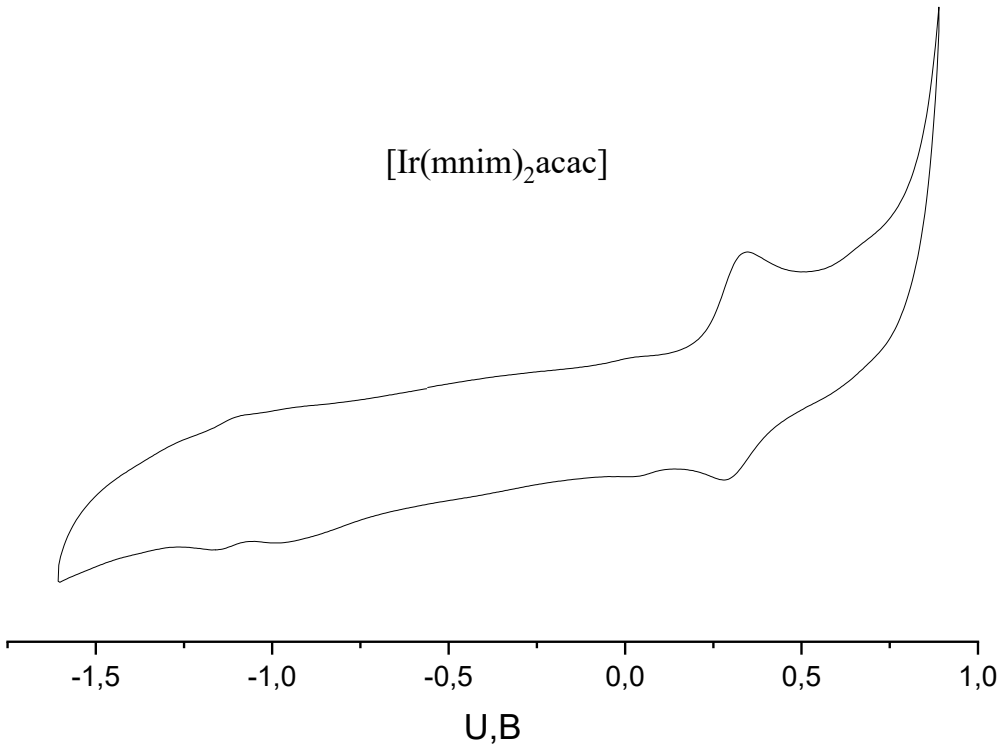

Figure S53. Cyclic voltammogram of [Ir(mnim)$_2$acac] recorded in Ar-saturated dichloromethane with 0.25 M (*n*-Bu_4N)ClO_4 at a scan rate of 200 mV/s.

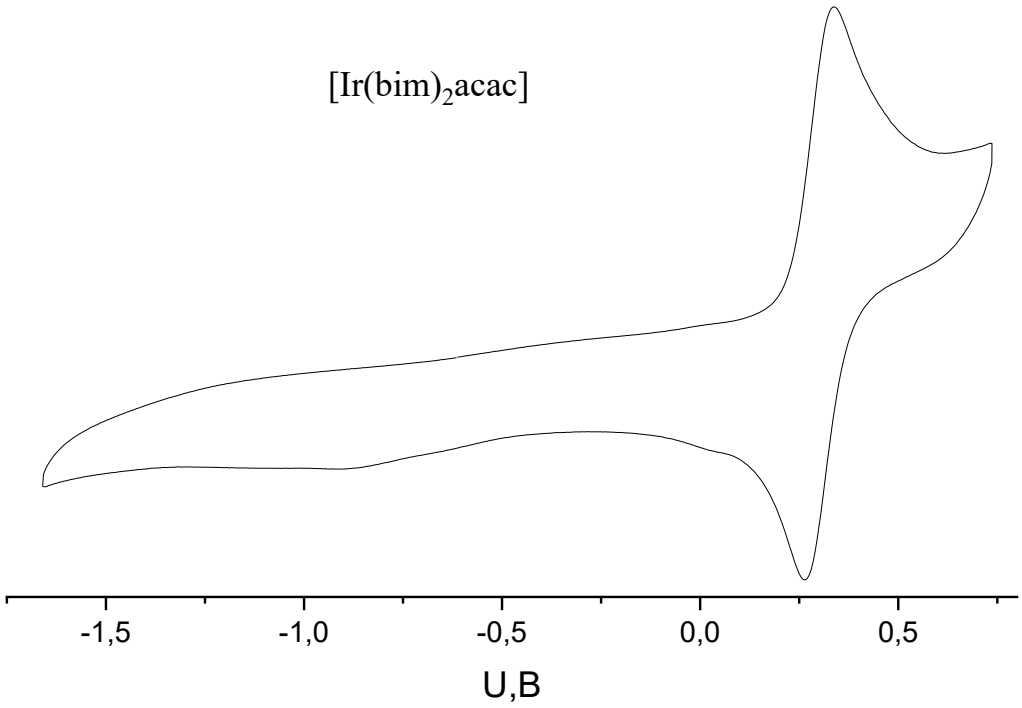

Figure S54. Cyclic voltammogram of [Ir(bim)$_2$acac] recorded in Ar-saturated dichloromethane with 0.25 M (*n*-Bu_4N)ClO_4 at a scan rate of 200 mV/s.

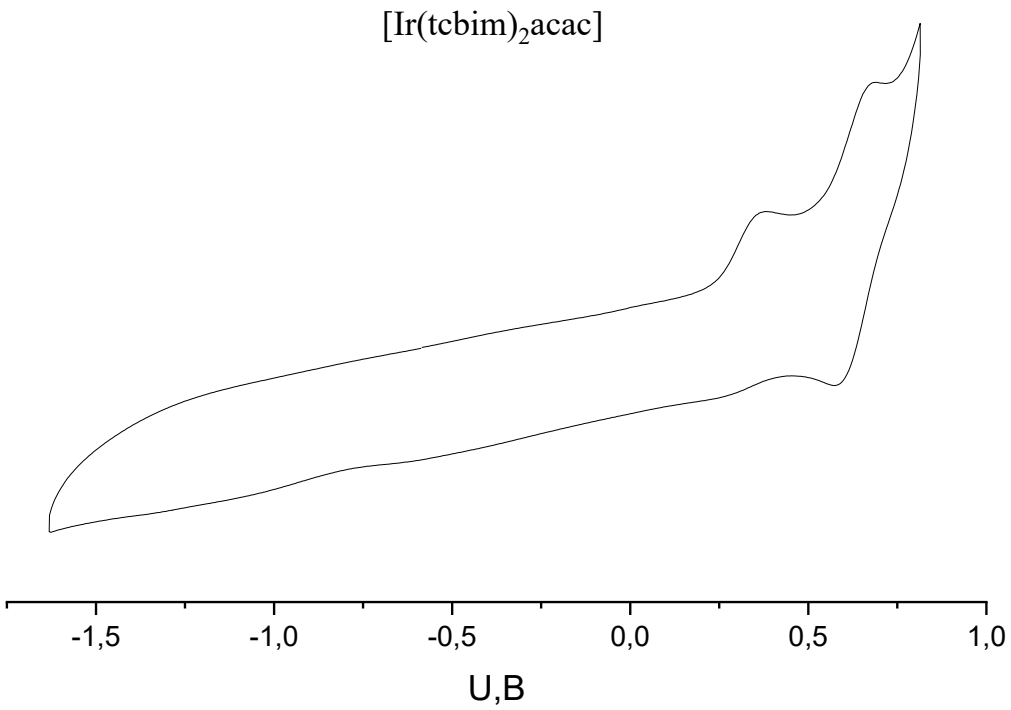

Figure S55. Cyclic voltammogram of [Ir(tcbim)$_2$acac] recorded in Ar-saturated dichloromethane with 0.25 M (n-Bu$_4$N)ClO$_4$ at a scan rate of 200 mV/s.

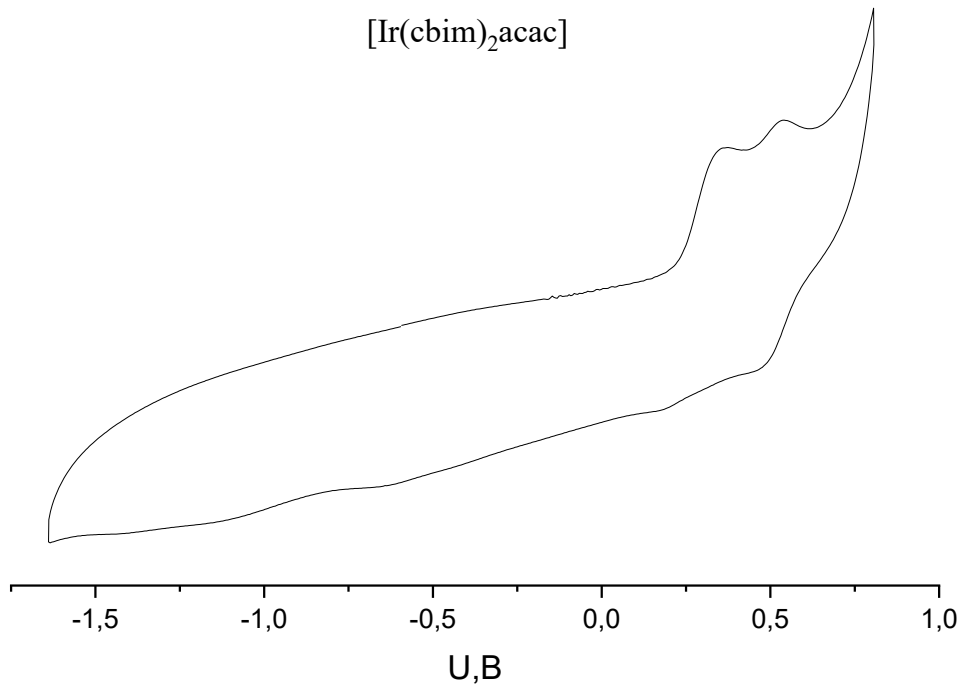

Figure S56. Cyclic voltammogram of [Ir(cbim)$_2$acac] recorded in Ar-saturated dichloromethane with 0.25 M (n-Bu$_4$N)ClO$_4$ at a scan rate of 200 mV/s.

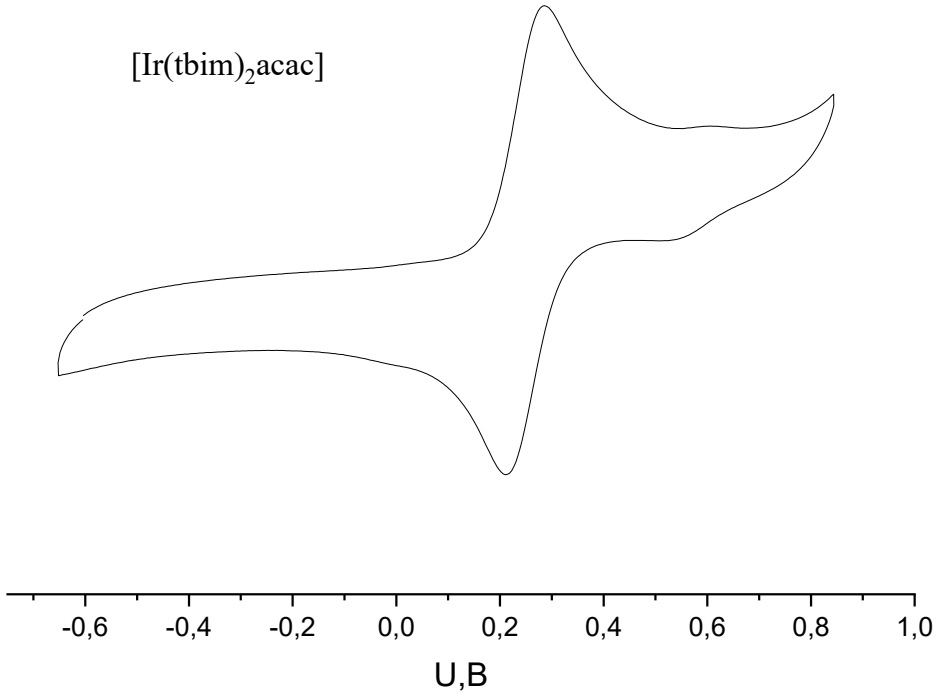

Figure S57. Cyclic voltammogram of [Ir(tbim)$_2$acac] recorded in Ar-saturated dichloromethane with 0.25 M (*n*-Bu$_4$N)ClO$_4$ at a scan rate of 200 mV/s.

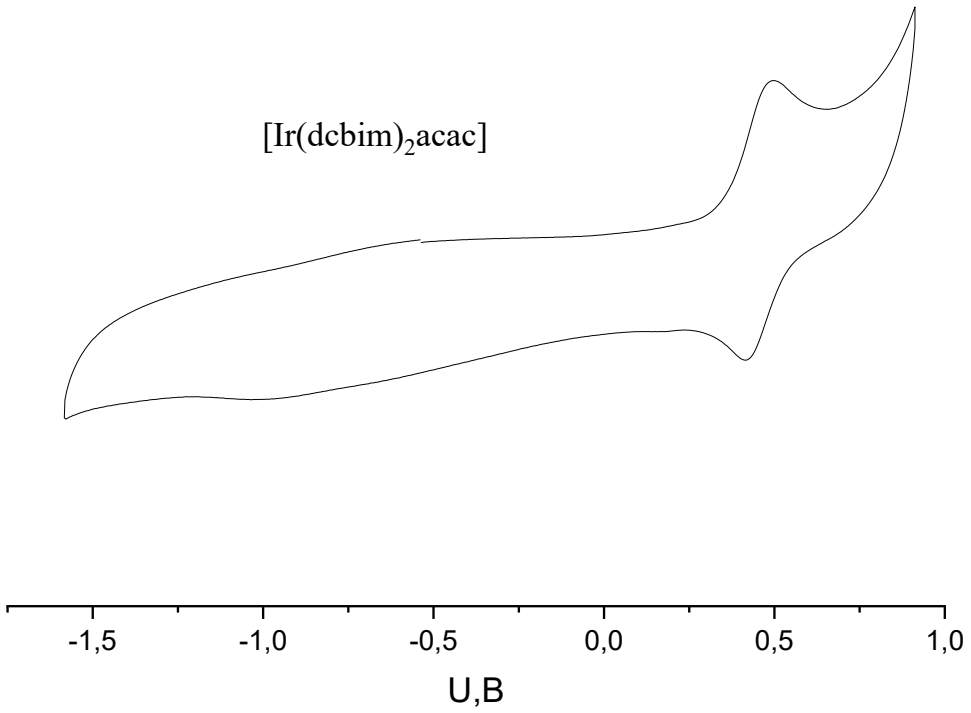

Figure S58. Cyclic voltammogram of [Ir(dcbim)$_2$acac] recorded in Ar-saturated dichloromethane with 0.25 M (*n*-Bu$_4$N)ClO$_4$ at a scan rate of 200 mV/s.

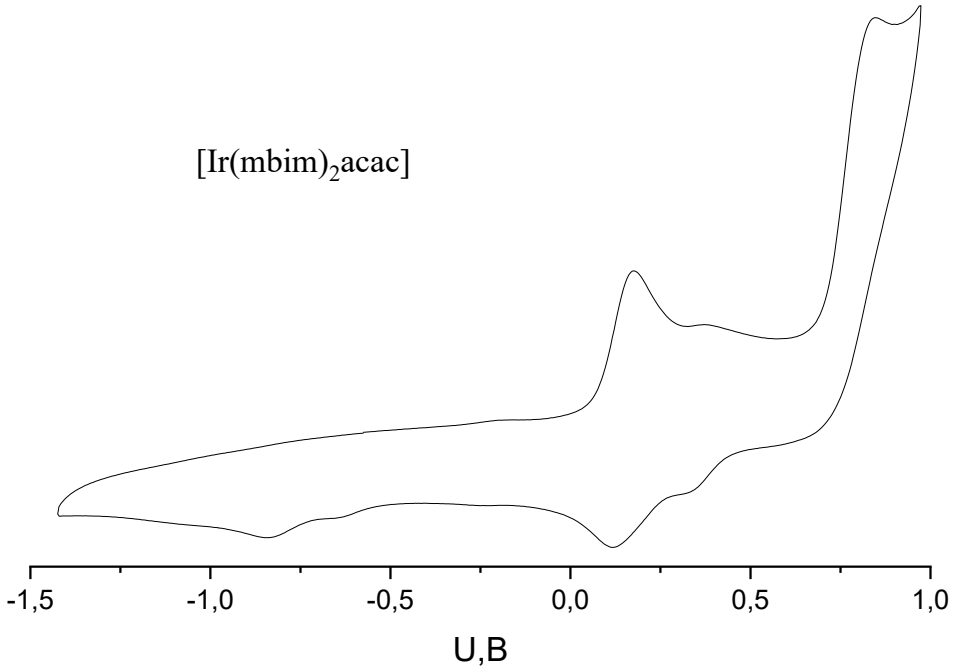

Figure S59. Cyclic voltammogram of [Ir(mbim)$_2$acac] recorded in Ar-saturated dichloromethane with 0.25 M (n-Bu$_4$N)ClO$_4$ at a scan rate of 200 mV/s.

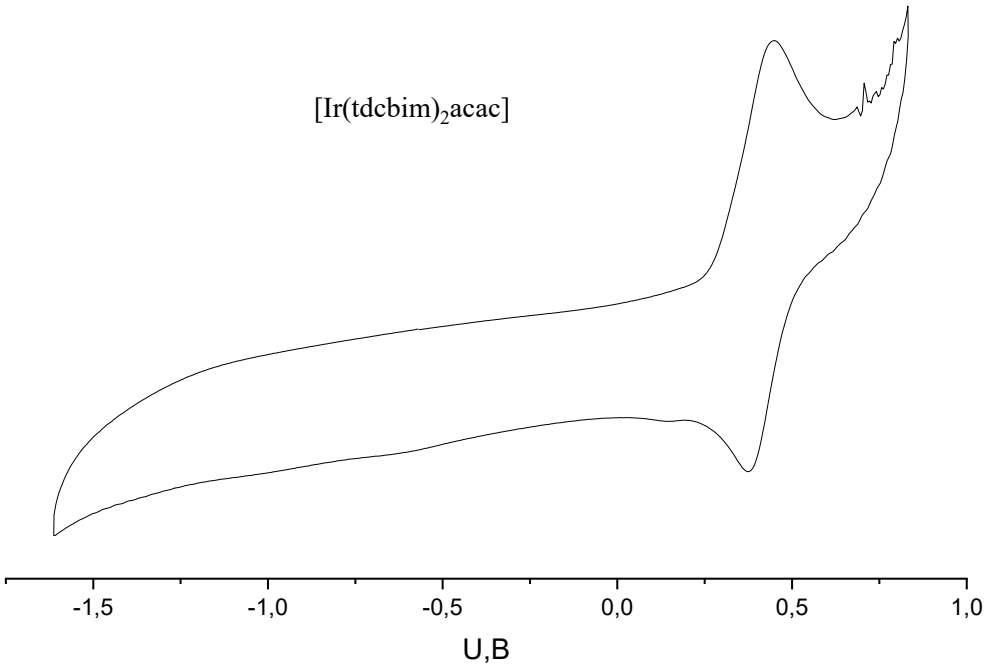

Figure S60. Cyclic voltammogram of [Ir(tdcbim)$_2$acac] recorded in Ar-saturated dichloromethane with 0.25 M (n-Bu$_4$N)ClO$_4$ at a scan rate of 200 mV/s.

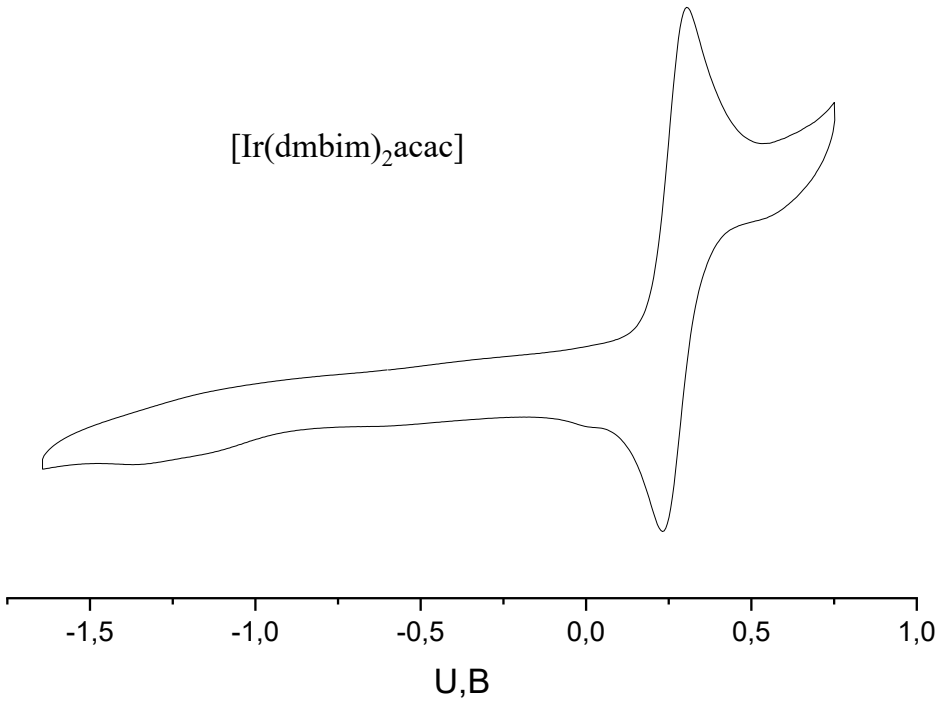

Figure S61. Cyclic voltammogram of [Ir(dmbim)$_2$acac] recorded in Ar-saturated dichloromethane with 0.25 M (*n*-Bu$_4$N)ClO$_4$ at a scan rate of 200 mV/s.

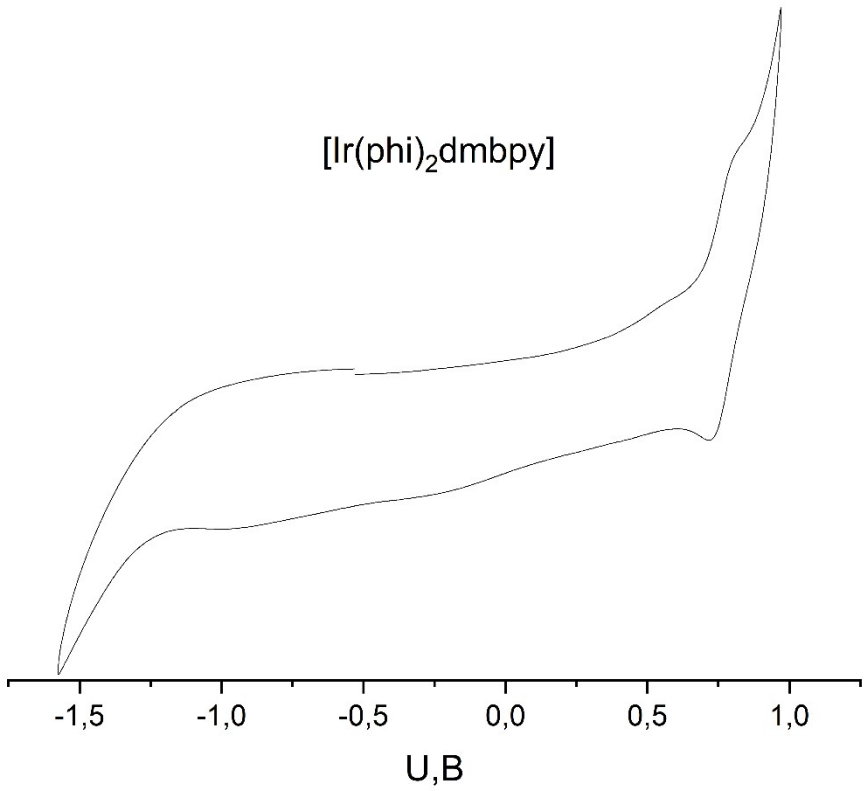

Figure S62. Cyclic voltammogram of [Ir(phi)$_2$dmbpy] recorded in Ar-saturated dichloromethane with 0.25 M (*n*-Bu$_4$N)ClO$_4$ at a scan rate of 200 mV/s.

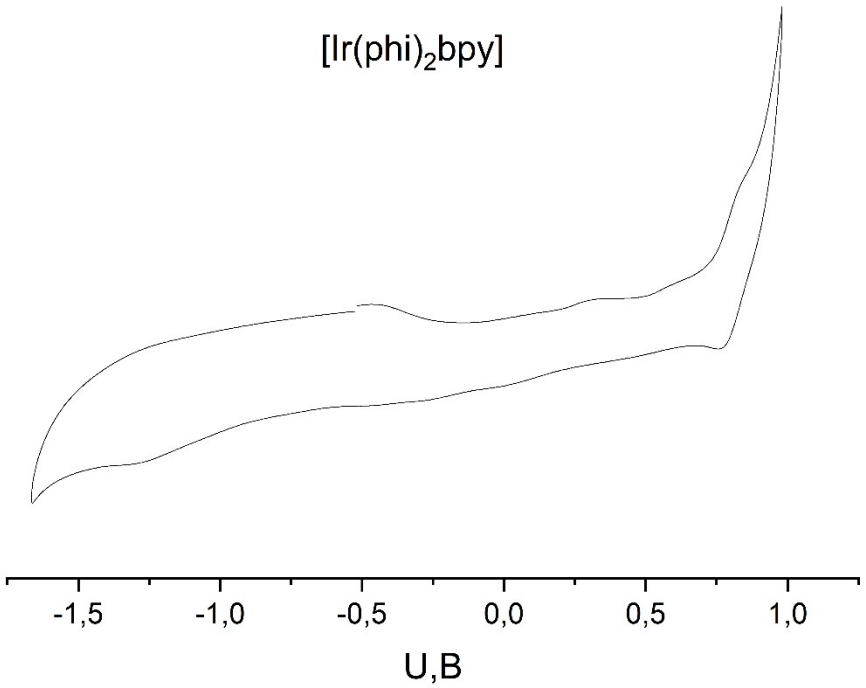

Figure S63. Cyclic voltammogram of [Ir(phi)$_2$bpy] recorded in Ar-saturated dichloromethane with 0.25 M (*n*-Bu$_4$N)ClO$_4$ at a scan rate of 200 mV/s.

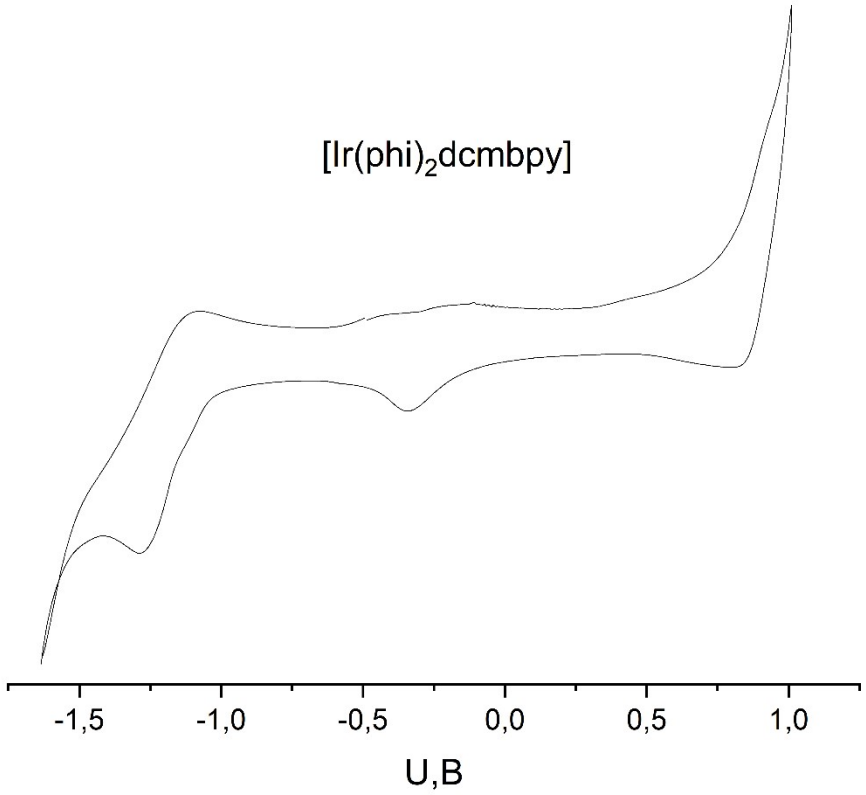

Figure S64. Cyclic voltammogram of [Ir(phi)$_2$dcmbpy] recorded in Ar-saturated dichloromethane with 0.25 M (*n*-Bu$_4$N)ClO$_4$ at a scan rate of 200 mV/s.

5. DFT calculation and machine learning (ML) details

All the calculations reported in this paper have been performed within density functional theory (DFT),[5] using the hybrid functional B3LYP.[6,7] The standard def2-SVP basis set for light elements and Stuttgart-Dresden effective core potential (ECP) for Ir atom,[8] as implemented in the ORCA 5.0 suite of programs[9], was applied. Frequency analysis was carried out to check if optimized structures were local minima. No imaginary frequencies were found for local minima. The polarizable continuum model C-PCM[10] with parameters of CH_2Cl_2 was applied to imitate the solvent medium. The theoretical emission wavelength was computed as the ΔSCF value corresponding to the difference between the triplet and singlet single point energy calculations at the optimized triplet minima.

Table S5. Hyperparameters of tested machine learning algorithms.

Model	Task	The best hyperparameters
kNN	λ_{max} prediction	{'n_neighbors': 2}
SVR	λ_{max} prediction	{'C': 980.3782570100385, 'epsilon': 0.0010807171902425606}
LightGBM	λ_{max} prediction	{'learning_rate': 0.008945691798973802, 'num_leaves': 430, 'subsample': 0.421299382581721, 'colsample_bytree': 0.7782704746853497, 'min_data_in_leaf': 1, 'objective': 'regression', 'metric': 'rmse', 'n_estimators': 1000, 'verbosity': -1, 'bagging_freq': 1}
CatBoost	λ_{max} prediction	{'learning_rate': 0.10283991617950267, 'depth': 8, 'subsample': 0.5843053868788202, 'colsample_bylevel': 0.2298254995755487, 'min_data_in_leaf': 30}
XGBoost	λ_{max} prediction	{'learning_rate': 0.06238679289783574, 'max_depth': 7, 'subsample': 0.9982371412074009, 'colsample_bytree': 0.1637075927345035, 'min_child_weight': 1, 'objective': 'reg:squarederror', 'n_estimators': 1000, 'verbosity': 0}
kNN	PLQY prediction	{'n_neighbors': 2}
SVR	PLQY prediction	{'C': 1.1803186568111252, 'epsilon': 0.004389660374508496}

LightGBM	PLQY prediction	{'learning_rate': 0.0312578769878087, 'num_leaves': 367, 'subsample': 0.5808481639196008, 'colsample_bytree': 0.28534206471458423, 'min_data_in_leaf': 1, 'objective': 'regression', 'metric': 'rmse', 'n_estimators': 100, 'verbosity': -1, 'bagging_freq': 1}
CatBoost	PLQY prediction	{'learning_rate': 0.04153336533280499, 'depth': 10, 'subsample': 0.9132677097127234, 'colsample_bylevel': 0.540038955308394, 'min_data_in_leaf': 61, 'n_estimators':1000}
XGBoost	PLQY prediction	{'learning_rate': 0.06238679289783574, 'max_depth': 7, 'subsample': 0.9982371412074009, 'colsample_bytree': 0.1637075927345035, 'min_child_weight': 1, 'objective': 'reg:squarederror', 'n_estimators': 1000, 'verbosity': 0}
kNN	PLQY classification	{'n_neighbors': 1}
SVC	PLQY classification	{'C': 4.831903143096115}
LightGBM	PLQY classification	{'learning_rate': 0.010108586093225807, 'num_leaves': 1018, 'colsample_bytree': 0.07145984259032351, 'min_data_in_leaf': 2, 'n_estimators': 100, 'verbosity': -1, 'bagging_freq': 1}
CatBoost	PLQY classification	{'n_estimators': 1000}
XGBoost	PLQY classification	{'n_estimators': 1000}

Table S6. The λ_{max} (nm) of 33 complexes in DCM predicted by DFT and different ML models.

Abbreviation	λ_{max} exp	λ_{max} DFT	λ_{max} XGBoost	λ_{max} LightGBM	λ_{max} CatBoost	Reference
[Ir(phi)$_2$(dmbpy)]	588	581	581	571	590	This work
[Ir(phi)$_2$(bpy)]	610	596	562	565	565	This work
[Ir(phi)$_2$(dcmbpy)]	644	703	651	611	657	This work
[Ir(tcbim)$_2$(acac)]	517	569	537	527	536	This work
[Ir(tbim)$_2$(acac)]	510	558	540	534	542	This work
[Ir(dmbim)$_2$(acac)]	515	572	536	520	526	This work
[Ir(mnim)$_2$(acac)]	571	632	564	585	576	This work
[Ir(bim)$_2$(acac)]	513	559	531	525	529	This work
[Ir(dcbim)$_2$(acac)]	524	563	543	528	542	This work
[Ir(mbim)$_2$(acac)]	528	588	543	533	536	This work
[Ir(tdcbim)$_2$(acac)]	522	559	544	537	549	This work
[Ir(cbim)$_2$(acac)]	509	567	532	523	529	This work
1	531	679	523	523	518	[11]
2	534	697	523	531	518	[11]
3	538	642	552	557	550	[11]
4	554	712	534	538	530	[11]
5	552	657	530	538	530	[11]
6	502	713	547	545	551	[11]
7	598	799	566	558	568	[11]
8	552	717	538	531	536	[11]
9	597	716	604	611	607	[11]
13	521	581	540	544	545	[11]
Ir2	544	553	554	555	549	[12]
Ir3	548	775	561	554	540	[12]
Ir4	548	776	517	515	516	[12]
3	624	678	588	598	616	[4]
2	611	613	583	593	597	[4]
1	614	616	579	585	597	[4]
5	573	692	580	590	586	[3]
2	603	716	608	612	611	[3]
4	629	772	658	656	645	[3]
1	596	715	607	614	598	[3]
3	539	746	550	555	541	[3]

Cited literature:

[1] D. E. Smirnov, S. V. Tatarin, M. A. Kiseleva, I. V. Taydakov, M. T. Metlin, S. I. Bezzubov, *Russ. J. Inorg. Chem.* **2023**, DOI 10.1134/S0036023623601605.

[2] S. I. Bezzubov, P. Kalle, A. A. Bilyalova, S. V. Tatarin, V. D. Dolzhenko, *Chem. Eur. J.* **2018**, *24*, 12779–12783.

[3] S. V. Tatarin, D. E. Smirnov, I. V. Taydakov, M. T. Metlin, V. Emets, S. Bezzubov, *Dalton Trans.* **2023**, *52*, 6435–6450.

[4] S. V. Tatarin, P. Kalle, I. V. Taydakov, E. A. Varaksina, V. M. Korshunov, S. I. Bezzubov, *Dalton Trans.* **2021**, *50*, 6889–6900.

[5] W. Kohn, A. D. Becke, R. G. Parr, *Journal of Physical Chemistry* **1996**, *100*, 12974–12980.

[6] A. D. Becke, *Physical Review A* **1988**, *38*, 3098–3100.

[7] C. Lee, W. Yang, R. G. Parr, *Physical Review B* **1988**, *37*, 785–789.

[8] F. Weigend, R. Ahlrichs, *Phys. Chem. Chem. Phys.* **2005**, *7*, 3297–3305.

[9] F. Neese, F. Wennmohs, U. Becker, C. Riplinger, *The Journal of Chemical Physics* **2020**, *152*, 224108.

[10] M. Cossi, N. Rega, G. Scalmani, V. Barone, *J Comput Chem* **2003**, *24*, 669–681.

[11] S. V. Tatarin, E. A. Meshcheriakova, S. A. Kozyukhin, V. V. Emets, S. I. Bezzubov, *Dalton Trans.* **2023**, *52*, 16261–16275.

[12] M. A. Kiseleva, A. V. Churakov, I. V. Taydakov, M. T. Metlin, S. A. Kozyukhin, S. I. Bezzubov, *Dalton Trans.* **2023**, *52*, 17861–17872.